Structure and Properties of Quaternary and Tetragonal Heusler Compounds for Spintronics and Spin Transfer Torque Applications

Dissertation
zur Erlangung des Grades
"Doktor der Naturwissenschaften"
am Fachbereich Chemie, Pharmazie und Geowissenschaften
der Johannes Gutenberg-Universität Mainz

vorgelegt von
Vajiheh Alijani Zamani
geboren in Tehran/Iran

Mainz, 2011

Tag der mündlichen Prüfung: 7. März 2012

Die vorliegende Arbeit wurde in der Zeit von Mai 2008 bis Dezember 2011 am Institut für Anorganische und Analytische Chemie im Fachbereich Chemie, Pharmazie und Geowissenschaften der Johannes Gutenberg-Universität, Mainz unter der Leitung von

angefertigt.

Mainz, Dezember 2011

Hiermit versichere ich, dass ich die vorliegende Dissertation selbstständig verfasst und keine anderen als die angegebenen Hilfsmittel benutzt habe. Alle der Literatur entnommenen Stellen sind als solche gekennzeichnet.

Mainz, Dezember 2011

1 Zusammenfassung

Diese Dissertation ist in zwei Teile aufgeteilt: Teil 1 befasst sich mit der Vorhersage von Halb-Metallizität in quarternären Heuslerverbindungen und deren Potential für Spintronik-Anwendungen. Teil 2 befasst sich mit den strukturellen Eigenschaften der Mn_2-basierenden Heuslerverbindungen und dem Tuning von ihrer magnetischen Eigenschaften bzgl. Koerzitivfeldstärke und Remanenz. Diese Verbindungen sind geeignet für Spin-Transfer Torque-Anwendungen.

In Teil 1 wurden die folgenden drei Probenserien quarternärer Heuslerverbindungen untersucht: XX'MnGa (X = Cu, Ni und X' = Fe, Co), CoFeMnZ (Z = Al, Ga, Si, Ge) und $Co_{2-x}Rh_xMnZ$ (Z = Ga, Sn, Sb). Abgesehen von CuCoMnGa wurden alle diese Verbindungen mittels ab-initio Bandstrukturrechnungen als halbmetallische Ferromagnete prognostiziert. In der XX'MnGa-Verbindungsklasse besitzt NiFeMnGa zwar eine zu niedrige Curie-Temperatur für technologische Anwendungen, jedoch NiCoMnGa mit seiner hohen Spinpolarisation, einem hohen magnetischen Moment und einer hohen Curie-Temperatur stellt ein neues Material für Spintronik-Anwendungen dar. Alle CoFeMnZ-Verbindungen kristallisieren in der kubischen Heuslerstruktur und ihre magnetischen Momente folgen der Slater-Pauling-Regel, was Halbmetalität und eine hohe Spinpolarisation impliziert. Die ebenfalls hohen Curie-Temperaturen ermöglichen einen Einsatz weit über Raumtemperatur hinaus. In der strukturellen Charakterisierung wurde festgestellt, dass sämtliche $Co_{2-x}Rh_xMnZ$ abgesehen von CoRhMnSn verschiedene Typen von Unordnung aufweisen; daher war die ermittelte Abweichung von der Slater-Pauling-Regel sowie von der 100%-igen Spinpolarisation dieser Verbindungen zu erwarten. Die Halbmetallizität der geordneten CoRhMnSn-Verbindung sollte nach den durchgeführten magnetischen Messungen vorhanden sein.

Im zweiten Teil wurden $Mn_{3-x}Co_xGa$ und $Mn_{2-x}Rh_{1+x}Sn$ synthetisiert und charakterisiert. Es wurde gezeigt, dass $Mn_{3-x}Co_xGa$ im Bereich $x = 0.1 - 0.4$ in einer tetragonal verzerrten inversen Heuslerstruktur kristallisiert und im Bereich $x = 0.6 - 1$ in einer kubisch inversen Heuslerstruktur. Während die tetragonalen Materialien hartmagnetisch sind und Charakeristika aufweisen, die typischerweise für Spin-Transfer Torque-Anwengungen attraktiv sind, repräsentieren die weichmagnetischen kubischen Vertreter die 100% spinpolarisierten Materialien, die der Slater-Pauling-Regel folgen. Mn_2RhSn kristallisiert in der inversen tetragonal verzerrten Heuslerstruktur, weist eine hartmagnetische Hystereseschleife auf und folgt nicht der Slater-Pauling-Regel. Bei

hohen Rh-Gehalt wird die kubische inverse Heuslerstruktur gebildet. Alle kubischen
Proben sind weichmagnetisch und folgen der Slater-Pauling-Regel.

2 Abstract

This work is divided into two parts: part 1 is focused on the prediction of half-metallicity in quaternary Heusler compounds and their potential for spintronic applications and part 2 on the structural properties of Mn_2-based Heusler alloys and tuning the magnetism of them from soft to hard-magnetic for spin-transfer torque applications.

In part 1, three different series of quaternary Heusler compounds are investigated, $XX'MnGa$ (X = Cu, Ni and X' = Fe, Co), $CoFeMnZ$ (Z = Al, Ga, Si, Ge), and $Co_{2-x}Rh_xMnZ$ (Z= Ga, Sn, Sb). All of these quaternary compounds except CuCoMnGa are predicted to be half-metallic ferromagnets by ab-initio electronic structure calculations. In the $XX'MnGa$ class of compounds, NiFeMnGa has a low Curie temperature for technological applications but NiCoMnGa with a high spin polarization, magnetic moment, and Curie temperature is an interesting new material for spintronics applications. All CoFeMnZ compounds exhibit a cubic Heusler structur and their magnetic moments are in fair agreement with the Slater-Pauling rule indicating the half-metallicity and high spin polarization required for spintronics applications. Their high Curie temperatures make them suitable for utilization at room temperature and above. The structural investigation revealed that the crystal structure of all $Co_{2-x}Rh_xMnZ$ compounds aside from CoRhMnSn exhibit different types of anti-site disorder. The magnetic moments of the disordered compounds deviate from the Slater-Pauling rule indicating that 100% spin polarization are not realized in CoRhMnGa, CoRhMnSb, and $Co_{0.5}Rh_{1.5}MnSb$. Exchange of one Co in Co_2MnSn by Rh results in the stable, well-ordered compound CoRhMnSn. This exchange of one of the magnetic Co atoms by a non-magnetic Rh atom keeps the magnetic properties and half-metallicity intact.

In part 2, two series of Mn_2-based Heusler alloys are investigated, $Mn_{3-x}Co_xGa$ and $Mn_{2-x}Rh_{1+x}Sn$. It has been shown that the series $Mn_{3-x}Co_xGa$ crystallizes in the inverse tetragonal structure, for $x = 0.1 - 0.4$ and in the cubic inverse Heusler structure, for $x = 0.6 - 1$. In this series, while the tetragonal alloys, hard magnets, exhibit the features typically attractive for STT applications, the cubic systems, soft magnets, present 100% spin polarized materials obeying the Slater-Pauling rule. In $Mn_{2-x}Rh_{1+x}Sn$ series, Mn_2RhSn crystallizes in the inverse tetragonal structure, shows a hard-magnetic hysteresis loop and does not follow the Slater-Pauling rule. With substituting Mn by Rh, the inverse cubic structure is observed. All cubic samples show perfect Slater-Pauling behavior and a soft hysteresis loop.

Contents

3 Introduction

3.1 Half-metallic Ferromagnets

Half-metallic ferromagnets represent a new class of materials which absorbed a lot of attention considering their possible applications in spintronics (also known as magnetoelectronics) [1]. In these materials the spin resolved bands have a special behavior. One of the spin densities (in most cases majority) shows typically a metallic behavior while the other (in most cases minority) is semiconducting. Therefore, the halfmetallic ferromagnets exhibit 100% spin polarization at the Fermi energy which is supposed to maximize the efficiency of magnetoelectronic devices [2, 3]. A schematic representation of the density of states of a half-metal, a normal metal, and a semiconductor is shown in Figure 3.1 for comparison [4].

Until now a lot of half-metallic ferromagnets are known. Full-Heusler and half-Heusler alloys are the most prominent among the half-metallic compounds. Other known half-metallic materials except the half- and full-Heusler alloys [4, 5, 6, 7, 8] are some oxides (*e.g* CrO_2 and Fe_3O_4) [9], the manganites (*e.g* $La_{0.7}Sr_{0.3}MnO_3$) [9], the double perovskites (*e.g* Sr_2FeReO_6) [10], the pyrites (*e.g* CoS_2) [11], the transition metal chalcogenides (*e.g* $CrSe_2$) and pnictides (*e.g* CrAs) in the zinc-blende or wurtzite structures [12, 13, 14, 15], the europium chalcogenides (*e.g* EuS) [16] and the diluted magnetic semiconductors (*e.g* Mn impurities in Si or GaAs) [17, 18].
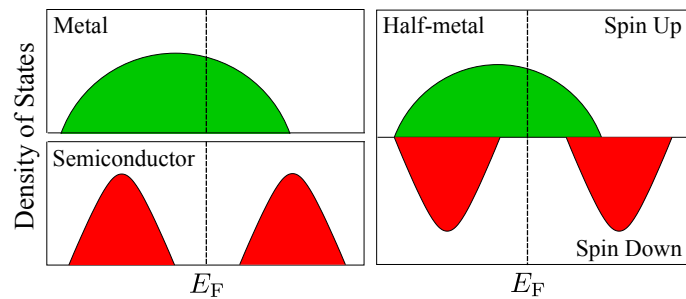

Figure 3.1: Schematic representation of the density of states for a half-metal compared to a normal metal and a semiconductor.

3.2 Heusler Compounds as Half-metallic Ferromagnets

Among the half-metallic ferromagnets which are mentioned in part 1.1 , although thin films of CrO_2 and $La_{0.7}Sr_{0.3}MnO_3$ have been verified to present practically 100% spin-polarization at the Fermi energy at low temperatures [10, 19], the Heusler alloys remain attractive for technical application like spin-injection devices [20], spin-filters [21], tunnel junctions [22], or GMR devices [23, 24] due to their relatively high Curie temperature compared to other compounds [25].

Heusler compounds first attracted interest among the scientific community in 1903, when F. Heusler found that the compound Cu_2MnAl becomes ferromagnetic, although non of its constituent elements is ferromagnetic by itself [26, 27]. The origin of interest in magnetic properties of the Heusler compounds is the prediction of half-metallic ferromagnetism in MnNiSb by de Groot *et al* [28] and in Co_2MnSn by Kübler *et al* [29]. In many Heusler compounds the total magnetic moment follows a simple electron-counting rule based on the Slater-Pauling behavior [30, 31].

3.3 The Slater-Pauling Rule

Slater [32] and Pauling [33] independently discovered that the magnetic moment (m) of the $3d$ elements and their binary alloys can be estimated on the basis of the average number of valence electrons (n_V) per atom. Depending on $m(n_V)$, the materials are divided into two classes. The first part of the Slater-Pauling curve, is the area of itinerant magnetism and high valence electron concentrations $(n_V \geq 8)$. Systems with closed packed structures (*fcc* and *hcp*) are found in this area. The second part is the area of localized magnetism and low valence electron concentrations $(n_V \leq 8)$. Here, mostly *bcc* and *bcc*-related structures are found. Iron is located at the borderline between localized and itinerant magnetism. Figure 3.2 shows the Slater-Pauling curve for $3d$ transition metals and some of their alloys.

The magnetic moment in multiples of Bohr magnetons (μ_B) for the first part of the curve describing itinerant magnetism is given by

$$m = (2n \uparrow - n_V = 2(n_d \uparrow + n_{sp} \uparrow) - n_V)\, \mu_B \tag{3.1}$$

where m denotes the magnetic moment in multiples of Bohr magnetons μ_B, $n \uparrow$ the total number of electrons in the majority states, $n_d \uparrow$ the number of spin-up electrons in d orbitals, $n_{sp} \uparrow$ the number of spin-up electrons in sp orbitals, and n_V the number of the valence electrons $(n_V = n \uparrow + n \downarrow)$.

For filled majority d bands (as e.g. in Nickel), one has $n_d \uparrow = 5$ and thus

$$m = (10 - n_V + 2n_{sp} \uparrow)\, \mu_B \tag{3.2}$$
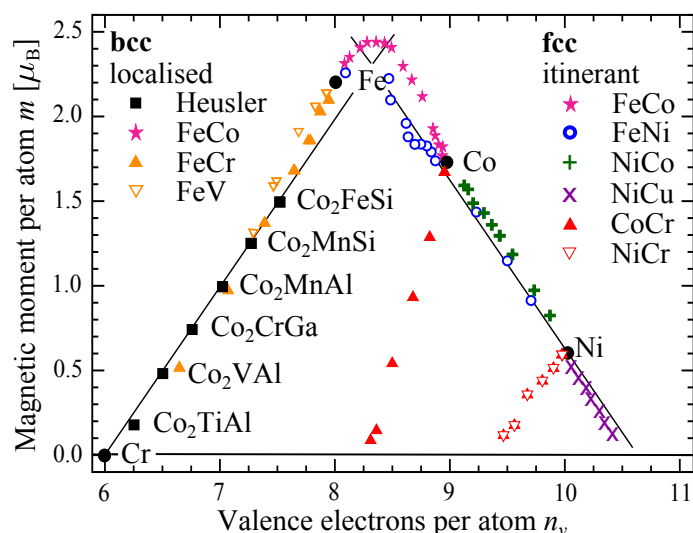
Figure 3.2: Slater-Pauling curve for $3d$ transition metals and their alloys.

Slater and Pauling found that the number of occupied sp states is approximately $n_{sp} = 2n_{sp} \uparrow \approx 0.6$, since the electrons are not polarised. This explains the magnetic moment of Ni which approximately is equal to 0.6 μ_B. It appears from the Slater-Pauling curve that some of the alloys do not follow the expected curve (Co-Cr and Ni-Cr in Figure 3.2). It was shown by Malozemov et $al.$ that the high valence concentration part of the curve can be generalized in such a way that the alloys under question still follow a similar rule [34], which also holds for alloys between transition metals and metalloids (Al, Si, Ga, etc.). For all of these cases, the magnetic moment is proportional to the average magnetic valence z_M and given by m = $z_M + 2n_{sp}\uparrow$ (for details, see Reference [31]).

The magnetic moments of Heusler compounds, especially Co_2-based half-metallic ferromagnets, follow the Slater-Pauling rule and are situated in the localized part of this curve. For localized moment systems, an average magnetic moment per atom in multiples of Bohr magnetons (μ_B) is given by

$$m = (n_V - 2n \downarrow -2n_{sp}) \, \mu_B \tag{3.3}$$

where $n\downarrow$ denotes the number of electrons in the minority states. Due to the fact that the d electrons are constrained such that the Fermi energy falls into a minimum (or gap) between occupied and unoccupied d states and therefore minimizes the total energy. The minimum in the minority density of states forces the number of electrons in the d minority band to be approximately three. In half-metallic ferromagnets with a gap in one of the spin densities or in quasi-closed-shell compounds all sp electrons are occupied, and the n_{sp} term vanishes. Therefore, the magnetic moment in the localized part of the Slater-Pauling curve can be calculated according to

$$m = (n_V - 6) \; \mu_B \tag{3.4}$$

which means that the average magnetic moment per atom is simply given by subtracting 6 from the average number of valence electrons. It is often more convenient to use the valence electron number per formula unit N_V.

For 1:1:1 Heusler compounds with 3 atoms in the unit cell, the Slater-Pauling rule is given by

$$m = (N_V - 18) \; \mu_B \tag{3.5}$$

In 2:1:1 or 1:1:1:1 Heusler compounds there are 4 atoms in the primitive cell and the total magnetic moment thus amounts to:

$$m = (N_V - 24) \; \mu_B \tag{3.6}$$

N_v is the accumulated number of valence electrons in the primitive cell (for details see References [6, 30, 31, 35]). The valence electron count means $2+n(d)$ for each transition metal and $2+n(p)$ for the main group elements, where 2 arises in both cases from the s electrons and $n(d)$ and $n(p)$ are the numbers of d and p valence electrons, respectively. At $N_v = 24$ the materials are not ferromagnetic according to the Slater-Pauling rule. The reason is that a quasi-closed-shell character is reached at a filling of the bands by 24 valence electrons. It is caused by successive filling of the a_1 (2 s electrons), t_2 (6 p electrons), e, and t_2 (10 d electrons) bands, followed by subsequent complete filling of an additional t_2 band (6 d electrons). Deviations from Equation (3.6) will appear when the compound is not in a half-metallic state, and unbalanced sp or d electrons are present. In certain cases of $L2_1$ ordered Heusler compounds, 24 valence electrons lead to the phenomenon of half-metallic completely compensated ferrimagnetism [36], where the moments are ordered in a way that the total magnetic moment vanishes even though individual magnetic moments are of different magnitudes, in contrast to antiferromagnets [37].

3.4 Crystal Structure of Heusler Compounds

3.4.1 Full-Heusler Compounds

The X_2YZ (X, Y = transition metals, Z = main group element) Heusler compounds are ternary intermetallics with a 2:1:1 stoichiometry [27, 38]. These compounds crystallize in the cubic structure ($Fm\overline{3}m$, space group no. 225) with Cu_2MnAl ($L2_1$) as prototype [26, 27, 38, 39, 40]. The X_2 atoms form a primitive cubic sublattice and adjacent cubes of this X_2 sublattice are filled alternating by Y or Z atoms (see Figure 3.3

(a)). The primitive cell of the $L2_1$ structure contains four atoms that form the base of the fcc primitive cell. The result is a lattice with the $Fm\bar{3}m$ symmetry were the Wyckoff positions 4a (0, 0, 0), 4b (1/2, 1/2, 1/2), and 8c (1/4, 1/4, 1/4) are occupied by Z, Y, and X_2, respectively.
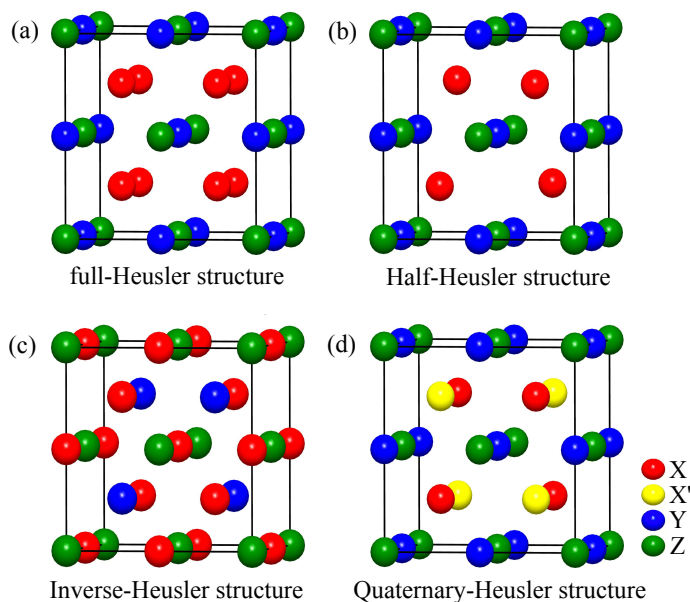
Figure 3.3: Different types of Heusler structures. Full-Heusler (a), Half-Heusler (b), Inverse-Heusler (c), and Quaternary-Heusler structures (d).

3.4.2 Half-Heusler Compounds

The Half-Heusler compounds (general formula: XYZ, X and Y = transition metals, Z = main group element) crystallize in a non-centrosymmetric cubic structure (space group no. 216, $F\bar{4}3m$, C1$_b$) which is a ternary ordered variant of the CaF$_2$ structure and can be derived from the tetrahedral ZnS-type structure by filling the octahedral lattice sites (Figure 3.3 (b)). C1$_b$ compounds of composition XYZ consist of three interpenetrating fcc sublattices, each of which are occupied by the X, Y and Z atoms [25]. The corresponding occupied Wyckoff positions are 4a (0, 0, 0), 4b (1/2, 1/2, 1/2), and 4c (1/4, 1/4, 1/4). Table 3.1 summarizes three inequivalent atomic arrangements which are possible for this structure type.

3.4.3 Inverse Heusler Compounds

In X_2YZ compounds, if the atomic number of Y, $Z(Y)$, is higher than the one of X, $Z(X)$, from the same period ($Z(Y) > Z(X)$), an inverse Heusler structure ($F\bar{4}3m$, space group no. 216) is observed. It may also appear in compounds with transition metals from different periods [41]. Usually, the element X is more electropositive than Y. In

Table 3.1: Inequivalent site occupancies within the C1$_b$-type structure. Atoms on Wyckoff positions 4a and 4c form a ZnS-type sublattice, the atoms on 4b occupy the octahedral holes.

	4a	4b	4c
	(0,0,0)	(1/2,1/2,1/2)	(1/4,1/4,1/4)
Type I	X	Y	Z
Type II	Z	X	Y
Type III	Y	Z	X

contrast to the normal Heusler structure where all of the X atoms fill the tetrahedral holes (see Figure 3.4), in the inverse Heusler structure, X and Z atoms form a rock salt lattice to achieve an octahedral coordination for X atoms and the remaining X atoms and Y atoms fill the tetrahedral holes with fourfold symmetry. Both octahedral and tetrahedral holes for inverse Heusler structure are displayed in Figure 3.4. This structure is still described by four interpenetrating fcc sublattices, however the X atoms do not form a simple cubic lattice. Instead, they are placed on the Wyckoff positions 4b(1/2, 1/2, 1/2) and 4d (3/4, 3/4, 3/4), while the Y and Z atoms are located at 4c (1/4, 1/4, 1/4) and 4a (0, 0, 0) respectively (see Figure 3.3 (c)). AgLi$_2$Sb is the prototype of this structure [42] (the older printed version of Pearson's Handbook used CuHg$_2$Ti [41] but the electronic version uses correctly AgLi$_2$Sb as prototype [42, 43]). It is also possible to emphasize the difference to normal Heusler compounds by expressing the formula as *(XY)XZ*. The inverse Heusler structure is frequently observed for Mn$_2$-based materials with Z(Y) > Z(Mn) (see Figure 3.4). Mn$_2$CoSn or (MnCo)MnSn is the most prominent example for this structure [44, 45].

3.4.4 Quaternary Heusler Compounds

When one of the two X atoms in X_2YZ compounds (full-Heusler compounds) is substituted by a different transition metal X', a quaternary compound with the composition $XX'YZ$ and $F\bar{4}3m$ symmetry (space group no. 216) is generated. The prototype of this Y-type structure of quaternary Heusler compounds is LiMgPdSn [46, 47]. Three possible nonequivalent superstructures based on the different positions of the four atoms exist for this structure type [48]. Different site occupations for this structure are shown in Table 3.2 for the CoFeMnM (M is a main group element) compound as an example. As shown in Figure 3.3 (d) the LiMgPdSn-type structure exhibits a primitive fcc cell with a basis containing four atoms on the Wyckoff positions $4a$ to $4d$, which form a larger cubic cell. The exchange of the atoms between $4a$ and $4b$ or $4c$ and $4d$ positions and between the groups $(4a, 4b) \leftrightarrow (4c, 4d)$ does not change the structure due to the
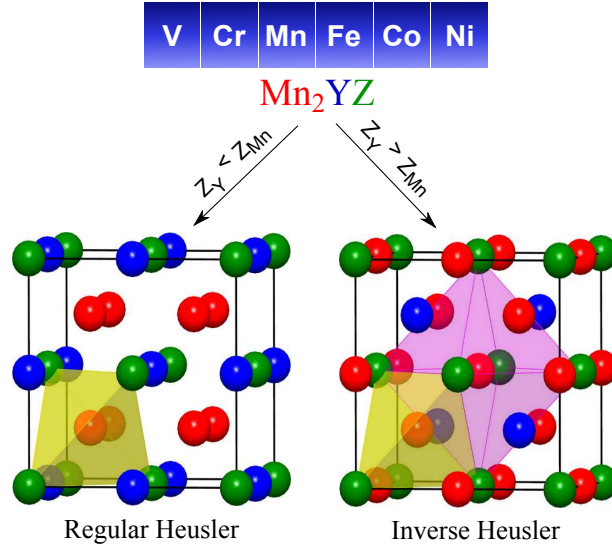
Figure 3.4: Inverse and regular structure for Mn_2-based Heusler compounds. Both, the inverse and the regular structure can be formed for Mn_2-based Heusler compounds depending on the atomic number of the element on the Y position.

symmetry implied by the $F\bar{4}3m$ space group.

Several quaternary—or, better, pseudo-ternary—Heusler compounds ($T_2T'_{1-x}T''_xM$) have been designed in order to tailor the middle of the minority band gap exactly to the Fermi energy. Quaternary Heusler compounds with a 1:1:1:1 stoichiometry ($TT'T''M$), however, have as yet been little explored. For symmetry reasons (T_d), they are substantially different from the $L2_1$ pseudo-ternary Heusler compounds with O_h symmetry and $2 : [(1-x) : x] : 1$ or $2 : 1 : [(1-y) : y]$ stoichiometry. In applications, the quaternary $TT'T''M$ compounds will have advantages over the pseudo-ternary $T_2T'_{1-x}T''_xM$ alloys. In the latter case, $i.e.$, the alloy type, random distribution of T' and T'' leads to additional disorder scattering resistivity and thus to an increase in the total resistivity. The result is that electronic devices based on *"real"* quaternary Heusler compounds are expected to have lower power dissipations.

3.4.5 Tetragonally Distorted Heusler Compounds

Until now only few tetragonal distorted Heusler materials have been studied thoroughly, Rh_2YSn (Y = V, Cr, Fe, or Co) [49] and $Mn_{3-x}Ga$ [50, 51] are the most prominent examples. A tetragonal distortion is observed for Mn_2YZ compounds crystallizing in the inverse Heusler structure. In this structure, the Mn atoms occupy two different lattice sites, one with tetragonal and one with octahedral coordination (see Figure 3.4). Kübler showed that the Mn atom on the octahedral site possesses an oxidation state of +3 (Mn^{3+}, d^4) [29]. According to the crystal field theory, the triple degenerated t_{2g} orbitals and one of the double degenerated e_g orbitals are occupied by a single electron

Table 3.2: Different site occupations for the Y-type structure. M assigns the main
group element. Note that the exchange of the atoms between $4a$ and $4b$
or $4c$ and $4d$ positions and between the groups $(4a, 4b) \leftrightarrow (4c, 4d)$ does not
change the structure due to the symmetry implied by the $F\overline{4}3m$ space group.
In $L2_1$ the positions $(4c, 4d)$ become equivalent and combine to $8c$.

	$4a$ $(0,0,0)$	$4c$ $(1/4,1/4,1/4)$	$4b$ $(1/2,1/2,1/2)$	$4d$ $(3/4,3/4,3/4)$
Y Type I	M	Fe	Mn	Co
Y Type II	M	Mn	Fe	Co
Y Type III	Fe	M	Mn	Co

for a single d^4 high-spin ion in an octahedral environment. This electron configuration
energetically is not favored and energy can be gained by a distortion of the octahe-
dron. Both, an elongation and a compression are possible. These distortions cause a
decreasing in energy levels of the occupied orbitals. This phenomenon is often referred
to as Jahn-Teller-distortion. The c/a ratios for Heusler alloys usually indicate distor-
tion which is comparable or larger than that observed in tetragonal spinels containing
the Jahn-Teller ions Mn^{3+} and Cu^{2+} [49, 52]. The appearance of this tetragonal dis-
tortion is attributed to an electronic instability of the band Jahn-Teller effect. In the
band type of Jahn-Teller effect, bands which are degenerate in the cubic system are
no longer degenerate in the tetragonal system, allowing a repopulation of electrons to-
ward the lower energy bands. In contrast to the usual Jahn-Teller effect which shows
a splitting of energy levels, in the band Jahn-Teller effect the main effect is a modi-
fication of the width of the energy levels- a narrowing of bands derived from orbitals
which overlap in the direction of crystal elongation, and a broadening of bands which
overlap in the direction of contraction. For example the $3d$-e_g narrow band orbitals are
degenerate in the cubic structure, but in the tetragonal structure, for $c/a>1$, the d_{z^2}
band will narrow and the $d_{x^2-y^2}$ band will widen because of decreased orbital overlap
respectively [49, 53, 54]. This allows a net transfer of 3d electrons to the $d_{x^2-y^2}$ band.

The cubic unit cell undergoes an elongation along the c axis, in the case of Mn_2YZ
compounds [40]. Therefore similar to the cubic Heusler structure, two different types
of structures are known for the tetragonal cell (see Figure 3.5). As shown in Fig-
ure 3.5, a regular tetragonal cell (Figure 3.5(a)) derived from the Cu_2MnAl-type struc-
ture (full Heusler structure) and an inverse tetragonal cell (Figure 3.5(b)) derived from
the $CuHg_2Ti$-type structure (inverse Heusler structure). The symmetry of the regular
tetragonal structure is I4/mmm (space group no. 139). In this structure, the X atoms
occupy the Wyckoff position 4d (0, 1/2, 1/4), the Y and the Z atoms are located at
2b (0, 0, 1/2) and 2a (0, 0, 0), respectively. If $X=Y$, like wise Mn_3Ga, the symmetry

becomes DO_{22} (prototype Al_3Ti) [51]. In the inverse tetragonal structure ($I\bar{4}m2$, space group no. 119) two Mn atoms occupy two different lattice sites, one with tetragonal and one with octahedral coordination. The first Mn atom is located at the Wyckoff position 2b (0, 0, 1/2), while the second Mn atom and the Y atom are placed at the Wyckoff position 4d (0, 1/2, 1/4). Finally, the Z atom occupies the 2a (0, 0, 0) position.
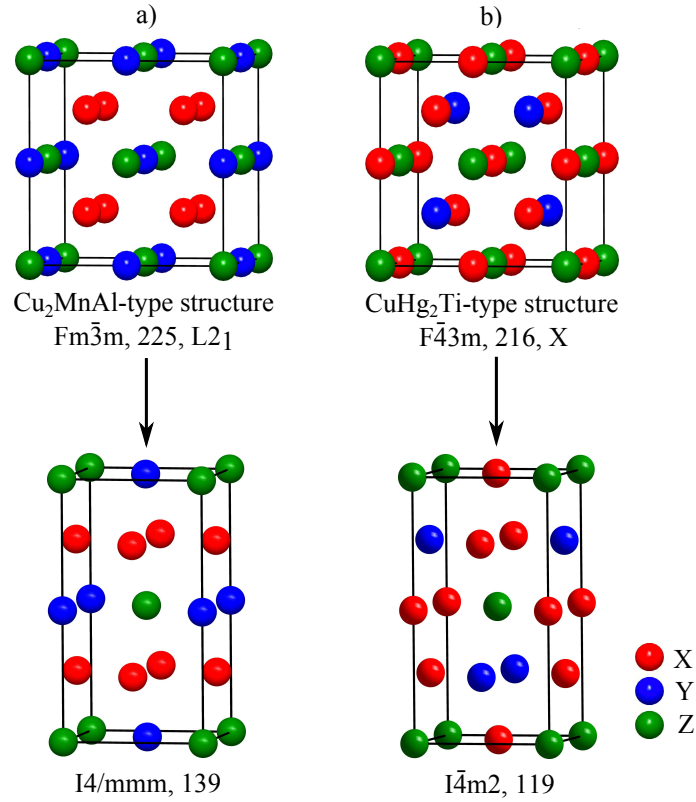
Figure 3.5: Regular (a) and inverse (b) Heusler structures and their related tetragonally distorted unit cells.

Experimentally, the tetragonal distortion becomes evident by a splitting of the cubic (220) reflex into the (112) and (200) reflexes in the corresponding XRD pattern. Depending on the direction of the distortion (elongation or compression), the reflexes move to smaller or larger scattering angles compared to the cubic (220) reflex. Therefore, the distance between the (112) and the (200) reflexes is a measure for the degree of distortion. From the series of the (112) and (200) reflexes one can decide whether $c/a>1$ or $c/a<1$. When the (200) reflex appears after the (112) reflex, it means $c/a>1$ and an elongation occured in the cell and when the (200) reflex appears before the (112) reflex, compression happened in the cell and $c/a<1$.

Mn_2YZ compounds are intresting materials as both tetragonal and cubic phases are found among them. Mn_2YZ tetragonal systems are particularly interesting due to their perpendicular magnetic anisotropy which can be achieved in thin films [55] opening the

door to spin-torque devices. Therefore, it is essential to design new materials that fulfill the corresponding criteria, i.e. high spin polarization and Curie temperature but a low saturation magnetization and magnetic damping. Mn_2YZ cubic systems also attract lot of attention due to their half-metallic properties. It seems that Mn_2YZ cubic alloys are the second largest family of Heusler alloys after the Co_2YZ compounds which present the 100% spin polarized materials (or half-metals) obeying the Slater-Pauling rule.

3.5 Order-Disorder Phenomena in Full-Heusler Compounds

The properties of Heusler materials are strongly dependent on the atomic arrangement of the atoms. Band structure calculations show that already small amounts of disorder within the distribution of the atoms on the lattice sites cause distinct changes in their electronic structure, and thus also in their magnetic and transport properties [56, 57, 58] and also it leads to a decrease in spin polarization [59]. Therefore, a careful analysis of crystal structure is essential to understand the structure-to-property relation of Heusler compounds.

   The most prominent disordered Heusler structures [25, 48, 60, 61, 62] are displayed in Figure 3.6. The most frequent type of disorder for $L2_1$ structure is the CsCl-like structure, also known as $B2$-type disorder. In this disorder structure, the Y and Z atoms are equally distributed and consequently the 4a and 4b positions become equivalent. As a consequence, the symmetry is reduced and the resulting space group is $Pm\bar{3}m$. On the other hand, the random distribution of X and Y or X and Z leads to a BiF_3-type disorder (space group no. 216: $Fm\bar{3}m$, DO_3). The NaTl-type structure occurs very rarely. In this structure type, the X-atoms, which occupy one of the *fcc* sub-lattices, are mixed with the Y atoms, whereas the X atoms on the second sub-lattice are mixed with the Z atoms. This kind of disorder is also known as B32a disorder (space group no. 227, $Fd\bar{3}m$). Here, the X atoms are placed at the Wyckoff position 8a (0, 0, 0), while Y and Z are randomly distributed at position 8b (1/2, 1/2, 1/2). In contrast to these partial disorder phenomena all positions become equivalent in the tungsten-type structure leading to a *bcc* lattice and reduced symmetry ($Im\bar{3}m$ (A2)). It should be noted that some types of disorder can not be easily detected by XRD, as the scattering coefficients of the *3d*-transition metals are very similar.

3.6 Application of Heusler Compounds as Half-metallic Ferromagnets in Spintronics

Magnetoelectronics, also known as spintronics, is probably the field with the most rapid growth in materials science [1, 63] and is one of the emerging disciplines that continue
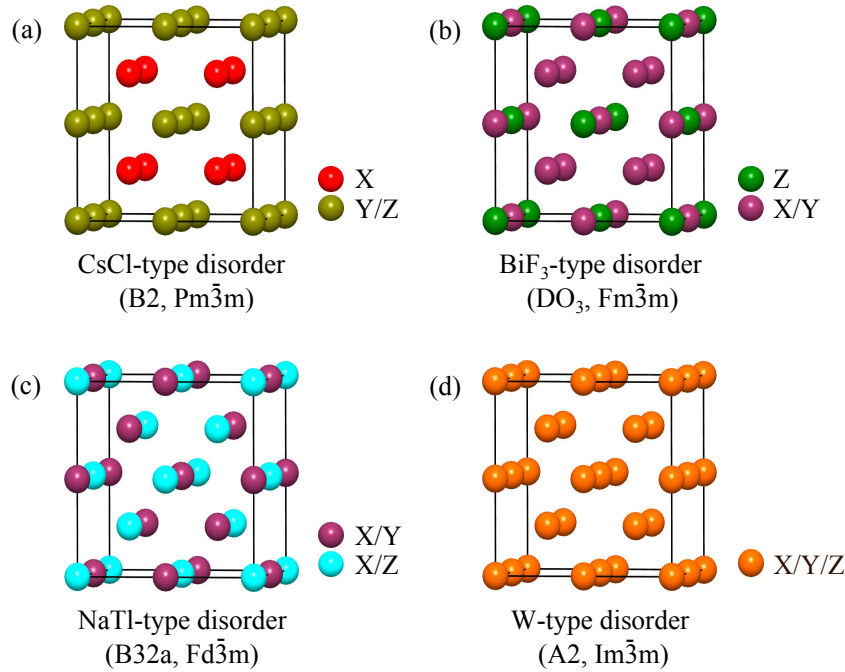
Figure 3.6: Most prominent disordered Heusler structures: (a) CsCl-type disorder, (b) BiF$_3$-type disorder, (c) NaTl-type disorder, and (d) W-type disorder.

to revolutionize the thriving field of information technology. Spintronics covers the field of devices that make use of not only the charge of electrons but also of their spin and therefore it is a promising approach to overcome the problem of the physical limit, namely the size of the structures.

In the last decade, spintronics has developed as a new approach that has revolutionized the market for electronic devices. Some predicted advantages of this new technology are the nonvolatility of data storage, the increased speed of data processing, the high storage density, and the low energy consumption [63].

In order to make use of the full potential of spintronics, new magnetic materials, magnetic semiconductors and so-called half-metallic ferromagnets (HFM) are needed. Half-metallic ferromagnets seem to be a suitable class of material which meet all requirements of spintronics. The most important reason is their exceptional electronic structure: They behave like metals for majority electrons and like semiconductors for minority electrons. Half-metallic ferromagnetic metals, such as Heusler compounds are potential candidates for spintronics applications.

Spintronics emerged from discoveries in the 1980s concerning spin-dependent electron transport phenomena in solid-state devices. This includes the observation of spin-polarized electron injection from a ferromagnetic metal to a normal metal by Johnson and Silsbee [64] and the discovery of giant magnetoresistance independently by Fert *et al.* [65] and Grünberg *et al.* [66]. Therefore, in the following, a short introduction into

the field of spintronic devices and magnetoresistance effects will be given.

3.6.1 Spintronic Devices

Conventional electronic devices rely on the transport of electrical charge carriers, electrons, in a semiconductor such as silicon. Now, however, physicists are trying to exploit the spin of the electron rather than its charge to create a remarkable new generation of spintronic devices which will be smaller, more versatile and more robust than those currently making up silicon chips and circuit elements. All spintronic devices act according to the simple scheme: (1) information is stored (written) into spins as a particular spin orientation (up or down), (2) the spins, being attached to mobile electrons, carry the information along a wire, and (3) the information is read at a terminal. Spin orientation of conduction electrons survives for a relatively long time (nanoseconds, compared to tens of femtoseconds during which electron momentum decays). Their non-volatile nature makes spintronic devices particularly attractive for memory storage and magnetic sensors applications, and, potentially for quantum computing where electron spin would represent a bit (called qubit) of information. Magnetoelectronics, spin electronics, and spintronics are different names for the same thing: the use of electrons spins (not just their electrical charge) in information circuits.

Nowadays, we are in contact with spintronics in our everyday life, in form of spin valves based on the GMR effect, which are used in magnetic hard disk drives [40]. A spin valve consists of two ferromagnetic layers sandwiching a thin nonmagnetic metal layer. One of the magnetic layers is pinned by an antiferromagnetic material, and is, therefore, insensitive to moderate magnetic fields; the second layer is free, i.e. its magnetization can be rotated by the application of small magnetic fields. GMR spin-valve based read heads consist of multilayer thin film material with alternating ferromagnetic and non magnetic metals. The current in a GMR device can either flow perpendicular to the interfaces (CPP, current-perpendicular-to-plane), or parallel to the interfaces (CIP, current-in-plane). The GMR was originally discovered in a CIP configuration; however the CPP configuration shows even larger effects.

New devices for spintronics which superseded the era of GMR are known as magnetic tunnel junctions (MTJs) or as tunneling magnetoresistance (TMR) devices. The metallic spacer in GMR devices is replaced by an insulating material in TMR devices and lead to an increase in magnetoresistance by a factor of 10, compared to GMR spin valves. Interestingly, the ultimate goal of spintronics, i.e. a tunneling device with a magnetoresistance effect of several thousand percent, can be reached by two different courses: One way is to engineer the insulation barrier, and the other way is to develop new electrode materials with 100% spin polarization. Potential candidates include half-metallic ferromagnetic oxides as well as half-metallic ferromagnets, such as

Heusler compounds.

3.6.2 Magnetoresistance

Magnetoresistance (MR) is a basic effect in spintronics, which is generally defined as the property of a material to change the value of its electrical resistance when an external magnetic field is applied to it. A large change in the electrical resistivity in response to an applied magnetic field is of technological relevance for the development of magnetic switching devices and magnetic memories.

The magnetoresistance effect was first discovered by William Thomson (more commonly known as Lord Kelvin) in 1856 [67], but he was unable to lower the electrical resistance of anything by more than 5%. This effect was later called ordinary magnetoresistance. He experimented with pieces of iron and discovered that the resistance increases when the current is in the same direction as the magnetic force and decreases when the current is at 90° to the magnetic force. He then did the same experiment with nickel and found that it was affected in the same way but the magnitude of the effect was greater. This effect is referred to as anisotropic magnetoresistance (AMR). AMR is the property of a material in which a dependence of electrical resistance on the angle between the direction of electric current and orientation of magnetic field is observed [68]. The effect is attributed to a larger probability of s-d scattering of electrons in the direction of the magnetic field. The net effect is that the electrical resistance has its maximum value when the direction of current is parallel to the applied magnetic field.

From the time of discovery of anisotropic magnetoresistance until 1988, AMR remained the most important contribution to the magnetoresistance of ferromagnets. More recently researchers discovered materials showing giant magnetoresistance (GMR), colossal magnetoresistance (CMR) and magnetic tunnel effect (TMR). Due to the importance of these types of magnetoresistance in the information technology a short introduction into this field is given in the following.

3.6.2.1 Giant Magnetoresistance (GMR)

The discovery of the giant magnetoresistance (GMR) effect in magnetic multilayers and sandwiches in 1986 by P. Grünberg [66] and A. Fert [65] is considered as the birth of spintronics. The giant magnetoresistance effect observed in thin film structures composed of alternating ferromagnetic and non magnetic layers and is used in magnetic sensors and in nearly every hard disc read head. The effect is observed as a significant change in the electrical resistance depending on whether the magnetization of adjacent ferromagnetic layers are in a parallel or an antiparallel alignment. Figure 3.7 shows an example of such a multilayer Fe-Cr-Fe systems [65]. The overall resistance is relatively

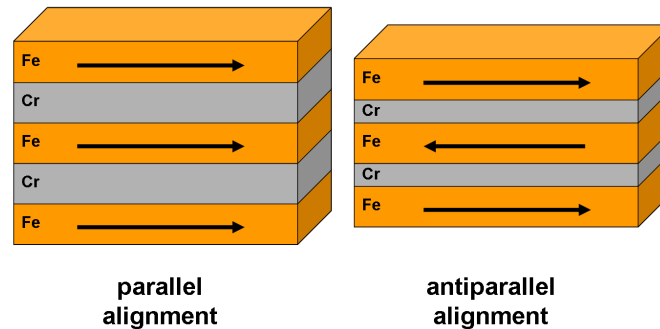low for parallel alignment and relatively high for antiparallel alignment.

Figure 3.7: A multilayer system Fe-Cr-Fe with ferromagnetic (left) and antiferromagnetic (right) exchange coupling between the iron layers.

Different types of giant magnetoresistance include multilayer GMR, spin valve GMR, pseudo-spin valve and granular GMR. As the GMR read head sensor in a hard disk is built using a spin valve in following the spin valve GMR is briefly explained.

3.6.2.2 Spin Valve Giant Magnetoresistance

In spin valve giant magnetoresistance a nonmagnetic spacer layer is sandwiched between two ferromagnetic electrodes. Two types of configurations are observed in these ferromagnetic layers, an antiparallel configuration and a parallel configuration which are shown in Figure 3.8. In this figure, the electron path is represented by arrows across the spin valves. A kink in the path displays the scattering of electrons. During passing through the spin valve, an electron will be scattered if its spin is opposite to the direction of the majority spins in the ferromagnetic layer which causes higher resistivity. Therefore, the overall resistance for the antiparallel alignment is higher than the resistance for the parallel alignment.

3.6.2.3 Colossal Magnetoresistance (CMR)

Colossal Magnetoresistance (CMR) was discovered by R. von Helmolt *et al.* [69] and Jin *et al.* [70] in 1993 and is a property of some materials which enable them to modify their electrical resistance in the presence of a magnetic field by orders of magnitude. The CMR effect is observed mostly in manganese-based perovskite oxides. Although this effect is large in manganites they are not suitable candidates for application due to their temperature dependence (only small effect at room temperature) and their sensitivity (magnetoresistance ratio in small fields).
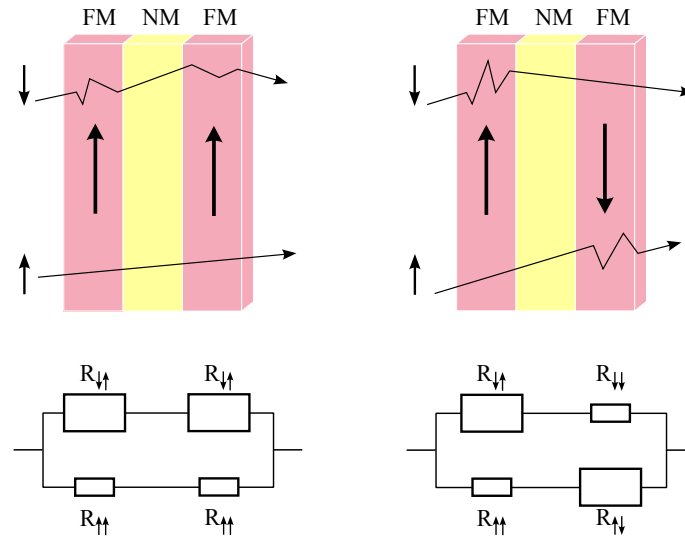
Figure 3.8: Scheme of the spin-valve GMR. A parallel configuration of magnetic mo-
ments is shown on the left and an antiparallel configuration on the right.
↑ is a spin-up electron and ↓ is a spin-down electron, NM stands for non-
magnetic metal, FM for ferromagnetic metal. The vertical black arrows in
the ferromagnetic layers display the direction of the majority spins and the
thin lines across the spin valves present the electron path. A kink in the
path shows the scattering of an electron. The size of resistors in electric
circuits shows the amount of resistance (schematic).

3.6.2.4 Tunnel Magnetoresistance (TMR)

When two ferromagnetic layers are separated by a thin insulator layer (see Figure 3.9),
the tunnel magnetoresistance effect based on the tunneling of electrons through the
insulating barrier occurs. In this situation, the electrical resistance of the multilayer
in the perpendicular direction to the film changes depending on the orientations of the
magnetizations of ferromagnetic thin layers. When the directions of the magnetizations
of the two ferromagnetic electrodes are the same, the probability of electron tunneling
between the two ferromagnetic electrodes through the insulator layer becomes larger,
resulting in a larger tunneling current. However, if the directions of the magentiza-
tions of the two ferromagnetic electrodes are opposite, the electron with opposite spin
orientation with respect to the majority spins of the ferromagnetic electrode cannot
tunnel. Then the tunneling electron current becomes smaller compared to the case
for the same direction of the magnetizations. This phenomenon is called tunneling
magnetoresistance (TMR) [71] and was originally discovered by Jullire in 1975 [72].
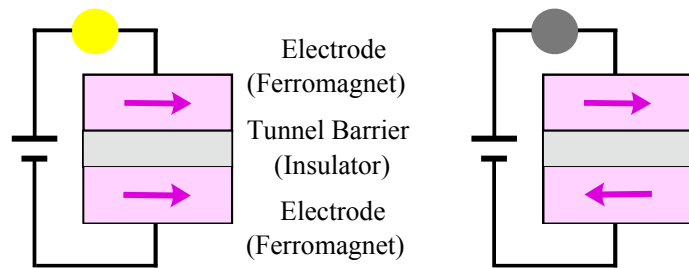
Figure 3.9: Tunnel magnetoresistance (TMR) effect in a magnetic tunnel junction
(MTJ) device. When the magnetizations are aligned parallel (left) the de-
vice resistance is small and when they are aligned antiparallel (right), the
device resistance is large.

3.6.2.5 Spin-Transfer Switching and Spin Torque Devices

In 1996, Slonczewski [73] and Berger [74] independently predicted the spin-transfer
effect, where magnetization orientations in magnetic multilayers can be manipulated
via a spin polarized current instead of an external magnetic field. The spin-transfer
phenomena occur for an electron current flowing through two ferromagnetic layers sep-
arated by a thin nonmagnetic spacer layer. The current becomes spin polarized by
transmission through or reflection from the first ferromagnetic layer (the pinned refer-
ence layer) and mostly maintains this polarization as it passes through the nonmagnetic
spacer and enters and interacts with the second ferromagnetic layer (the free layer).
This interaction exerts a spin torque on the magnetic moment of the free layer through
a transfer of angular momentum from the polarized current to the magnetization of
the free layer. This spin torque can oppose the intrinsic damping of the free layer
causing a magnetization precession or can reverse the direction of the magnetization
with sufficient current strength. A schematic figure of spin transfer switching is shown
in Figure 3.10. Spin-transfer can have important implications for electronic devices
since it provides a local means of magnetization manipulation rather than using the
non-local character of magnetic fields.

The STT-MRAM technology is one of the most important applications of the spin-
transfer switching phenomena and has significant advantages over magnetic-field-switched
MRAMs. High speed of writing, local addressing, scalability, low power consumption,
non volatility, unlimited endurance, and simpler cell architecture are the most impor-
tant advantages of the STT-MRAM [75].

The main challenge for implementing the STT writing mode is achieving a low STT
write current density J_{c0} required to switch the magnetization of the free layer and high
thermal stability required for long-term data retention at the same time.

The intrinsic current density J_{c0} required for switching the magnetization in multiples
of A/cm^2 is expressed as
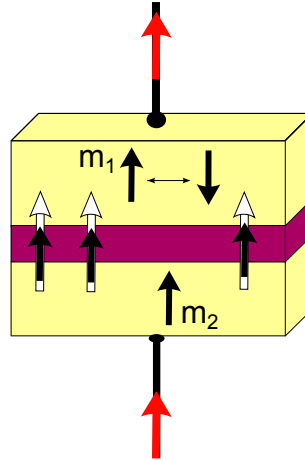
Figure 3.10: Spin transfer switching. Two ferromagnetic layers separated by a thin nonmagnetic layer. m_1 and m_2 denote the direction of the majority spins in the free layer and pinned reference layer, respectively. The white arrows show the spin polarized current. The direction of the magnetization in the free layer (m_1) can be reversed with sufficient current strength as indicated by the double-headed arrow.

$$J_{c0} = \frac{2e}{h} \frac{\alpha}{g(\theta)} K_u^{eff} d \qquad (3.7)$$

where e is the charge of the electron, h is the Planck constant, α is the damping constant, $g(\theta)$ is the spin polarization, K_u^{eff} is the perpendicular magnetic anisotropy, and d is the free layer thickness.

The thermal stability factor is given by

$$\Delta = \frac{K_u^{eff} V}{K_B T} \qquad (3.8)$$

Where V is the volume of the free layer, K_B is the Boltzmann constant, and T is the temperature.

According to equations 3.7 and 3.8 materials with high spin polarization, low magnetic damping, low saturation magnetization, and high perpendicular anisotropy are suitable for spin-torque devices.

3.7 Structure of This Thesis

This work is divided into two parts: part 1 is focused on the prediction of half-metallicity in quaternary Heusler compounds and their potential for spintronic applications and part 2 on the structural properties of Mn_2-based Heusler alloys and tuning the magnetism of them from soft to hard-magnetic for spin-transfer torque applications.

In part 1, three different series of quaternary Heusler compounds are investigated, XX'MnGa (X = Cu, Ni and X' = Fe, Co), CoFeMnZ (Z = Al, Ga, Si, Ge), and $Co_{2-x}Rh_xMnZ$ (Z= Ga, Sn, Sb). In this section all the quaternary Heusler compounds have been identified using a theoretical approach for preselection and the half metallic ferromagnets are predicted. For the XX'MnGa class of compounds as predicted by calculations we have found that NiFeMnGa and NiCoMnGa are half-metallic ferromagnets (HMF). These are the first reported Ni based half-metallic ferromagnets within the huge family of Heusler compounds. CuCoMnGa turned out to be a regular metallic ferromagnet due to the closed shell character of the Cu d electrons. NiFeMnGa has a Curie temperature, that is too low to make it relevant for technological applications but NiCoMnGa with a high spin polarization, magnetic moment, and Curie temperature is an interesting new material for spintronics applications. The quaternary intermetallic Heusler compounds CoFeMnZ (Z = Al, Ga, Si, or Ge) were identified as potential half-metallic ferromagnets with high T_C by ab- initio electronic structure calculations. All compounds exhibit a cubic Heusler structure. The magnetic moments of the compounds are in fair agreement with the Slater-Pauling rule indicating the half-metallicity and high spin polarization required for spintronics applications. The Curie temperatures of all compounds are 553 K or higher allowing for utilization at room temperature and above. The quaternary Heusler compounds $Co_{2-x}Rh_xMnZ$ (Z = Ga, Sn, Sb) are also predicted by ab initio electronic structure calculations to be HMF. The structural investigation revealed that the crystal structure of all compounds aside from CoRhMnSn exhibit different types of anti-site disorder. The magnetic moments of the disordered compounds deviate to different amounts from the Slater-Pauling rule indicating that 100% spin polarization are not realized in CoRhMnGa, CoRhMnSb, and in the alloy $Co_{0.5}Rh_{1.5}MnSb$. Exchange of one Co in Co_2MnSn by Rh results in the stable, well-ordered compound CoRhMnSn. This exchange of one of the magnetic Co atoms by a non-magnetic Rh atom keeps the magnetic properties and half-metallicity intact. Those properties are completely determined by the Mn atoms together with valence electron count and do not depend much on the remaining type of atoms. This behavior allows to increase the spin-orbit interaction at one of the sites while keeping all other properties as a precondition for applications and physical effects relying on a large spin-orbit interaction.

In part 2, two series of Mn_2-based Heusler alloys are investigated, $Mn_{3-x}Co_xGa$ and $Mn_{2-x}Rh_{1+x}Sn$. It has been shown that the series $Mn_{3-x}Co_xGa$ crystallizes in the inverse tetragonal structure ($I\bar{4}m2$, space group no. 119), for $x = 0.1 - 0.4$, in the cubic inverse Heusler $CuHg_2Ti$ structure type ($F\bar{4}3m$, space group no. 216), for $x = 0.6 - 1$ and in both cubic and tetragonal phases for $Mn_{2.5}Co_{0.5}Ga$. In this series, while the tetragonal alloys, hard magnets, exhibit the features typically attractive for STT applications (high Curie temperature and low saturation magnetic moment), the cubic

systems, soft magnets, present 100% spin polarized materials (or half-metals) obeying the Slater-Pauling rule. A continuous tunability of magnetic and structural properties simply depending on the Co concentration can easily be realized in these materials. In $Mn_{2-x}Rh_{1+x}Sn$ series, Mn_2RhSn crystallizes in the inverse tetragonal structure ($I\bar{4}m2$, space group no. 119) and shows a hard-magnetic hysteresis loop at low temperature. As Mn_2RhSn has a tetragonal structure, it does not follow the Slater-Pauling rule. With substituting Mn by Rh, the inverse cubic structure for $Mn_{2-x}Rh_{1+x}Sn$ (x = 0.5, 0.6, 0.8) and regular cubic structure for Rh_2MnSn are observed. All cubic samples show perfect Slater-Pauling behavior and a soft hysteresis loop at room and low temperature. Both cubic and tetragonal phases exist for $Mn_{1.8}Rh_{1.2}Sn$ and it shows similar magnetic properties as Mn_2RhSn.

4 List of publications

a) This thesis is based on the publications

1. *Quaternary half-metallic Heusler ferromagnets for spintronics applications*
V. Alijani, J. Winterlik, G. H. Fecher, S. S. Naghavi, and C. Felser
Phys. Rev. B. 83, 184428 (2011)

2. *Electronic, structural, and magnetic properties of the half-metallic ferromagnetic quaternary Heusler compounds CoFeMnZ (Z = Al, Ga, Si, Ge)*
V. Alijani, S. Ouardi, G. H. Fecher, J. Winterlik, S. S. Naghavi, X. Kozina, G. Stryganyuk, C. Felser, E. Ikenaga, Y. Yamashita, S. Ueda, and K. Kobayashi
Phys. Rev. B. 84, 224416 (2011)

3. *Quaternary Heusler compounds $Co_{2-x}Rh_xMnZ$ (Z= Ga, Sn, Sb): crystal structure, electronic structure, and magnetic properties*
V. Alijani, J. Winterlik, G. H. Fecher, S. S. Naghavi, S. Chadov, T. Gruhn, and C. Felser
J. Phys.: Condens. Matter. 24, 046001 (2012)

4. *Tuning the magnetism of the Heusler alloys $Mn_{3-x}Co_xGa$ from soft and half-metallic to hard-magnetic for spin-transfer torque applications*
V. Alijani, J. Winterlik, G. H. Fecher and C. Felser
Appl. Phys. Lett. 99, 222510 (2011)

b) Further publications

5. *Electronic, magnetic, and structural properties of the ferrimagnet Mn_2CoSn*
J. Winterlik, G. H. Fecher, B. Balke, T. Graf, V. Alijani, V. Ksenofontov, C. A. Jenkins, O. Meshcheriakova, C. Felser, G. Liu, S. Ueda, K. Kobayashi, T. Nakamura, and M. Wjcik
Phys. Rev. B. 83, 174448 (2011)

6. *Disentangling the Mn moments on different sublattices in the half-metallic ferrimagnet $Mn_{3-x}Co_xGa$*

P. Klaer, C. A. Jenkins, V. Alijani, J. Winterlik, B. Balke, C. Felser, and H. J. Elmers
Appl. Phys. Lett. 98, 212510 (2011)

7.   *Element specific magnetic moments and spin-resolved density of states in CoFeMnZ (Z = Al, Ga; Si, Ge)*
P. Klaer, B. Balke, V. Alijani, J. Winterlik, G. H. Fecher, C. Felser, and H. J. Elmers
Phys. Rev. B. 84, 144413 (2011)

8. *Theoretical study of new acceptor and donor molecules based on polycyclic aromatic hydrocarbons*
S. S. Naghavi, T. Gruhn, V. Alijani, G. H. Fecher, C. Felser, K. Medjanik, D. Kutnyakhov, S. A. Nepijko, G. Schönhense, R. Rieger, M. Baumgarten, and K. Müllen
J. Mol. Spec. 265, 95 (2011)

9. *Electronic structure of large disc-type donors and acceptors*
K. Medjanik, D. Kutnyakhov, S. A. Nepijko, G. Schönhense, S. Naghavi, V. Alijani, C. Felser, R. Rieger, M. Baumgarten, and K. Müllen
Phys. Chem. Chem. Phys. 12, 7184 (2010)

10. *Composites of graphene with large aromatic molecules*
Q. Su, S. Pang, V. Alijani, C. Li, X. Feng, and K. Müllen
Adv. Mater. 21, 3191 (2009)

11. *Di- and triorganotin(IV) carboxylates derived from triorganotin(IV) iodide with mixed organic groups on tin: Cyclic, hexameric triorganotin(IV) carboxylates*
M. M. Amini, A. Azadmehr, V. Alijani, H. Khavasi, T. Hajiashrafi, and A. Nemati Kharat
Inorganica Chimica Acta. 362, 355 (2009)

12. *A hexagonal modification of catena-poly[[ethyldiphenyltin(IV)]-μ-2-chloroacetato-$\kappa^2 O{:}O'$]*
M. M. Amini, V. Alijani, A. Azadmehr, and S. W. Ng
Acta Cryst. E63, m913 (2007)

13. *catena-Poly[[ethyldiphenyltin(IV)]-μ-dichloroacetato-$\kappa^2 O{:}O'$]*
M. M. Amini, V. Alijani, A. Azadmehr, and S. W. Ng
Acta Cryst. E62, m2427 (2006)

14. *catena-Poly[[diphenylethyltin(IV)]-μ-chloroacetato-$\kappa^2 O{:}O'$]*
M. M. Amini, V. Alijani, A. Azadmehr, H. Khavasi, and S. W. Ng
Acta Cryst. E62, m2028 (2006)

5 Calculational details

The electronic structures of all quaternary compounds were calculated by means of the full potential linearized augmented plane wave (FLAPW) method as implemented in WIEN2k provided by Blaha, Schwartz, and coworkers [76, 77, 78]. The exchange-correlation functional was taken within the generalized gradient approximation (GGA) in the parameterization of Perdew, Burke and Enzerhof [79]. A $25 \times 25 \times 25$ point mesh was used as base for the integration in the cubic systems resulting in 455 k-points in the irreducible wedge of the Brillouin zone. The energy convergence criterion was set to 10^{-5} Ry and simultaneously the criterion for charge convergence to $10^{-3} e^-$. The muffintin radii were set to 2.5 a_{0B} (a_{0B} = Bohr's radius) for the transition metals as well as the main group elements.

For XX'MnGa (X = Cu, Ni and X' = Fe, Co) compounds, further electronic structure calculations were carried out using the full relativistic spin polarized Korringa - Kohn - Rostocker method (SPRKKR) provided by Ebert *et al* [80, 81, 82]. This program provides the coherent potential approximation (CPA) for calculating the properties of alloy systems with random distribution of the atoms. The SPRKKR calculations were performed using the PBE generalized gradient approximation [79]. The CPA tolerance was set to 10^{-4} and the energy convergence criterion to 10^{-5}. f-states were included in the basis of all atoms. 832 irreducible k-points based on a $22 \times 22 \times 22$ mesh were used for integration. The density of states is calculated for the double number of k-points from the Greens function by adding a small imaginary part of 0.002 Ry to the energy. For smaller values, the band gaps may become better visible, however, at the same time the DOS becomes much more noisy.

Furthermore, the stability of all quaternary cubic structures was checked by calculation of the elastic constants c_{ij}. The elastic constants were calculated by applying isotropic strain as well as volume conserving tetragonal and rhombohedral strains to the optimized cubic primitive cell. There are only three independent components for cubic symmetry: $c_{11} = c_{22} = c_{33}$, $c_{12} = c_{13} = c_{23}$, and $c_{44} = c_{55} = c_{66}$. The bulk modulus of cubic systems is derived from $B = (c_{11} + 2c_{12})/3$. The elastic stability criteria of the cubic structure are found from the elastic constants [83]. For stability of the cubic structure, the bulk modulus, the c_{44}-shear modulus, and the tetragonal shear modulus must be positive resulting in the following conditions: $c_{11} + 2c_{12} > 0$, $c_{44} > 0$, and $c_{11} - c_{12} > 0$. The elastic anisotropy $A_e = 2c_{44}/(c_{11} - c_{12})$ compares the

shear moduli and furthermore allows a decision about the structural stability. Youngs modulus becomes isotropic for $A_e = 1$. Materials with large A_e ratios show a tendency to deviate from the cubic structure.

6 Experimental details

All polycristalline samples were prepared by repeated arc melting of stoichiometric amounts of high purity constituents in an argon atmosphere. Special care has to be taken to avoid oxygen contamination, in particular in case of materials containing elements with a high oxygen affinity, such as manganese. As the surface of mangenese can absorb a lot of oxygen, it was melted several times to remove the oxygen from the surface of it and obtain metallic ingots. To avoid oxygen contamination during the melting a Ti sponge was used as an oxygen absorber before melting the compounds as well as by additional purifying of the process gas. The samples were melted three to four times from both sides to ensure sufficient homogeneity. To improve the crystal structure as well as the phase purity the resulting polycrystalline ingots were annealed in evacuated quartz tubes at 800°C for quaternary Heusler alloys and at 850°C for Mn_2-based Heusler compounds for two weeks and quenched afterward into a bath of an ice/water mixture.

The crystallographic structure was investigated by X-ray powder diffraction (XRD) using a Bruker D8 powder diffractometer equipped with a Mo K_α X-ray tube for $XX'MnGa$ (X = Cu, Ni and X' = Fe, Co), CoFeMnZ (Z = Al, Ga, Si, Ge) and $Co_{2-x}Rh_xMnZ$ (Z = Ga, Sn) series and a Seifert XRD 3003 PTS powder diffractometer equipped with a Cu K_α X-ray tube for $Co_{2-x}Rh_xMnSb$ (x = 1, 1.5) and Mn_2-based Heusler compounds. Rietveld refinements of the data were performed using the TOPAS ACADEMIC software package for all compounds. For the XRD measurements cut disks of the samples were ground to fine powder and processed immediately to avoid oxidation. Also flat disks were cut from the ingots and polished for spectroscopic investigations of the bulk samples.

The magnetic properties of the samples were investigated by means of a super conducting quantum interference device (SQUID, Quantum Design MPMS-XL-5) using small spherical sample pieces of approximately 5-10 mg.

The compounds with Z = Si and Ge in CoFeMnZ series were investigated by means of photoelectron spectroscopy. The measurements were carried out at different excitation energies in order to investigate the influence of varying cross sections. For the hard X-ray photoemission spectroscopy (HAXPES) measurements, polished discs of the samples were fractured in-situ in an ultrahigh vacuum chamber before the respective measurements to avoid surface contamination due to air exposure. The experiments

were carried out at the beamlines BL15XU [84] and BL47XU of SPring-8 in Japan. At BL15XU, the photon energy was fixed at 5.9534 keV using a Si (111) double crystal monochromator (DCM) and the 333 reflection of a Si channel cut post monochromator. At BL47XU, the photon energy was fixed at 7.9392 keV using a Si(111) DCM and the 444 reflection of the channel cut post monochromator. At both beamlines, the photoelectrons were analyzed and detected by means of hemispherical analyzers (VG Scienta, R4000). The overall energy resolution (monochromator plus analyzer) was set to 240 meV, as verified by spectra of the Au valence band at Fermi energy (ϵ_F). Additionally, spectra were recorded with a resolution of 150 meV. The angle between the electron spectrometer and photon propagation is fixed at $90°$. The photons are p-polarized, $i.\ e.$ the electric field vector is in the plane of incidence and always points in the direction of the electron detector. A nearly normal emission ($\theta \approx 2° \dots 5°$) angle was used for electron detection (Note that the angle is not that well defined for fractured bulk samples due to surface roughness.) The measurements were performed at sample temperatures of 300 K. The core level spectra were analyzed using the program UNIFIT 2011 [85].

7 Quaternary Heusler Alloys

7.1 Quaternary Half-Metallic Heusler Ferromagnets for Spintronics Applications

7.1.1 Introduction

The $T_2T'M$ (T, T' = transition metals, M = main group element) Heusler compounds are ternary intermetallics with a 2:1:1 stoichiometry [27, 38]. They attracted interest of the magnetism community when F. Heusler *et al.* [26, 27] had shown that the compound Cu_2MnAl becomes ferromagnetic, even though none of its constituents is ferromagnetic by itself. Interest in the Heusler compounds has increased since it has been established that their properties can easily be altered by substitution of elements. Co_2-based compounds were already synthesized and investigated in the 1960s and 70s [86, 87]. Later the predicted half-metallic ferromagnets came into the center of attention [28, 29]. Today Heusler compounds are used for various applications in the research fields of spintronics [63], thermoelectrics [88, 89], and superconductors [90]. Quaternary half-metallic Heusler compounds are yet very rarely investigated. A multitude of compounds of this class with interesting properties can thus be uncovered using appropriate tools for exploration. We have used *ab initio* electronic structure calculations to identify interesting half-metallic compounds for spintronics applications. In the current work we present the results of theoretical, structural, and magnetic investigations of the unreported half-metallic quaternary Heusler ferromagnets NiFeMnGa and NiCoMnGa. These are actually the first Ni-based half-metallic ferromagnets reported up to now. We have also characterized the unreported quaternary Heusler compound CuCoMnGa. This compound is, however, of minor technological importance because the closed d shell of copper inhibits half-metallic ferromagnetism.

7.1.2 Calculational Details

The electronic structures of the compounds were calculated by means of the full potential linearized augmented plane wave (FLAPW) method as implemented in WIEN2k provided by Blaha, Schwartz, and coworkers [76, 77, 78]. The exchange-correlation functional was taken within the generalized gradient approximation (GGA) in the parameterization of Perdew, Burke and Enzerhof [79]. A $25 \times 25 \times 25$ point mesh was

used as base for the integration in the cubic systems resulting in 455 k-points in the irreducible wedge of the Brillouin zone. The energy convergence criterion was set to 10^{-5} Ry and simultaneously the criterion for charge convergence to $10^{-3}e^-$. The number of plane waves was restricted by $R_{MT}k_{max} = 7$ (R_{MT} is muffin-tin radius). A convergence test for NiFeMnGa as well as many other Heusler compounds [35] revealed that this criterion is sufficient for systems with $L2_1$, X, Y, or $C1_b$ structure, due to the closed packing of these fcc type structures. The muffin tin radii were set to 2.5 a_{0B} ($a_{0B} :=$ Bohr's radius) for the transition metals as well as the main group elements.

Further electronic structure calculations were carried out using the full relativistic spin polarized Korringa - Kohn - Rostocker method (SPRKKR) provided by Ebert *et al* [80, 81, 82]. This program provides the coherent potential approximation (CPA) for calculating the properties of alloy systems with random distribution of the atoms. The SPRKKR calculations were performed using the PBE generalized gradient approximation [79]. The CPA tolerance was set to 10^{-4} and the energy convergence criterion to 10^{-5}. f-states were included in the basis of all atoms. 832 irreducible k- points based on a $22 \times 22 \times 22$ mesh were used for integration. The density of states is calculated for the double number of k-points from the Greens function by adding a small imaginary part of 0.002 Ry to the energy. For smaller values, the band gaps may become better visible, however, at the same time the DOS becomes much more noisy.

7.1.3 Electronic structure

Starting point for the electronic structure calculations was an optimization of the cubic structure, *i. e.* a search of the minimum total energy as a function of the lattice parameter and site occupation. For all three compounds, the optimization of the cubic lattice parameter revealed the lowest energy for the structure with M on Wyckoff position 4a, T' on 4b, T on 4c and T'' on 4d on the lattice with space group $F\,\overline{4}3m$ (see Section 7.1.4). Starting for example with opposite moments at the Mn and Co sites of CuCoMnGa, the calculations always converged into a state with parallel moments at Co and Mn, *i .e.* no ferrimagnetic ground state was observed for one of the three structures. The dependence of the total energy on the crystal structure and the lattice parameter is shown in Figure 7.1.

Furthermore, the stability of the cubic structure was checked by calculation of the elastic constants c_{ij}. The three independent elastic constants of the cubic structure (c_{11}, c_{12}, and c_{44}) were calculated by applying isotropic strain as well as volume conserving tetragonal and rhombohedral strains to the optimized primitive cubic cell.

The results of the calculated elastic properties are summarized in Table 7.1. As a result of a negative tetragonal shear modulus ($c_{11} - c_{12}$), the elastic anisotropy of CuCoMnGa becomes also negative. This clearly points on a structural instability of

CuCoMnGa, whereas the Ni-containing compounds turned out to be structurally stable.
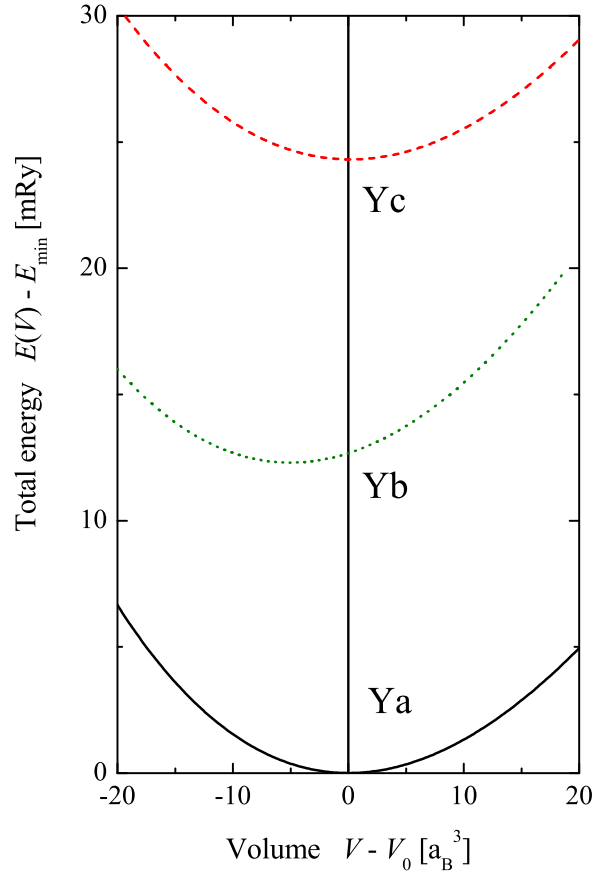
Figure 7.1: Structure dependence of the total energy of CuCoMnGa. Shown is the volume dependence of the total energy for the three possible different site occupations Ya: CuCoMnGa, Yb: CoMnCuGa, and Yc: CuMnCoGa.

Table 7.1: Elastic constants of NiFeMnGa, NiCoMnGa, and CuCoMnGa. The optimized lattice parameter a_{calc} is given in Å, all values c_{ij} and the bulk modulus B are given in GPa, The elastic anisotropy $A_e = 2c_{44}/(c_{11} - c_{12})$ is dimensionless.

Compound	a_{calc}	c_{11}	c_{12}	c_{44}	B	A_e
NiFeMnGa	5.755	208	176	151	186	9.4
NiCoMnGa	5.784	186	172	119	177	17
CuCoMnGa	5.846	65	184	153	144	-2.6

Figure 7.2 shows the calculated band structure and density of states of NiFeMnGa.

It is evident that the compound exhibits a half-metallic ferromagnetic band structure, the minority channel shows a gap at the Fermi energy. NiCoMnGa was also identified to exhibit a half-metallic ferromagnetic ground state. CuCoMnGa in contrast to these findings has states at the Fermi energy in both spin directions and is thus a normal metal. Figure 7.3 shows the corresponding band structure and density of states for comparison. Table 7.2 summarizes the magnetic moments obtained from the electronic structure calculations.

Figure 7.2: Band structure and density of states of NiFeMnGa. (a) minority bands, (b) density of states, (c) majority bands. Majority and minority spin densities are assigned by ↑ and ↓, respectively.

Table 7.2: Calculated magnetic moments of NiFeMnGa, NiCoMnGa, and CuCoMnGa. Note that the Mn atoms in this structure correspond to T' and occupy the Wyckoff position 4b.

TT''MnGa	$m_{\text{tot}}\ [\mu_B]$	$m_T\ [\mu_B]$	$m_{T''}\ [\mu_B]$	$m_{\text{Mn}}\ [\mu_B]$
NiFeMnGa	4.01	0.47	0.79	2.84
NiCoMnGa	5.07	0.59	1.22	3.26
CuCoMnGa	4.32	0.08	0.97	3.27

For CuCoMnGa, calculations were performed assuming different types of anti-site disorder. Besides the ordered Y-type structure, the $A2$ ($I\,m\bar{3}m$, W-type), $B2$ ($P\,m\bar{3}m$,
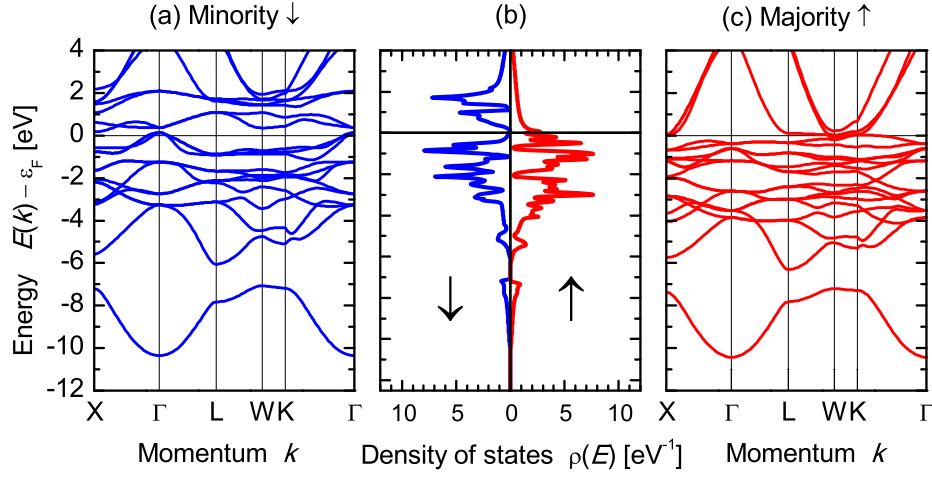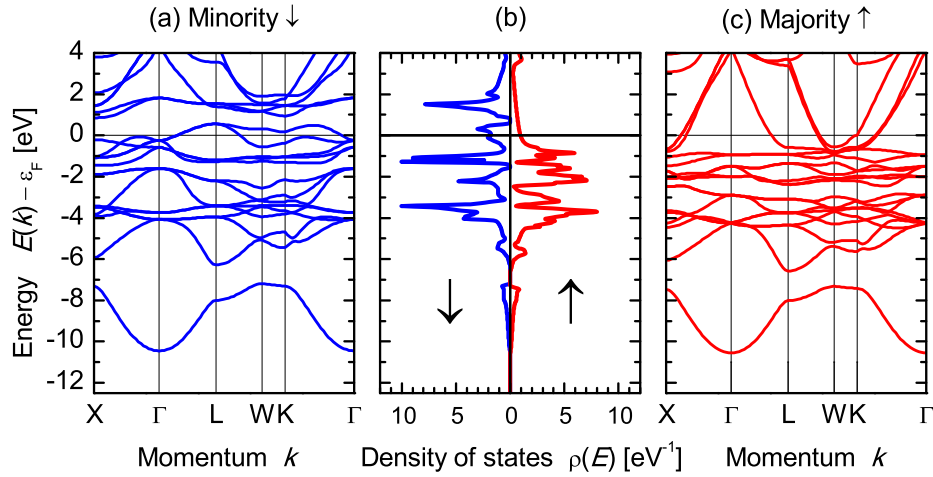
Figure 7.3: Band structure and density of states of CuCoMnGa. (a) minority bands, (b) density of states, (c) majority bands. Majority and minority spin densities are assigned by ↑ and ↓, respectively.

CsCl-type), and a disordered $L2_1$ ($Fm\bar{3}m$, Cu$_2$MnAl-type) variation were assumed (see also Ref. [48]). In $A2$, all sites are randomly occupied by one quarter of the different atom types. For $B2$ it was assumed that Co and Cu are distributed on one site of the CsCl cell and Mn and Ga on the second site. For the disordered $L2_1$ structure Cu and Co randomly occupy the 8c Wyckoff position of the $Fm\bar{3}m$ lattice, while Mn and Ga occupy the positions 4b and 4a, respectively. The KKR-CPA method was used to account for the random site occupation. The lattice parameter was set to $a = 5.846$ Å in all four cases.

Figure 7.4 compares the density of states of well-ordered Y-type CuCoMnAl to the three major disordered variations of the cubic structure: $L2_1$, $B2$, and $A2$. It is seen that the density of states becomes smeared out with an increasing degree of disorder. In the $B2$ and $A2$ structures, even the Heusler-typical hybridization gap (seen at about -6.6 eV for Y and $L2_1$), which separates the low-lying s bands from the higher-lying p and d bands, vanished. The Fermi energy is located in a minimum of the total density in the $L2_1$ and $B2$ type structures. This may stabilize or enhance these types of disorder in the compound. The Fermi energy is also trapped in or close to a minimum of the minority density of states. This behavior stabilizes the magnetic moments at approximately 4 μ_B.
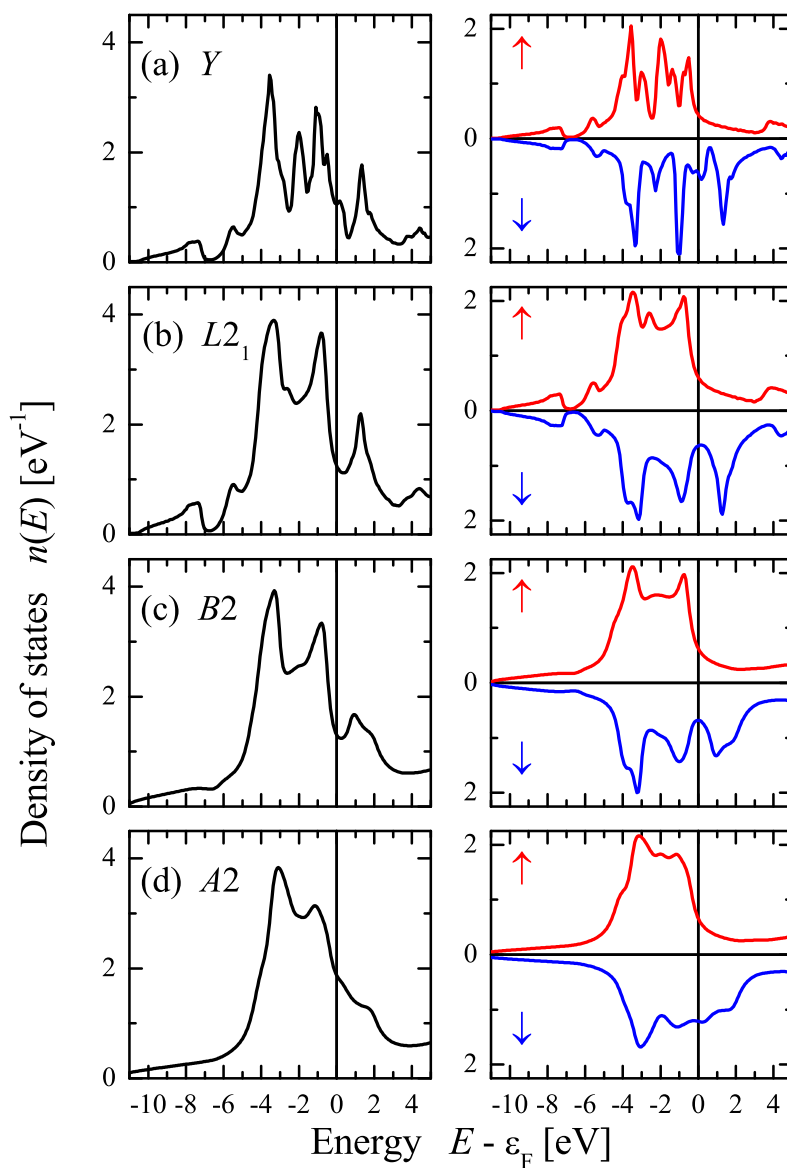
Figure 7.4: Electronic structure of disordered CuCoMnGa. Compared is the total and
spin-resolved density of states for the ordered compound (a) and 3 possi-
ble types of disorder $L2_1$ (b), $B2$ (c) and $A2$ (d). Majority and minority
densities are assigned by up and down arrows, respectively.

Table 7.3 compares the magnetic moments in the disordered and ordered structures assumed for CuCoMnGa. The total spin magnetic moments stay, independent of the structure, at approximately 4 μ_B with respect to the fcc primitive cell with a basis of four atoms. The magnetic moment in the Y structure using SPRKKR is slightly smaller as in the FLAPW calculations, where the moment at the Co site was slightly higher. This is due to the neglection of the full symmetry potential in the SPRKKR method used here.

Table 7.3: Calculated magnetic moments of disordered CuCoMnGa. Total spin moments of $A2$ and $B2$ are given for the primitive cell of the Y structure. Site resolved moments are given per atom.

	Symmetry	$m_{\text{tot}}\,[\mu_B]$	$m_{\text{Co}}\,[\mu_B]$	$m_{\text{Mn}}\,[\mu_B]$
$A2$	$I\,m\bar{3}m$	4.09	1.42	2.69
$B2$	$P\,m\bar{3}m$	4.17	0.91	3.26
$L2_1$	$F\,m\bar{3}m$	4.08	0.87	3.25
Y	$F\,\bar{4}3m$	3.98	0.7	3.28

7.1.4 Structural Characterization

Various types of ordered and disordered structures of Heusler compounds were discussed by Bacon and Plant [48]. The $L2_1$ structure of the ternary Heusler compounds with a 2:1:1 stoichiometry is a perfect 2^3 CsCl superstructure. The T_2 atoms form a primitive cubic sublattice and adjacent cubes of this T_2 sublattice are filled alternating by T' or M atoms (see Figure 7.5(a)). The primitive cell of the $L2_1$ structure contains four atoms that form the base of the fcc primitive cell. The result is a lattice with the $F\,m\bar{3}m$ symmetry, where the Wyckoff positions 4a (0, 0, 0), 4b (1/2, 1/2, 1/2), and 8c (1/4, 1/4, 1/4) are occupied by M, T', and T_2, respectively. The simple cubic sublattice is lost if one of the T_2 atoms is replaced by a third type of transition metal T''. At the same time, the symmetry is lowered to $F\,\bar{4}3m$ (the center of inversion is removed in this symmetry). In this so-called Y structure the Wyckoff positions 4a (0, 0, 0), 4b (1/2, 1/2, 1/2), 4c (1/4, 1/4, 1/4), and 4d (3/4, 3/4, 3/4) are occupied by M, T', T, and T'', respectively (see Figure 7.5(c)). The prototype of this structure is LiMgPdSn. Transforming the quaternary 1:1:1:1 compound back to a ternary by replacing T' by T does not change the $F\,\bar{4}3m$ symmetry (see Figure 7.5(b)). This transformation leads to so-called X structure, which often appears for Heusler compounds when the ordinal number of the T' element is larger than the one of the T element ($Z(T') > Z(T)$) and both elements are from the same period (*i. e.* 3d transition metals). It should be mentioned that all three structure types are converted into a simple bcc structure ($A2$,

$I\,m\bar{3}m$) when all four positions are filled with identical atoms. This is in particular the case for Heusler compounds with a random occupation of all lattice sites, *i. e.* complete disorder.
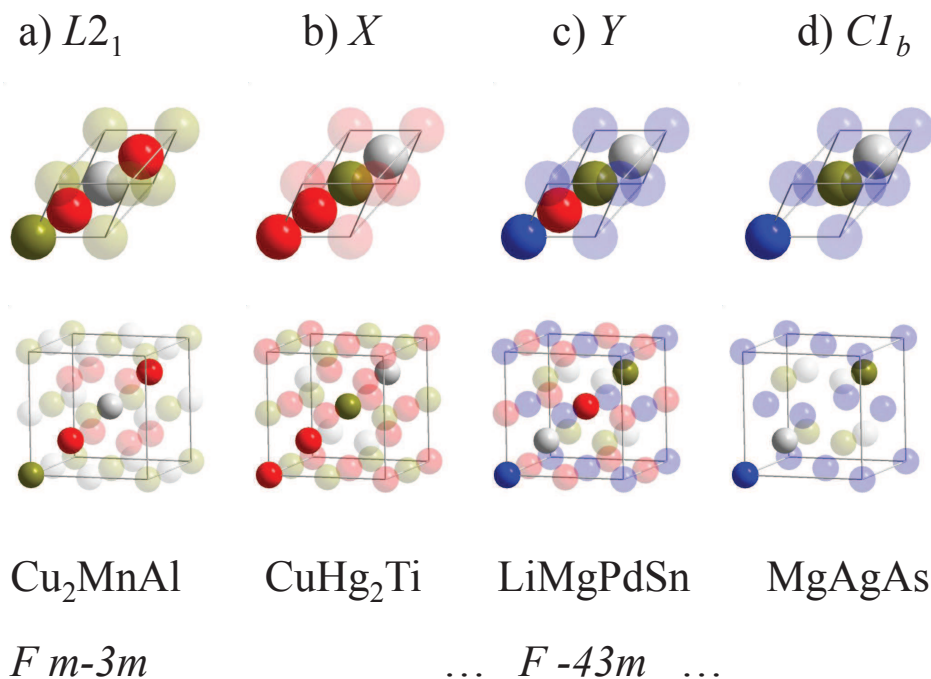

a) $L2_1$ b) X c) Y d) Cl_b

Cu$_2$MnAl   CuHg$_2$Ti   LiMgPdSn   MgAgAs

F m-3m   … *F -43m* …

Figure 7.5: Different crystal structures of well-ordered Heusler compounds. In Cu$_2$MnAl compound red, gray, and green colors are representative of Cu, Mn, and Al atoms respectively. In CuHg$_2$Ti compound red, gray, and green colors show Hg, Ti, and Cu respectively. In LiMgPdSn blue, red, green, and gray colors are representative of Sn, Mg, Pd, and Li atoms respectively. In MgAgAs blue, green, and gray colors show Mg, As, and Ag atoms respectively.

Figure 7.6 shows the powder diffraction data of the three compounds measured at room temperature. The diffraction data confirm the cubic LiPdMgSn crystal structures for all compounds. Note that the (111) and (200) *fcc-* superstructure reflexes are not resolved for all compounds due to nearly equal scattering amplitudes of the constituting elements, which are all found in the third period of the periodic table of elements. A discussion of disorder phenomena as known from related Heusler compounds is therefore not possible. A deeper insight into the structure is a task for the future and could be achieved employing methods such as anomalous XRD or extended x-ray absorption fine structure (EXAFS). Rietveld refinements of the data were performed using the TOPAS ACADEMIC software package [91]. The lattice parameters as deduced from

the refinements as well as the Rietveld figures of merit are shown in Table 7.4 and compared to the calculated, structural data. The calculated bulk moduli of the Ni compounds are in the order of 180-190 GPa whereas the Cu compound is obviously softer with a $\approx 30\%$ lower value.
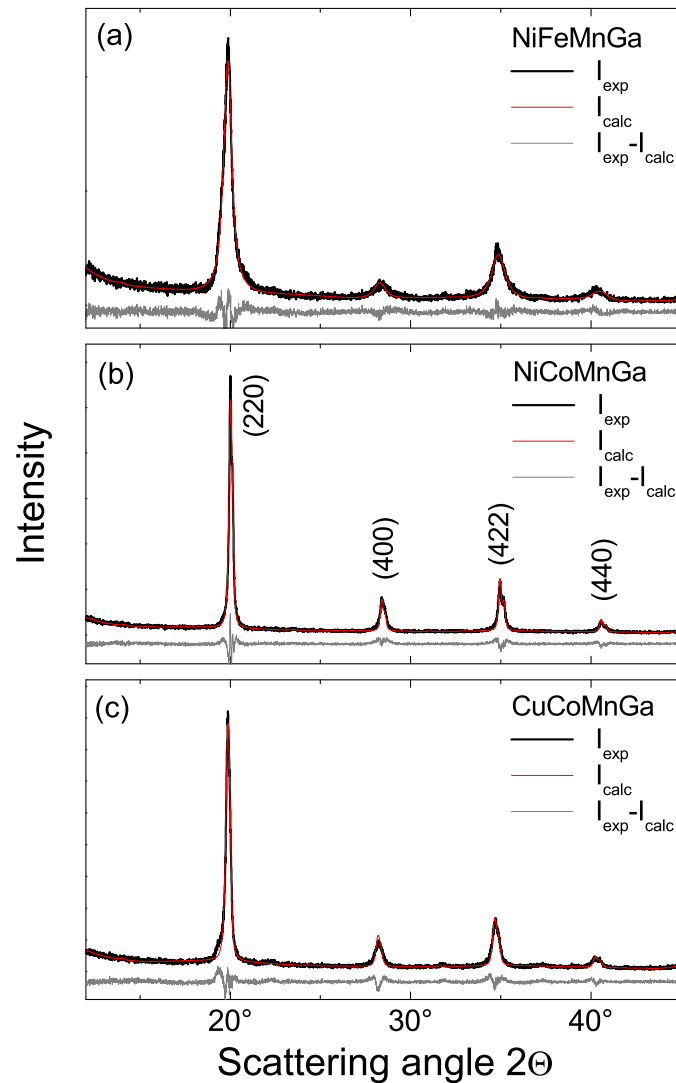

Figure 7.6: Powder XRD of polycrystalline NiFeMnGa (a), NiCoMnGa (b), and Cu-CoMnGa (c). The data were recorded at room temperature using Mo K_α radiation.

Table 7.4: Lattice parameters, Rietveld figures of merit and goodness of fit (GoF) of the NiFeMnGa, NiCoMnGa, and CuCoMnGa compounds.

Compound	$a_{\exp}$ [Å]	R_{wp}	R_{exp}	R_{Bragg}	GoF
NiFeMnGa	5.799	11.99%	8.27%	2.19%	1.45
NiCoMnGa	5.803	11.63%	8.10%	2.48%	1.44
CuCoMnGa	5.847	11.32%	8.63%	1.51%	1.31

7.1.5 Magnetic Properties

The magnetic properties of the polycrystalline samples were investigated by means of SQUID magnetometry. The field dependent magnetic moments at low temperature (5 K) are displayed in Figure 7.7. The inset shows temperature dependent measurements of the magnetizations. All compounds are soft-magnetic. The saturation magnetic moments of the compounds are summarized in Table 7.5. The calculated contribution of each atoms in total magnetic moment are summarized in Table 7.2.

According to the localized Slater-Pauling behavior (Equation 7.1) and the electronic structure calculations, the magnetic moment for NiFeMnGa should amount to 4 μ_B and for NiCoMnGa to 5 μ_B. The discrepancy between these and the experimental values is quite large. It may be attributed to structural disorder but the order of magnitude is too high to be dedicated only to this effect. Impurities below the detection limit of XRD (approximately 5%) may also contribute to the deviations. A ferrimagnetic arrangement or canted spins are possible but energetically unstable for all compounds according to the calculations. Antisite disorder may, however, lead to local ferrimagnetic order of the Mn atoms when they are nearest neighbors.

$$m = (N_V - 24)\,\mu_B \qquad (7.1)$$

Table 7.5: Magnetic moments of the NiFeMnGa, NiCoMnGa, and CuCoMnGa alloys at 5 K and 300 K and Curie temperatures T_C.

Compound	m_{exp}(5 K) [μ_B]	m_{exp}(300 K) [μ_B]	T_C [K]
NiFeMnGa	3.45	1.74	326
NiCoMnGa	4.47	4.28	646
CuCoMnGa	2.32	2.14	631

As it was discussed in Section 3.3, for high valence electron concentrations ($N_v \geq 30$), the assumption of localized behavior may no longer hold. Heusler compounds with mo-
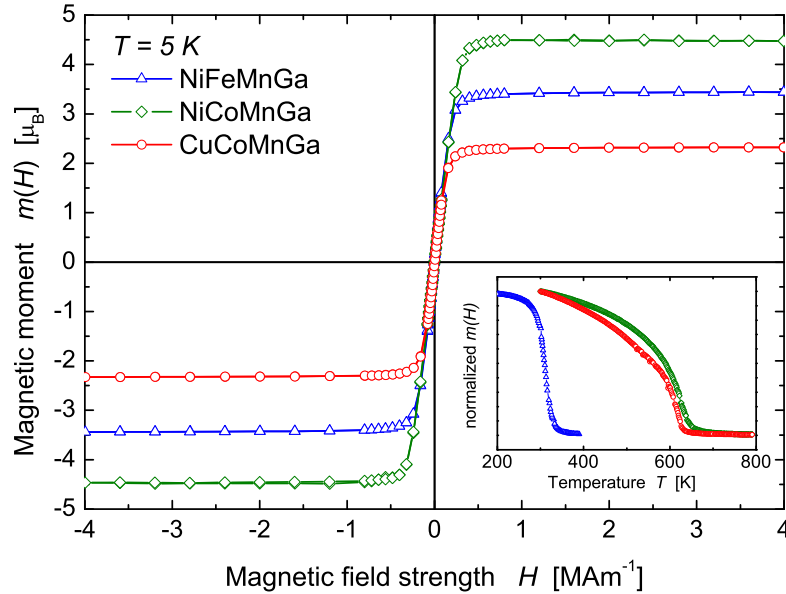
Figure 7.7: Magnetic properties of NiFeMnGa, NiCoMnGa, and CuCoMnGa. The MH-curves were measured at $T = 5$ K. The inset shows temperature dependent measurements of the magnetic moments in order to determine T_C.

ments much larger than 6 μ_B are rarely known. For higher valence electron concentrations, an itinerant Slater-Pauling behavior is approximated where the magnetic moment is determined by constraining the Fermi energy by the filled majority states [30, 31]. The following approximation is valid for these certain cases of Heusler compounds:

$$m_{\mathrm{it}} \approx (34 - N_v)\ \mu_B \tag{7.2}$$

This behavior is expected for d-elements with nearly filled d-shells as is the case for Ni (or Cu) and is obtained for various Ni_2-based Heusler compounds [92]. Here, the Cu-containing compound follows obviously this rule and the itinerant behavior may arise from the CuCo sublattice. Indeed, because of the localized moment at the Mn atoms, the behavior is not purely itinerant. The rule given by Equation (7.2) hints that approximately 17 majority states are occupied [30, 92] corresponding to T_d symmetry with a complete filling of one a_1, two e and four t_2 majority bands.

The magnetic moment of CuCoMnGa with $N_v = 30$ should amount to 6 μ_B when assuming half-metallicity and a localized Slater-Pauling behavior (Equation (7.1)), which is in disagreement with the calculational and the experimental results. However, for an itinerant Slater-Pauling behavior (Equation (7.2)) the expected moment is only 4 μ_B. The lower magnetic moment is explained by the vanishing contribution of Cu to the

magnetic properties due to the filled d shell, which makes a localized Slater-Pauling behavior in the form presented in Equation (7.1) impossible. Although the calculation did not result in a half-metallic ferromagnetic state, the experimental value is also still too small compared to the calculation for a simple, regular ferromagnet. The low magnetic moment may also be a result of disorder and/or undetected impurities below the limit of powder XRD. The occurrence of disorder may be explained by the structural instability suggested by the calculations. As for the other two compounds, antisite disorder may lead to local ferrimagnetic order of next-neighbor Mn atoms with the result of a lower total magnetic moment. This effect is not accounted for in the CPA calculations.

NiFeMnGa and NiCoMnGa, however, show at least fair agreement with the Slater-Pauling rule and thus half-metallic ferromagnetic behavior, which makes the compounds attractive for the research area of spintronics. The high T_C of NiCoMnGa makes the compound even more attractive for application. Optimizing annealing temperatures and times could provide help to obtain a better quality of the samples with respect to disorder and impurities. While NiCoMnGa and CuCoMnGa show a textbook ferromagnetic behavior, NiFeMnGa exhibits a rather sharp drop of magnetization at its Curie temperature. This may be due to a structural transformation and remains to be analyzed in future experiments (high-temperature XRD).

7.1.6 Summary

In conclusion, quaternary Heusler compounds were identified using a theoretical approach for preselection. As predicted by these calculations we have found the half-metallic ferromagnets NiFeMnGa and NiCoMnGa. These are the first reported Ni-based half-metallic ferromagnets within the huge family of Heusler compounds. CuCoMnGa turned out to be a regular metallic ferromagnet due to the closed shell character of the Cu d electrons. NiFeMnGa has a Curie temperature that is too low to make it relevant for technological applications but NiCoMnGa with a high spin polarization, high magnetic moment, and high Curie temperature is an interesting new material for spintronics applications. A large resource of quaternary Heusler materials is open and to be investigated in future to find prospective materials for several applications.

7.2 Electronic, Structural, and Magnetic Properties of the Half-Metallic Ferromagnetic Quaternary Heusler Compounds CoFeMnZ (Z = Al, Ga, Si, Ge)

7.2.1 Introduction

The class of quaternary Heusler materials offers an enormous variety of possibilities for rational material design since Heusler compounds are known to exhibit tunable magnetic and electronic properties depending on their valence-electron count. Some quaternary Heusler compounds have recently been proposed to exhibit half-metallic ferromagnetism [93]. A comprehensive study of four yet unreported quaternary half-metallic ferromagnetic Heusler compounds will be presented in the following. The compounds were identified by *ab-initio* electronic structure calculations. The preferred route to predict a new quaternary half-metal has been to combine two ternary half-metals that are already known to crystallize in the Heusler structure, such as Co_2FeSi or Co_2MnSi [94]. Following this route, the quaternary compound CoFeMnSi was identified to be a half-metallic ferromagnet [95]. The present work reports on the theoretical identification and the experimental characterization of the quaternary Heusler half-metallic ferromagnets CoFeMnZ (Z = Al, Ga, Si, Ge).

Several quaternary—or, better, pseudo-ternary—Heusler compounds have been designed in order to tailor the middle of the gap exactly to the Fermi energy, as in $Co_2Mn_{1-x}Fe_xSi$ [96]. Quaternary Heusler compounds with a 1:1:1:1 stoichiometry, however, have as yet been little explored. For symmetry reasons (T_d), they are substantially different from the $L2_1$ pseudo-ternary Heusler compounds with O_h symmetry and $2 : [(1-x) : x] : 1$ or $2 : 1 : [(1-y) : y]$ stoichiometry. In applications, the quaternary CoFeMnZ compounds will have advantages over the pseudo-ternary $Co_2Fe_{1-x}Mn_xZ$ alloys. In the latter case, *i.e.*, the alloy type, random distribution of Fe and Mn leads to additional disorder scattering resistivity and thus to an increase in the total resistivity. The result is that electronic devices based on *"real"* quaternary Heusler compounds are expected to have lower power dissipations.

The experimental results presented in the following include a structural analysis by powder X-ray diffraction (XRD), a characterization of the magnetic properties by a superconducting quantum intereference device (SQUID), and an investigation of the band structures by hard X-ray photoemission spectroscopy (HAXPES).

7.2.2 Structural properties

The classical intermetallic Heusler compounds consist of two transition or rare-earth elements and one main group element in the stoichiometric composition X_2YZ, and crystallize in the cubic $L2_1$ structure (space group no. 225: $F\,m\bar{3}m$). When one

Table 7.6: Different site occupations for the Y-type structure. M denotes a main-group element. Note that the exchange of the atoms between $4a$ and $4b$ or $4c$ and $4d$ positions and between the groups $(4a, 4b) \leftrightarrow (4c, 4d)$ does not change the structure because of the symmetry implied by the $F\,\overline{4}3m$ space group. In $L2_1$, the positions $(4c, 4d)$ become equivalent and combine to $8c$.

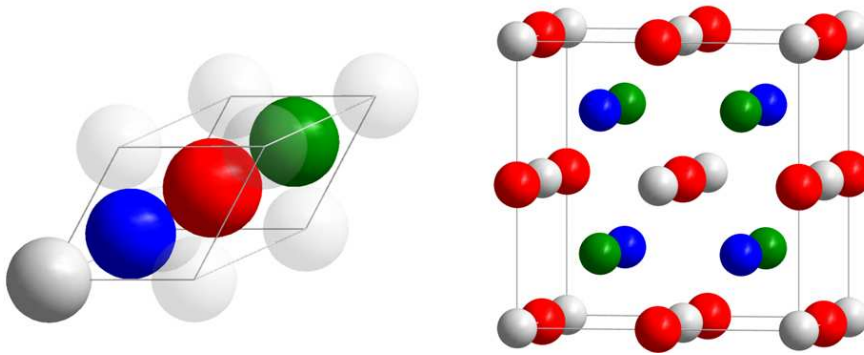|	$4a$ (0,0,0)	$4c$ (1/4,1/4,1/4)	$4b$ (1/2,1/2,1/2)	$4d$ (3/4,3/4,3/4)
Y Type I	M	Fe	Mn	Co
Y Type II	M	Mn	Fe	Co
Y Type III	Fe	M	Mn	Co

Figure 7.8: Crystal structure of the quaternary Y-type Heusler compound CoFeMnSi and related primitive cell. There are three nonequivalent supercells of CoFeMnSi in the Y-type structure depending on the occupation of the four different lattice sites $4a$ (0,0,0), $4b$ (1/2,1/2,1/2), $4c$ (1/4,1/4,1/4), and $4d$ (3/4, 3/4, 3/4). As deduced from ternary Heusler compounds, Co and Fe should occupy the lattice sites $4c$ and $4d$, and Mn and Si should occupy $4b$ and $4a$. Si atoms are gray, Mn atoms are red, Fe atoms are green, and Co atoms are blue. The ratios of atomic radii correspond to the factual values of the atoms.

of the two X atoms is substituted by a different transition metal X', a quaternary compound with the composition XX'YZ and $F\bar{4}3m$ symmetry (space group no. 216) is generated. The prototype of this Y-type structure of quaternary Heusler compounds is LiMgPdSn [46, 47]. Three possible nonequivalent superstructures based on the different positions of the four atoms exist for this structure type [48] (see Table 7.6). As shown in Figure 7.8 the LiMgPdSn-type structure exhibits a primitive fcc cell with a basis containing four atoms on the Wyckoff positions $4a$ to $4d$, which form a larger cubic cell. The three nonequivalent primitive or cubic cells are explained in Table 7.6 for the example of CoFeMnSi, as depicted in Figure 7.8. It is known from the corresponding regular Heusler compounds Co_2MnZ or also archetype Cu_2MnAl [27] that the Mn atoms and the main group elements are typically located on the octahedrally coordinated a and b Wyckoff positions, identical to the situation in Type I in Table 7.6. This configuration determines highly localized magnetic moments at the Mn atoms, which dictate the magnetic order in Heusler compounds [97].
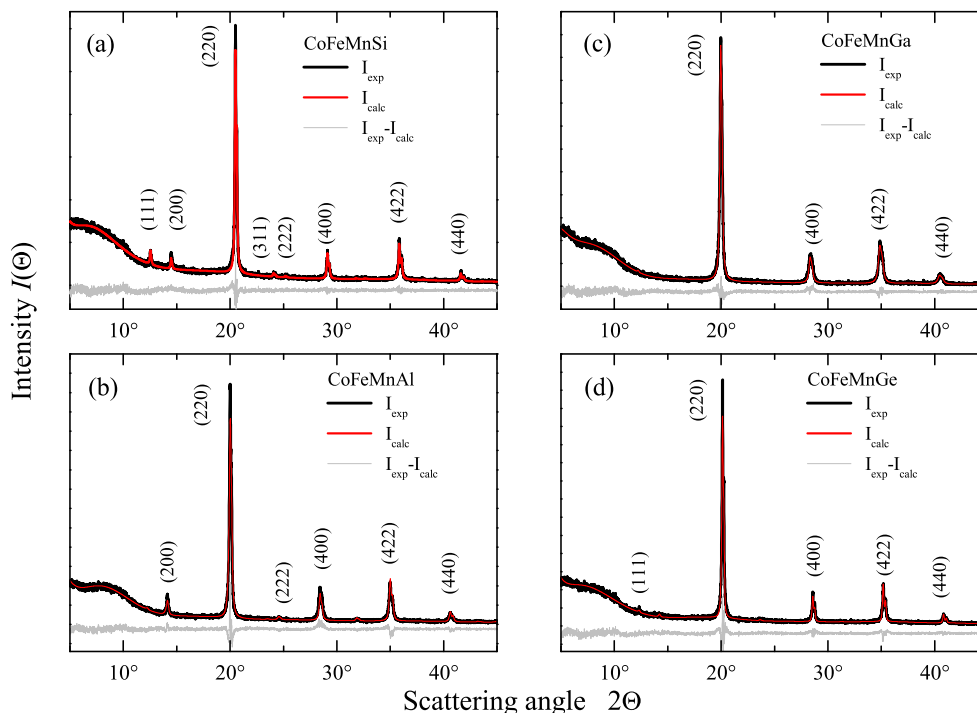

Figure 7.9: Powder XRD and Rietveld refinements of CoFeMnZ (Z = Si (a), Al (b), Ga (c), and Ge (d)). The measurements were carried out at room temperature using Mo K_α radiation.

The XRD patterns of the compounds, measured at room temperature, are shown in

Figure 7.9. Rietveld refinements of the data were performed using the TOPAS ACA-DEMIC software package [91]. Details of the refinements are shown in Table 7.7. In the patterns of CoFeMnGa and CoFeMnGe, the (111) and (200) fcc superstructure reflexes are very small or completely absent. This is the result of the nearly equal scattering amplitudes of all constituent elements ($3d$ and $4p$); this impedes a detailed order-disorder analysis by Mo K$_\alpha$ XRD. It is impossible to distinguish among Type I, II, or III (see Table 7.6) for all compounds because only $3d$ elements are involved. For the Rietveld refinements, Type I was assumed, based on the experiences from regular X$_2$YZ Heusler compounds and the results of the *ab-initio* electronic structure calculations (see Section 7.2.3). However, an analysis of order was possible for the Al and Si atoms. In the pattern of CoFeMnAl the (200) reflex is clearly visible, but (111) is not visible at all. This indicates disorder among the Mn and Al atoms when Type I is assumed. Including this type of structural disorder in the refinement provided an improved weighted-profile R-factor R_{wp} of 10.90% as compared to 12.62% for an assumed ordered Y-type structure. It has been known for several years that Al-containing Heusler compounds are very susceptible to this type of disorder [98]. Similarly, but to a smaller extent of disorder ($\approx$ 15% among Mn and Si), the Rietveld refinement of CoFeMnSi was improved (R_{wp} =8.38%, Y-type: 8.50%).

Table 7.7: Lattice parameters and weighted-profile R-factors R_{wp} of CoFeMnZ compounds. The lattice parameters a_{exp} and a_{calc} are given in Å. a_{calc} is taken from a structural optimization (see Section 7.2.3). The R-factors R_{wp} of CoFeMnAl and CoFeMnSi were determined employing disordered structural models, as described in the text.

Z	a_{exp} [Å]	a_{calc} [Å]	R_{wp} [%]
Al	5.7858	5.6916	10.90
Si	5.6545	5.6103	8.38
Ga	5.8107	5.7075	10.52
Ge	5.7629	5.7099	10.70

7.2.3 Electronic structure calculations

Ab-initio electronic structure calculations were performed using Wien2k [76, 77, 78] and the generalized gradient approximation (GGA) [79]. The number of plane-waves was restricted by $R_{MT}k_{max} = 9$. All self-consistent calculations were performed with 256 k-points in the irreducible wedge of the Brillouin zone, based on a mesh of 20^3 k-points. The density of states was calculated on a mesh of 25^3 k-points. The conver-

gence criteria were set to 10^{-5} Ry for energy and simultaneously to 10^{-3} e$^-$ for charges. It was checked that the energies were converged with respect to the number of k-points and the number of plane-waves. Further details are given in [35, 93]. The lattice parameters were optimized as a starting point for the calculation of the band structures, densities of states, and magnetic moments. The magnetic state was checked by use of different settings of the initial magnetization: ferromagnetic (all initial spins parallel) or ferrimagnetic (initial spins partially anti-parallel). The results of the structural optimization are summarized in Table 7.8. In the case of the Type III atomic arrangements two different magnetic ground states were found. The additional results (marked by "*") exhibit higher energies compared to the other magnetic and site configurations. For the Type I and II atomic arrangements, only one magnetic ground-state was found, independent of the initial settings of the magnetization.

Table 7.8: Results of the structure optimization. The structure types are explained in Table 7.6. For the "*"-types different settings of the initial magnetization were used.

	E_{tot} [Ry]	a_{opt} [Å]	m_{tot} [μ_B]	m_{Co} [μ_B]	m_{Fe} [μ_B]	m_{Mn} [μ_B]
CoFeMnAl						
Type I	-8135.60220	5.692	3.00	0.81	-0.13	2.44
Type II	-8135.57782	5.775	5.03	1.20	2.22	1.76
Type III	-8135.56980	5.793	6.41	1.80	2.11	2.66
Type III*	-8135.54059	5.772	0.68	1.21	2.03	-2.46
CoFeMnSi						
Type I	-8230.06630	5.611	4.00	0.89	0.52	2.70
Type II	-8230.04494	5.613	3.98	0.95	2.52	0.58
Type III	-8230.01337	5.649	5.33	1.81	1.66	1.98
Type III*	-8230.00433	5.588	0.45	0.47	1.58	-1.51
CoFeMnGa						
Type I	-11538.16710	5.717	3.05	0.77	-0.25	2.60
Type II	-11538.15619	5.792	5.98	1.26	2.45	2.42
Type III	-11538.14772	5.832	6.84	1.79	2.28	2.87
Type III*	-11538.12254	5.810	0.35	1.22	2.11	-2.88
CoFeMnGe						
Type I	-11848.12662	5.713	4.01	0.86	0.51	2.71
Type II	-11848.10152	5.726	4.25	0.99	2.54	0.81
Type III	-11848.07647	5.780	6.03	1.75	1.94	2.45
Type III*	-11848.06634	5.756	0.18	-0.48	-1.81	2.39

All structural optimizations showed that the Type I structures with Co($4d$)Fe($4c$)-Mn($4b$)Z($4a$) exhibit the lowest energy, as reported in detail for CoFeMnSi [95] (the

small differences in the results are caused by the larger number of plane-waves used in the present work). The total energy of the Type I structure is on average ≈ 270 meV lower than that of the Type II structure. The optimized lattice parameters are compared with the experimental values in Table 7.7. GGA usually tends to slightly larger lattice parameters. It is obvious that all calculated values are $\approx 1\%$ below the experimental values. This may be attributed to a temperature effect (measurement at 300 K), to disorder, and/or other structural defects. In the following, Type I structures with optimized lattice parameters were used for the calculations of the electronic structures and magnetic properties of the compounds.

The stability of the cubic structure was checked by calculation of the elastic constants c_{ij}. The elastic constants were calculated by applying isotropic strain as well as volume-conserving tetragonal and rhombohedral strains to the optimized cubic primitive cell. There are only three independent components for cubic symmetry: $c_{11} = c_{22} = c_{33}$, $c_{12} = c_{13} = c_{23}$, and $c_{44} = c_{55} = c_{66}$. The bulk modulus of cubic systems is derived from $B = (c_{11} + 2c_{12})/3$. The elastic stability criteria of the cubic structure are found from the elastic constants [83]. For stability of the cubic structure, the bulk modulus, the c_{44} shear modulus, and the tetragonal shear modulus must be positive, resulting in the following conditions: $c_{11} + 2c_{12} > 0$, $c_{44} > 0$, and $c_{11} - c_{12} > 0$.

The elastic anisotropy $A_e = 2c_{44}/(c_{11} - c_{12})$ compares the shear moduli and allows a decision about the structural stability. Young's modulus becomes isotropic for $A_e = 1$. Materials with large A_e ratios show a tendency to deviate from the cubic structure. The results of the calculated elastic properties are summarized in Table 7.9. The results are for the Birch–Murnaghan equation of state (EOS). They are within $\approx \pm 0.4$ GPa compared to EOS2 [99] or Murnaghan, and no differences in the optimized lattice parameters are observed within 10^{-4} Å for different EOSs. All fits to determine the optimized lattice parameters were performed with nine volume changes between -8% and +8% approximately around the relaxed volume. For elastic properties, seven deformations within $\pm 4\%$ about the equilibrium structure were used.

Table 7.9: Elastic constants of CoFeMnZ compounds (Z = Al, Si, Ga, Ge). A_e is dimensionless.

Z	c_{11} [GPa]	c_{12} [GPa]	c_{44} [GPa]	B [GPa]	A_e
Al	209	183	156	192	12.1
Si	302	197	177	232	6.3
Ga	245	198	147	214	3.4
Ge	315	190	132	231	2.1

CoFeMnAl exhibits the lowest bulk modulus, and the highest values are observed

for CoFeMnSi and CoFeMnGe. With respect to both A_e and the elastic stability criteria, the compounds are stable in the cubic Y-type crystal structure. The observed structural instability of CoFeMnAl, with a tendency to disorder [100], may be related to the comparatively high elastic anisotropy. The Cauchy pressure ($p_C = c_{12} - c_{44}$) is positive for all four compounds.

Figures 7.10–7.13 show the calculated electronic structures of the CoFeMnZ (Z = Al, Si, Ga, Ge) compounds. The compounds exhibit electronic structures typical of fully spin-polarized half-metallic ferromagnetic Heusler compounds with a band gap in the minority channel.
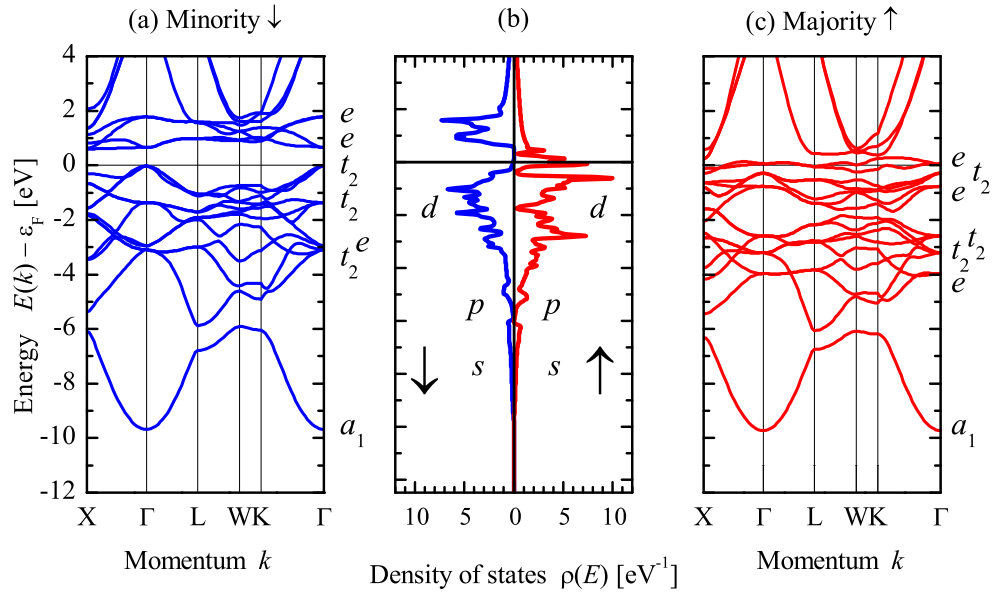
Figure 7.10: Band structure and density of states of CoFeMnAl. (a) minority bands, (b) density of states, (c) majority bands. Majority and minority spin densities are denoted by ↑ and ↓, respectively. The irreducible representations of the bands are given for the Γ point.

All compounds exhibit a typical Heusler-compound hybridization gap between the low-lying s bands and the remaining, high-lying part of the valence bands, which mainly contain p and d states. The sizes of the sp gap of the compounds differ but do not depend much on the spin character of the bands because of the small exchange splitting of the s states. The hybridization gaps between W and L are indirect, and their sizes are 40 meV, 1 eV, 1.7 eV, and 2.6 eV for Z = Al, Ga, Si, and Ge, respectively. The widths of the low-lying s-bands are 3.5 eV, 2.5 eV, 3 eV, and 2.5 eV for Al, Si, Ga, and Ge, respectively. This is related to the different lattice parameters and thus to the
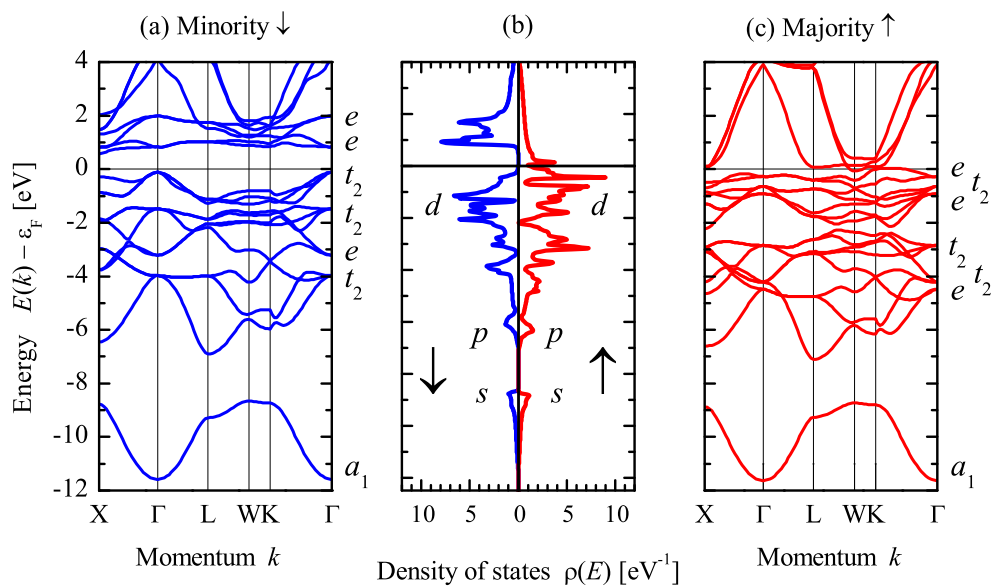
Figure 7.11: Same as Figure 7.10 but for CoFeMnSi.
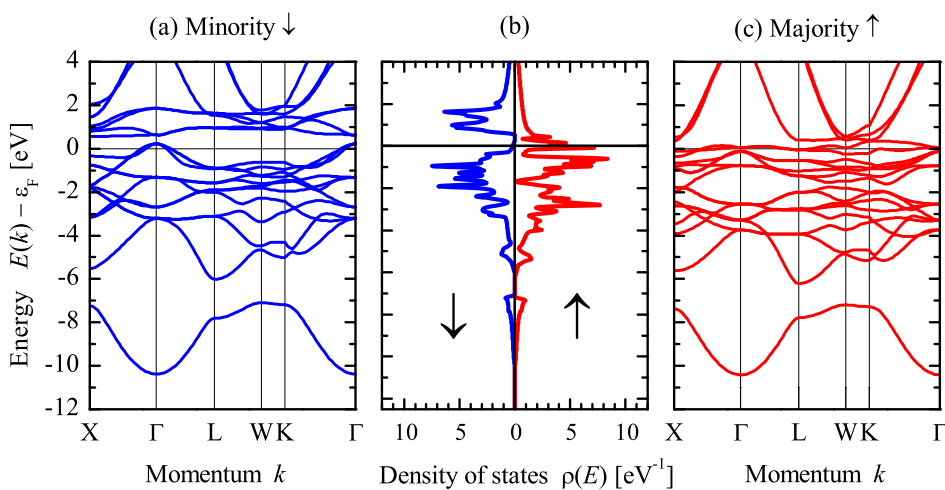
Figure 7.12: Same as Figure 7.10 but for CoFeMnGa.
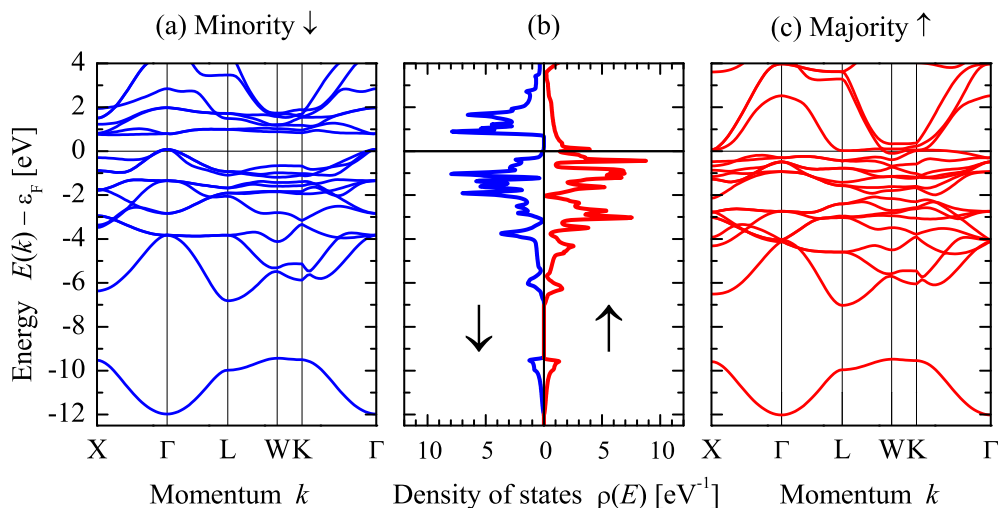
Figure 7.13: Same as Figure 7.10 but for CoFeMnGe.

differences in the overlaps of the wave functions. The small sp gap in CoFeMnAl points to weak hybridization and indicates structural instability; this may be the reason for anti-site disorder.

The most important feature of the electronic structure is the band gap in the minority channel, turning the compounds to half-metallic ferromagnets. This band gap in the minority states arises from a particular band filling by 12 valence electrons. This is caused by successive filling of the minority bands a_1 by one s electron, t_2 by three p electrons, e and t_2 by a total of five d electrons, followed by subsequent complete filling of an additional t_2 band by three d electrons (see the assignment of the irreducible representations of the bands at Γ in Figures 7.10 and 7.11 for the example of the compounds based on Al and Si, respectively). It should be noted that the representations for the T_d group used here for the quaternary compounds with a 1:1:1:1 composition are considerably different from quaternary (pseudo- ternary) or ternary Heusler compounds with O_h symmetry and a 2:1:1 composition described in [101]. At 24 valence electrons, a quasi-closed shell character is reached, accounting for both spin channels with 12 minority and 12 majority electrons. Additional valence electrons (here three for Al, Ga, or four for Si, Ge) fill majority bands only, and the exchange interaction concurrently splits the minority and majority bands. According to the Slater–Pauling rule [32, 33], ϵ_F is pinned directly above the occupied minority states. In the minority channel of CoFeMnGa, 0.02 electrons are found above ϵ_F at the optimized lattice parameter, calculated for $T = 0$ K. A slight change in the lattice parameter will push

this band at the Γ point away from ϵ_F. It is interesting to note that these states will be depleted at elevated temperatures as a result of the Fermi–Dirac distribution; this increases the spin polarization with temperature.

7.2.4 Magnetic Properties

The magnetic properties of the polycrystalline samples were investigated using a SQUID magnetometer. The field-dependent magnetization at 5 K is shown in Figure 7.14. The corresponding magnetic moments in saturation are given in Table 7.10. Although the magnetic moment of CoFeMnSi is in reasonable accordance with the Slater–Pauling rule [6, 30, 31], the other compounds exhibit higher magnetic moments than expected. These results indicate the existence of disorder and/or magnetic impurities. As is known from the structural characterizations, disorder was identified in CoFeMnAl and CoFeMnSi, and cannot be excluded for CoFeMnGa and CoFeMnGe. Magnetic impurities were not identified in either of the diffraction patterns but may be below the detection limit of XRD, *i.e.*, an impurity content of $\approx 5\%$. EDX shows no phase separation on a length scale of 1 μm [102]. The Curie temperatures T_C of the compounds were determined by temperature-dependent magnetization measurements as shown in the inset of Figure 7.14 and Table 7.10. Evidently, all compounds exhibit high T_C facilitating technological application.
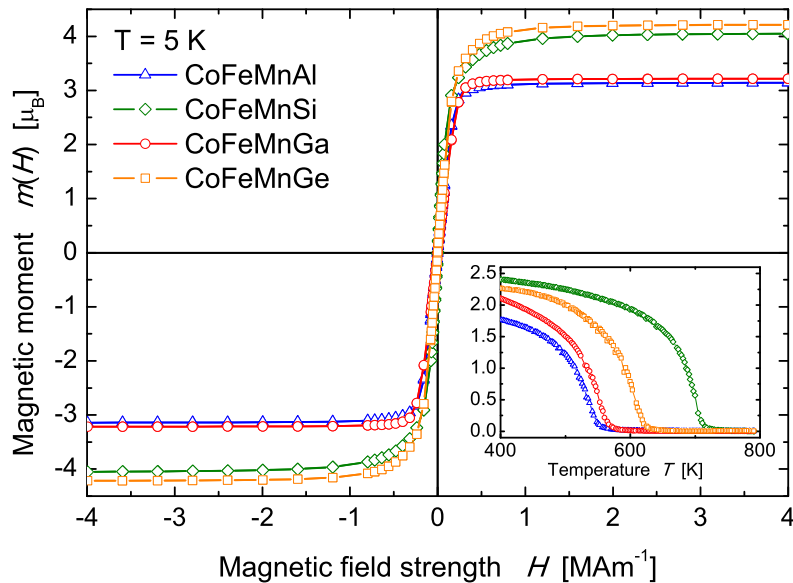
Figure 7.14: Magnetic properties of CoFeMnZ (Z = Al, Si, Ga, and Ge). The field-dependent measurements were performed at $T = 5$ K. The inset shows temperature-dependent magnetic moments in the high-temperature range of the Curie temperature.

The calculated values m_{calc} of the total magnetic moments are all integers, as is typical for half-metallic ferromagnets with a band gap in the minority states at ϵ_F. According to the Slater–Pauling rule, the magnetic moments adopt values of 3 μ_B for Z = Al and Ga, and 4 μ_B for Z = Si and Ge. From the calculations of the site-specific moments, it is evident that the magnetic properties are mainly determined by the Mn atoms, which contribute the highest magnetic moments, of approximately 2.5 μ_B. The magnetic moment at the Co sites is also stable against variations of the Z element and the number of valence electrons. It exhibits a value of approximately 0.8 μ_B. Most interestingly, the moment at the Fe site shows the strongest variation and even exhibits a change of sign when comparing compounds with 27 and 28 valence electrons. In CoFeMnAl and CoFeMnGa, it is oriented anti-parallel to the Mn and Co atoms. This may be interpreted as a ferrimagnetic order. The nearest neighbors of Mn are Co and Fe atoms. It can therefore be supposed that the magnetic moments at the Fe atoms are induced by the neighboring Mn spins. In other words, the stability of the Co and Mn moments, together with the Slater–Pauling rule, dictates whether the moment at the Fe sites is aligned anti-parallel or parallel to Mn. This obvious dependence of the Fe moments also explains the soft-magnetic behavior of the compounds, even for seemingly ferrimagnetic types of order. A detailed investigation of the local magnetic moments of these compounds has recently been carried out using X-ray magnetic circular dichroism and supports the findings shown here [102].

The measured magnetic moments at 5 K are increased by 0.1 μ_B for the Al and Si compounds, and by 0.2 μ_B for the Ga and Ge compounds, compared to the calculated values. Evidently, the magnetic order is conserved at room temperature, and the temperature dependences of the magnetic moments for all compounds are very similar.

Table 7.10: Magnetic moments and T_C of CoFeMnZ compounds.

Z	m_{exp}(5 K) [μ_B]	m_{exp}(300 K) [μ_B]	m_{calc} [μ_B]	T_C [K]
Al	3.14	2.65	3.0	553
Si	4.05	3.70	4.0	711
Ga	3.21	2.78	3.0	567
Ge	4.21	3.81	4.0	623

7.2.5 Hard X-ray Photoelectron Spectroscopy.

The compounds with Z = Si and Ge were investigated using photoelectron spectroscopy. The measurements were carried out at different excitation energies in order to investigate the influence of varying cross sections.

7.2.5.1 Core Level Spectroscopy

Figure 7.15 shows the HAXPES spectra of CoFeMnSi and CoFeMnGe in the energy range of the semi-core level (note the low intensity of the valence band at energies from -12 eV to 0 compared to the intense Ge $3s$ or Si $2s$ lines). The spin–orbit splitting of the $3p$ states is resolved clearly for Ge, but not for the transition metals (Co, Fe, Mn), despite the small differences in nuclear charges.
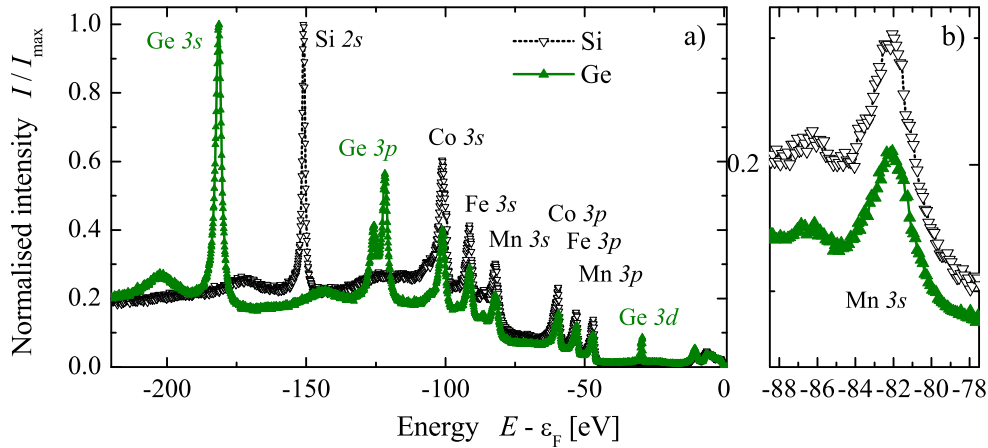

Figure 7.15: Spectra of the shallow core states of CoFeMnZ (Z = Si, Ge). The excitation energy was $h\nu = 7.9380$ keV. The spectra are normalized to the maxima for easier comparison; (b) shows an enlarged view of the Mn $3s$ states.

Besides the spin-orbit splitting of the p states, the spectra shown in Figure 7.15 exhibit several satellites, which have different origins. The appearance of metallic satellites (for example, plasmons) or multiplet splittings resulting from exchange interaction is typical. The spin–orbit (Δ_{SO}) and exchange (Δ_{EXC}) splittings were determined for selected core and semi-core levels. Selected results for Δ_{SO} are summarized in Table 7.11. The most interesting finding is that the Mn $3s$ states of the compounds exhibit well-distinguished exchange splittings of $\Delta_{EXC}^{\text{Si}} = 4.3$ eV and $\Delta_{EXC}^{\text{Ge}} = 4.6$ eV (see Figure 7.15(b)); these splittings are quite independent of the main-group element or the total magnetic moment. The intensity ratio between the main $3s$ line and the exchange-split satellite appears to be independent of the photon energy; it amounts to 1.37 ± 0.01. The Coulomb interaction of the Mn $3s$ core hole and the Mn $3d$ valence electrons leads to a splitting of the photoionized state into sublevels [101, 103] caused by the existence of more than one possible final ionic state during ejection of electrons, even from a closed s shell. A difference in the splitting would point to differences in the localization of the Mn $3d$ valence electrons in CoFeMnSi and CoFeMnGe. The

observed similarity of the compounds shows that the Mn atoms behave identically and independently of the main-group element, even though the compounds differ in their total magnetic moments.

Figure 7.16 displays the results of the core-level photoemissions from the transition-metal $2p$ states of CoFeMnSi and CoFeMnGe excited by hard X-rays of energy approximately 6 keV. The typical spin–orbit splitting of the states into $2p_{1/2}$ and $2p_{3/2}$ sublevels is clearly detected ($2p_{1/2}$ in -793.21 eV, -719.61 eV, -649.94 eV and $2p_{3/2}$ in -778.21 eV, -706.71 eV and -638.44 eV for Co, Fe and Mn, respectively).
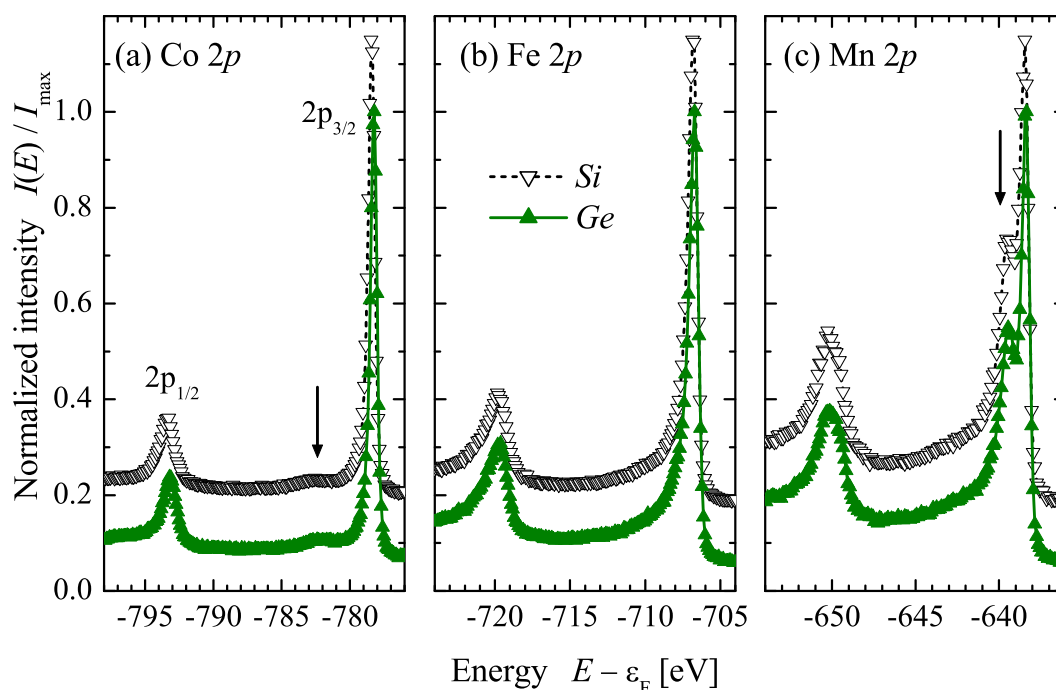
Figure 7.16: Co, Fe, and Mn $2p$ core levels of CoFeMnZ (Z = Si, Ge). The most important satellites (see text) are marked by arrows. The photon energy was $h\nu = 5.9534$ keV.

The details of the spin orbit splitting of the transition metal $2p$ core levels are summarized in Table 7.11 together with selected intensity ratios. The intensity ratio $R(2p_{3/2}) = I_{Co}/I_{Fe}/I_{Mn}$ of the $2p_{3/2}$ core states is independent of the compound and points on the correct stoichiometry of the samples. The statistical branching ratio $BR = I(2p_{3/2})/I(2p_{1/2})$ is expected to be 4:2 from the $(2j+1)$ multiplicity of the states. In nearly all cases, the observed branching ratios are larger than the statistical value of 2. At the higher photon energy of approximately 8 keV, they are lower than those measured at the excitation energy of approximately 6 keV. This is because of the energy dependence of the differential cross sections σ_{nlj} and angular asymmetry parameters

β_{nlj} [104]. For the present experimental setup and linearly p-polarized photons, the energy dependence of the branching ratio for the $2p$ states is given by:

$$BR(E) = \frac{\sigma_{2p_{3/2}}(E)(1 + \beta_{2p_{3/2}}(E))}{\sigma_{2p_{1/2}}(E)(1 + \beta_{2p_{1/2}}(E))}. \tag{7.3}$$

This ratio only accounts for the spin–orbit-split components and does not include multiplet effects. The changes in the branching ratios with excitation energy, however, reflect the energy dependence of both the differential cross-section and the angular asymmetry parameter.

The observed spin–orbit splitting itself is independent of the excitation energy, as expected. The calculated spin–orbit splittings are 14.8 eV, 12.5 eV, and 10.4 eV for Co, Fe, and Mn, respectively. These values are within 10 meV, independent of the main-group element in the CoFeMnZ compounds. The observed and calculated values for Co and Fe are in good agreement within the resolution of the experiment. A considerable deviation is found for the Mn $2p$ states (≈ 1.5 eV). The reason is the observed multiplet splitting (see below), which was not accounted for in the calculations. The interaction between the core hole and the valence electrons in the photoexcited state causes an additional increase in the splitting on top of the ground-state spin–orbit interaction.

Table 7.11: Experimentally determined spin-orbit splitting Δ_{SO} and intensity ratios in the core-level spectra of CoFeMnSi and CoFeMnGe. $R(2p_{3/2}) = I_{Co}/I_{Fe}/I_{Mn}$ is the intensity ratio of the $2p_{3/2}$ core states. BR is the branching ratio of the $2p$ states. All core level energies are given in eV. The exact excitation energies $h\nu = 5.9534$ keV and 7.9380 keV are assigned by 6 and 8, respectively.

Z	$h\nu$	Co $2p$		Mn $2p$		Fe $2p$		
		Δ_{SO}	BR	Δ_{SO}	BR	Δ_{SO}	BR	$R(2p_{3/2})$
Si	6	14.90	2.30	11.96	3.07	13.00	3.15	0.70 : 0.76 : 0.75
	8		1.83		2.91		2.76	
Ge	6	15.00	2.42	11.80	3.49	13.00	3.29	0.71 : 0.77 : 0.75
	8		2.03		3.25		3.01	

A pronounced, further splitting of the Fe $2p$ states is not observed. The absence of multiplet effects in the Fe $2p$ states points to the *"weak"* role of the Fe atoms in the magnetic properties of the compounds, as discussed above. In both compounds, the Co $2p_{3/2}$ state exhibits a broad satellite at approximately 4 eV below the maximum (marked by an arrow in Figure 7.16(a)). This satellite is also seen in the Co $2p_{1/2}$ state. The Co $2p$ satellite may be the result of an intra-atomic shake-up transition from states directly below ϵ_F into the onset of the unoccupied s-bands at approximately 4–5 eV

above ϵ_F. An influence of the interaction between the core hole with the partially filled d-bands cannot, however, be excluded. A similar transition is also observed in X-ray absorption spectroscopy and is assigned to effects of the fcc structure [102, 105].

The Mn $2p_{3/2}$ state exhibits a typical multiplet structure with a pronounced splitting of approximately 1 eV (see the arrow in Figure 7.16(c)). This splitting is not seen in the Mn $2p_{1/2}$ state but leads only to a considerable broadening of the line. Additional weaker satellites show up as broadenings at approximately 4 eV and 7 eV below the Mn $2p_{3/2}$ and $2p_{1/2}$ states, respectively. The multiplet splitting of the Mn $2p$ states arises from the interaction of the core hole with the partially filled d-bands, which are strongly localized [106, 107]. Similar to the splitting of the Mn $3s$ state, the Coulomb interactions of the Mn $2p$ core holes and the Mn $3d$ valence electrons lead to splitting caused by the existence of several possible final ionic states [101, 103]. The splittings and intensity ratios observed in the spectra of the Mn states of CoFeMnGe or CoFeMnSi are very close to those of Co_2MnGe. In Ref. [101], the multiplet splittings of the Mn $3s$ and $2p$ states were analyzed in detail and it was shown, by comparing experimental data with calculations, that the Mn state cannot be identified as being definitely ionic Mn^{3+} or Mn^{2+}, but is in between. This means that one has either a mixture of d^4 and d^5 or, more realistically for a metallic solid, a formal $d^{4.x}$ configuration with respect to the incomplete localization of the d electrons at the Mn site.

7.2.5.2 Valence band spectroscopy

Figure 7.17 compares the valence-band spectra of CoFeMnSi and CoFeMnGe excited by hard X-rays of photon energy of approximately 8 keV. Both compounds exhibit the hybridization gap expected from the electronic structure calculations at approximately 8 eV below ϵ_F. The low-lying s states with a_1 character at Γ exhibit maxima at -9.9 eV and -10.5 eV for CoFeMnSi and CoFeMnGe, respectively. The energies of the maxima correspond to the centre of the low-lying a_1 bands rather than to the maxima in the calculated densities of states at -8.9 eV and -9.6 eV (see Figures 7.11 and 7.13). As a result of the different cross-sections for the Si $3s$ and Ge $4s$ states at the same photon or kinetic energy, the intensity is considerably lower in CoFeMnSi than in CoFeMnGe. At the same time, the maxima at approximately -6 eV are lower in CoFeMnGe than in CoFeMnSi.

The energy range of the d bands in CoFeMnSi contains three major maxima at approximately -1.55 eV, -2.95 eV, and -4.4 eV. A comparison with the calculated densities of states reveals that they arise from localized d states, either at Fe or Mn, which are responsible for the localized magnetic moments in Heusler compounds. The Co d states appear to be rather delocalized. Only two major maxima related to d states are resolved for CoFeMnGe at -1.3 eV and -4.1 eV. The maximum at -4.1 eV arises mainly
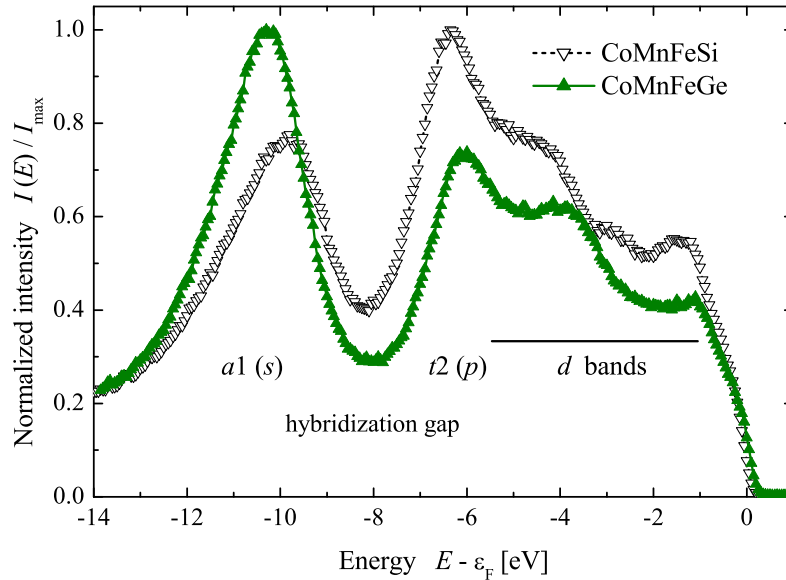
Figure 7.17: HAXPES valence band spectra of CoFeMnSi and CoFeMnGe. The excitation energy was set to $h\nu = 7.9380$ keV. For easier comparison the spectra are normalized to their maxima.

from t_2 majority states localized at the Mn atoms. The states at about -1.55 eV or -1.3 eV are in both compounds localized to a greater extent at Fe than at Mn. Overall, the valence-band spectra of both compounds show good agreement with the calculated densities of states using GGA. This shows that the localizations of the Fe and Mn d states are rather insensitive to the type of order or disorder. It should also be noted that no pronounced effects of electron–electron correlations are observed. Figure 7.18 compares the valence-band spectra of CoFeMnGe excited by hard X-rays of different energies. With increasing photon energy, the cross-section of the s states decreases more slowly compared to the d states. The intensity in the energy range of the d bands is, at the lower photon-energy, increased compared to the range of the s bands. Both the intensity arising from the Mn t_2 majority states at approximately -4.1 eV and that arising from the d states at -1.3 eV become more pronounced at the lower excitation energy.

7.2.6 Summary

In summary, the quaternary intermetallic Heusler compounds CoFeMnZ (Z = Al, Ga, Si, Ge) were identified as potential half-metallic ferromagnets with high T_C by *ab-initio* electronic structure calculations. The compounds were then synthesized, the electronic and structural properties were analyzed at 300 K, and the magnetic properties were analyzed at 5 K. All the compounds exhibit cubic Heusler structures. A certain amount
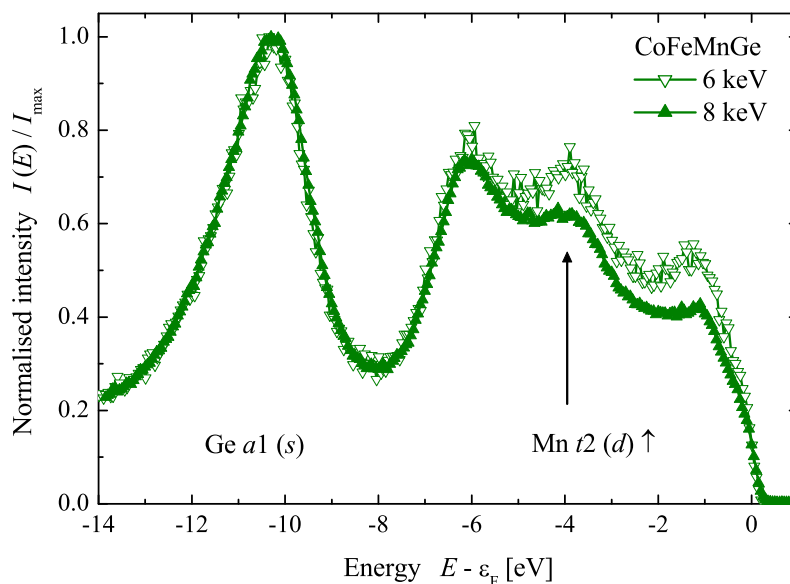
Figure 7.18: Valence band spectra of CoFeMnGe taken at different excitation energies.

of disorder was found in the XRD patterns of CoFeMnAl and CoFeMnSi, and cannot be excluded for CoFeMnGa and CoFeMnGe, as a result of the similar scattering amplitudes of the corresponding elements. A detailed study of order–disorder is required to clarify the complex crystallographic situation with four equivalent fcc sublattices. Anomalous XRD and extended X-ray absorption fine structure (EXAFS) studies will help to clarify this. It was, however, shown for related and recently reported quaternary half-metallic ferromagnetic Heusler compounds that disorder does not influence the electronic structures to an extent that destroys the half-metallicity [93] of the compounds.

Bulk sensitive hard X-ray photoelectron spectroscopy revealed the correct compositions of CoFeMnSi and CoFeMnGe. The multiplet splitting of the Mn $3s$ and $2p$ states suggests incomplete localization, $i.e.$, a metallic character of the d electrons in the compounds. The absence of multiplet effects in the Fe $2p$ states points to a weak role for Fe in the magnetic properties of the compounds, in agreement with the electronic structure calculations. Observed changes in the spectra (for valence bands) on the one hand and similarities (for core levels) when changing the excitation energy on the other hand are exclusively the result of differences in the cross-sections. This rules out surface influences for kinetic energies of 5 keV and above. The energy dependences of cross-sections and angular asymmetry parameters are revealed in the energy dependence of the $2p$ branching ratios of all three transition-metal elements.

The magnetic moments of the compounds are in fair agreement with the Slater–Pauling rule, indicating the half-metallicity and high spin-polarization required for

spintronics applications. The results are also in accordance with the electronic structure calculations and the results of X-ray magnetic circular dichroism [102]. The Mn atoms carry the highest local magnetic moments and, together with the Co atoms and the Slater–Pauling rule, dictate the orientation of the Fe moments. The Curie temperatures of all compounds are higher than 550 K, allowing use at room temperature and above. The many possible combinations in designing quaternary 1:1:1:1 Heusler compounds give enormous potential for many applications such as in spintronics or thermoelectrics and other areas of research, and clearly deserve further exploration in the future.

7.3 Quaternary Heusler Compounds $Co_{2-x}Rh_xMnZ$ ($Z=$ Ga, Sn, Sb): Electronic, Structural, and Magnetic Properties

7.3.1 Introduction

Half-metallic ferromagnetism (HMF) was initially predicted for the Heusler compounds NiMnSb by de Groot *et al.* [28] and Co_2MnSn by Kübler *et al.* [29] in 1983. It was brought to the center of scientific research by the recent development in electronics based on the combination of magnetic and semiconducting materials (so-called magnetoelectronics or spintronics). In these magnetic metals, the electrons are semiconducting in one spin channel while the other spin channel exhibits a metallic electronic structure. Several Heusler compounds were predicted to exhibit half-metallicity and are due to their high Curie temperatures (T_C) attractive candidates for spintronics applications [40, 63, 108]. Recently a tunable effect of the spin-orbit interaction becomes more and more important for new spintronic applications making use of the spin Seebeck or spin Hall effects [109, 110, 111]. Heusler compounds offer the opportunity of easily tunable electronic and magnetic properties, depending on their valence electron concentration. Heusler compounds containing elements with large spin-orbit interaction and high spin polarization are therefore highly prospective candidates for the desired effects. Introducing Rh or Ir into the Co_2-based HMF compounds may consequently allow the combination of both large spin-orbit interaction and high spin polarization.

In quaternary Heusler materials, the large number of possible combinations of atoms opens a wide range of possibilities for material design, in particular due to the predictability and tunability of their electronic and magnetic properties. It was reported very recently that several quaternary Heusler compounds exhibit the required properties for implementation in spintronic devices [93, 112]. The compounds investigated in those studies contained 3d elements exclusively on the X, X', and Y positions.

In this section a theoretical and experimental study on the so far not reported quaternary Heusler compounds CoRhMnZ ($Z=$ Ga, Sn, Sb) is presented. Compared to the convenient Co_2MnZ Heusler compounds [113, 114], one Co atom was substituted

by Rh. The differences between Co and Rh are the atomic radii and the magnetism, *i. e.* the atomic size of Rh is larger, it does not carry a considerable magnetic moment, and it exhibits an increased spin-orbit interaction. It is furthermore known that several Rh_2-based compounds crystallize in a tetragonally distorted variation of the Heusler structure [115]. Several tetragonal Heusler compounds exhibit electronic and magnetic properties highly prospective for spin-transfer torque applications [50, 51].

The CoRhMnZ compounds were synthesized and investigated experimentally in detail using powder X-ray diffraction (XRD) and SQUID magnetometry. Electronic structure calculations by *ab initio* methods were used to verify the assumed half-metallic ferromagnetic band structures of the compounds.

7.3.2 Electronic Structure

The electronic structures of the compounds were calculated as described in chapter 3. For all three compounds the optimization of the cubic lattice parameter revealed the lowest energy for the structure with Z on Wyckoff position 4a, Mn on 4b, Rh on 4c and Co on 4d in the lattice with space group $F\,\overline{4}3m$. Furthermore we checked the stability of the cubic structure by calculation of the elastic constants c_{ij}. The three independent elastic constants of the cubic structure (c_{11}, c_{12}, and c_{44}) were calculated by applying isotropic strain as well as volume conserving tetragonal and rhombohedral strains to the optimized primitive cubic cell.

The results of the calculated elastic properties are summarized in Table 7.12. The bulk modulus decreases with increasing Z of the main group element, *i. e.* the compounds become slightly softer. The elastic stability criteria for the cubic structure are found from the elastic constants (c_{ij}) [83]. The necessary conditions are: $c_{11}+2c_{12} > 0$, $c_{44} > 0$, $c_{11} - c_{12} > 0$ that is, the bulk, c_{44}- shear, and tetragonal shear moduli are all positive. From both, the elastic stability criteria as well as A_e, the CoRhMnZ compounds are stable in the cubic Y-type crystal structure, whereas CoRhFeGa exhibits a tetragonal instability as is seen from the negative value of A_e, *i. e.* the compound is not stable against tetragonal strain (it was verified experimentally that a single phase compound CoRhFeGa does not form, see Section 7.3.3).

The calculated band structure and density of states of CoRhMnGa, CoRhMnSn, and CoRhMnSb are shown in Figures 7.19, 7.20, and 7.21, respectively. It is evident that all compounds exhibit gaps at the Fermi energy in the minority spin channels and that all electronic structures are close to HMF.

7.3.3 X-ray Diffraction

The LiMgPdSn-type structure exhibits a primitive fcc cell with a basis containing four atoms on the Wyckoff positions 4a (0,0,0), 4b (1/2,1/2,1/2), 4c (1/4,1/4,1/4), and

Table 7.12: Structural properties of $Co_{2-x}Rh_xMnZ$ ($Z=$ Ga, Sn, Sb). Compared are the structure types as well as measured and calculated lattice parameters. The calculated elastic properties for the Y-type structure bulk modulus B, elastic constants c_{ij}, and elastic anisotropy $A_e = \frac{2c_{44}}{c_{11}-c_{12}}$ are given in addition for the pure compounds.

Compound	structure type	a_{exp} [Å]	a_{calc} [Å]	R_{wp} [%]	B [GPa]	c_{11} [GPa]	c_{12} [GPa]	c_{44} [GPa]	A_e
CoRhMnGa	$L2_1$	5.976	5.910	10.55	196	300	135	146	1.8
CoRhMnSn	Y	6.149	6.164	12.81	177	369	88	173	2.5
CoRhMnSb	X	6.048	6.203	16.42	151	296	89	217	4.2
$Co_{0.5}Rh_{1.5}MnSb$	$DO3$	6.152	6.258	20.14	-	-	-	-	-
CoRhFeGa	-	-	5.908	-	189	186	189	73	-97
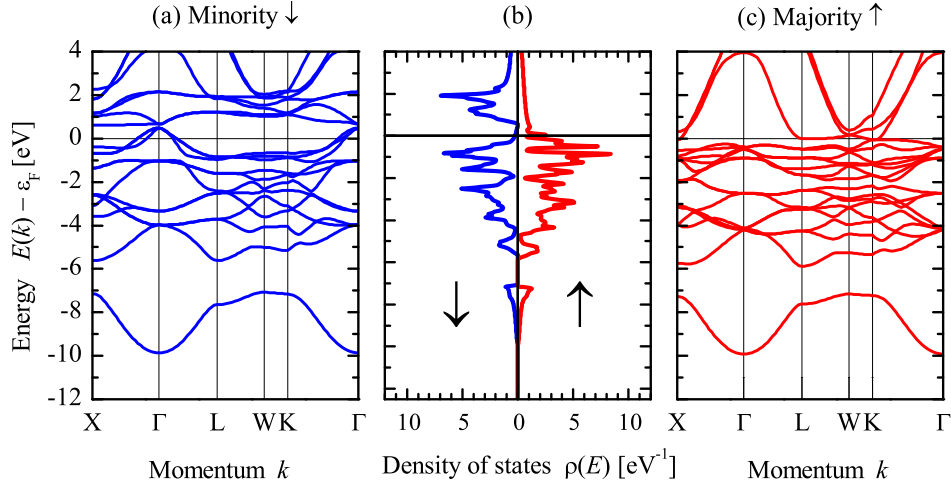
Figure 7.19: Band structure and density of states of CoRhMnGa. (a) minority bands, (b) density of states, (c) majority bands. Majority and minority spin densities are assigned by ↑ and ↓, respectively.
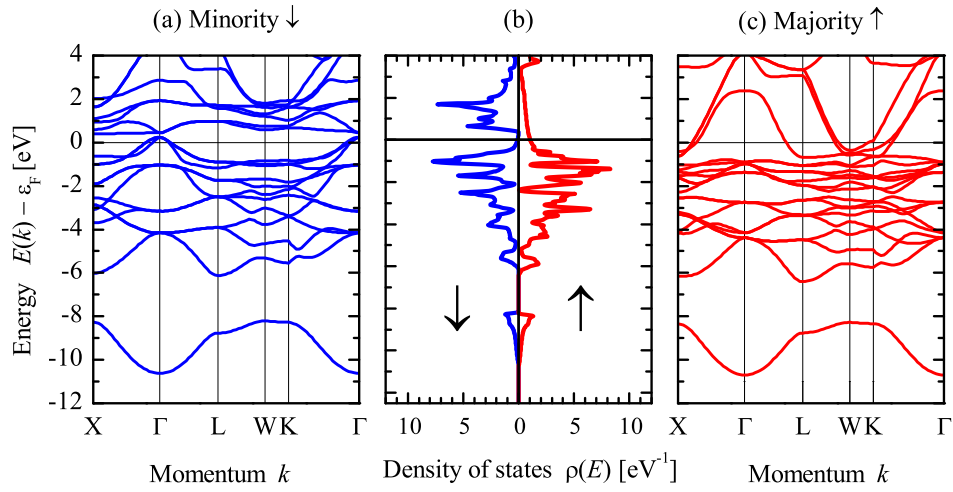
Figure 7.20: Same as Figures 7.19 but for CoRhMnSn.
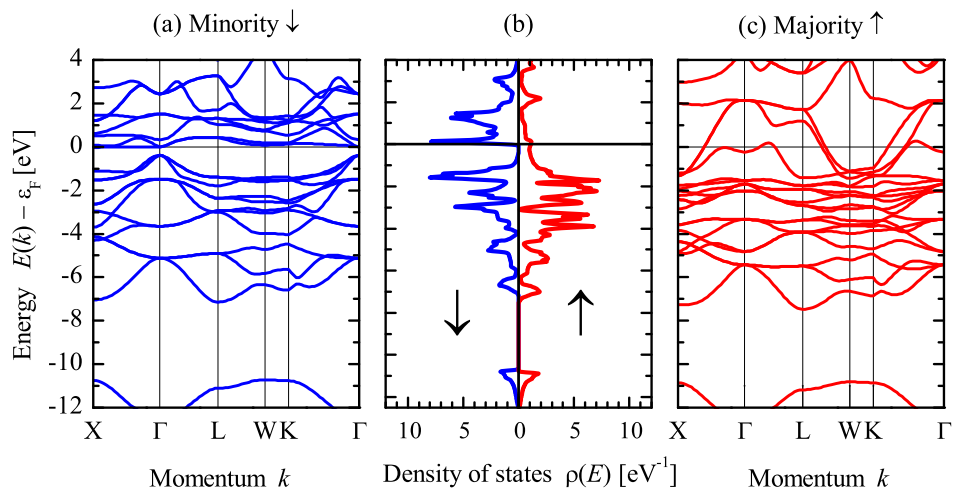
Figure 7.21: Same as Figures 7.19 but for CoRhMnSb.

4d (3/4,3/4,3/4). Three possible nonequivalent superstructures based on the different positions of the four atoms exist for this structure type [48] (see Table 7.13). Note that the exchange of the atoms between 4a and 4b or 4c and 4d positions and between the groups (4a, 4b) and (4c, 4d) does not change the structure due to the symmetry implied by the $F\bar{4}3m$ space group. The comparsion between the structure of quaternary and ternary Hesler compounds and corresponding primitive unit cells is shown in figure 7.22.
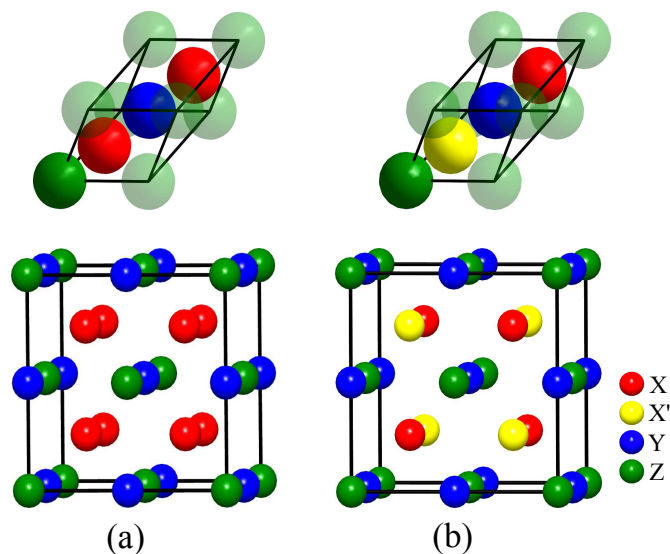
Figure 7.22: Crystal structures of the regular Heusler compound Cu_2MnAl (a) and quaternary compound LiMgPdSn (b). The corresponding primitive unit cells give insight into the different fcc sublattices.

Table 7.13: Different site occupation for the Y-type structure compared to $L2_1$. Z assigns the main group element. Note that the exchange of the atoms between 4a and 4b or 4c and 4d positions and between the groups $(4a, 4b) \leftrightarrow (4c, 4d)$ does not change the structure due to the symmetry implied by the $F\bar{4}3m$ space group. In $L2_1$ the positions (4c, 4d) become equivalent and combine to 8c.

	4a	4c	4b	4d
	(0,0,0)	(1/4,1/4,1/4)	(1/2,1/2,1/2)	(3/4,3/4,3/4)
Y Type I	Z	Rh	Mn	Co
Y Type II	Z	Mn	Rh	Co
Y Type III	Rh	Z	Mn	Co
$L2_1$	Z	Co	Mn	Co

The room temperature XRD patterns of the compounds are shown in Figure 7.23. On a first glance it is evident that all compounds exhibit cubic crystal structures. The

compound CoRhFeGa was also predicted to be a candidate for HMF and was therefore also synthesized and investigated. For this material, however, a mixture of two cubic phases was observed. These are most probably addressed to Co_2FeGa and Rh_2FeGa. This finding demonstrates that the Co-Rh substitution cannot be generalized to all parent ternary Co_2YZ compounds.
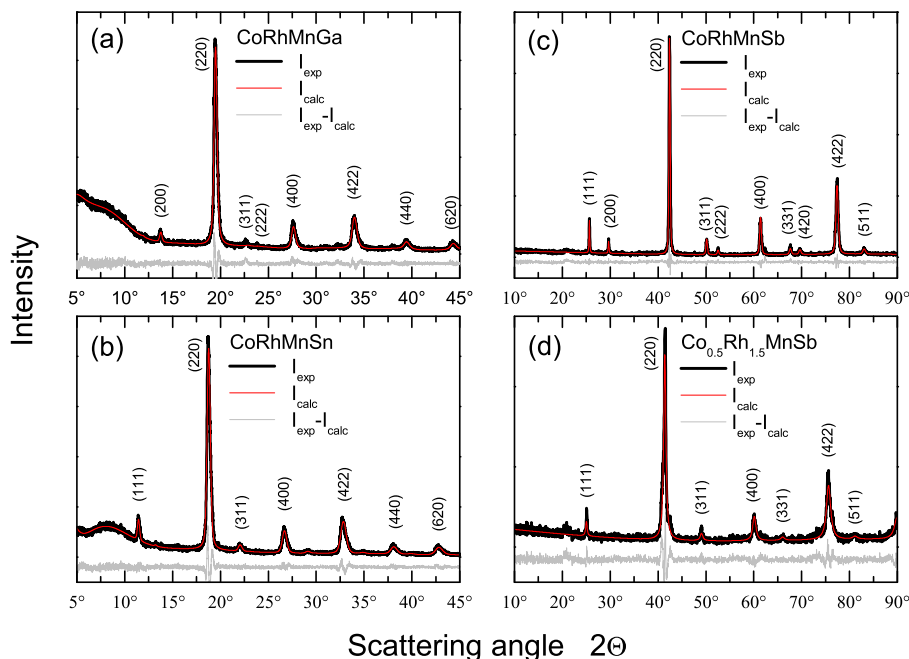
Figure 7.23: Powder XRD of polycrystalline $Co_{2-x}Rh_xMnZ$ (Z= Ga, Sn, Sb). The measurements were carried out at room temperature using Mo K_α radiation for $CoRhMnZ$ (Z= Ga, Sn) and Cu K_α for $Co_xRh_{2-x}MnSb$ ($x = 1, 1.5$).

Rietveld refinements of the data were performed using the TOPAS ACADEMIC software package [91]. The lattice parameters deduced from the refinements as well as the weighted-profile R-factors R_{wp} are summarized in Table 7.12 and compared to the calculated structural data. For the Heusler compounds a well-ordered crystal structure is desired in order to conserve the HMF electronic structure because anti-site disorder can reduce the spin polarization. Perfectly ordered regular Heusler compounds such as Co_2MnZ crystallize in the regular $L2_1$ structure. In this structure, the Wyckoff position 8c is occupied by equivalent atoms (Co). The Mn and Z atoms occupy the 4b, and 4a Wyckoff positions, respectively. Substitution of Co by Rh leads to the Y-type structure ($F\bar{4}3m$ symmetry) where 8c is split into 4c and 4d. However, if Co

and Rh are randomly distributed among the (4c, 4d) positions then the structure is again transformed to $L2_1$, which in that case represents disorder. In fact quaternary or inverse Heusler compounds are prone to this type of disorder [116, 117, 118, 119].

The structural models in the Rietveld refinements were modified in order to account for anti-site disorder in the compounds. The R_{wp} values listed in Table 7.12 correspond to the respective best structural model derived for the compounds. For CoRhMnGa it was found that the structure is $L2_1$ disordered (Co and Rh). However, a conclusive declaration of order is particularly difficult for CoRhMnGa due to almost equal scattering amplitudes of Co, Mn, and Ga for the energy of the X-rays used. CoRhMnSb was identified to exhibit an X-type of disorder. In this case the Rh and Mn atoms mix. The best fit was obtained for an occupancy of 30% of Mn on the Rh position and vice versa. The bad R_{wp} value of 16.42% is explained by the occurrence of an unidentified impurity in the XRD pattern. The amount of this impurity is rather small ($\leq 5\%$). The $Co_{0.5}Rh_{1.5}MnSb$ alloy exhibits a DO_3-type of disorder. The optimum fit was obtained for a random distribution of Co, Rh, and Mn atoms. The types of disorder determined for CoRhMnSb and $Co_{0.5}Rh_{1.5}MnSb$ explain the huge discrepancy between the theoretical and experimental lattice parameters of these compounds. When the small Mn atoms replace the large Rh atoms, the sizes of atoms in the corresponding layers become more similar (Co/Mn and Rh/Sb) and the unit cell can contract. The bad R_{wp} value of 20.14% for $Co_{0.5}Rh_{1.5}MnSb$ is attributed to the very broad reflexes in the XRD pattern. The large shoulders on the right sides of the (220) and (422) reflexes may indicate a structural distortion. A further increase of the Rh content may lead to a tetragonal distortion (the compound Rh_2MnSb is known to exhibit a tetragonally distorted Heusler structure) [115]. Finally, the CoRhMnSn compound was found to be ordered and to crystallize in the proposed Y-structure. Compared to their ternary regular Heusler relatives Co_2MnGa, Co_2MnSn, and Co_2MnSb, the lattice parameters of CoRhMnGa, CoRhMnSn, and CoRhMnSb are larger, respectively [120, 121]. With increasing atomic radii of the Z atoms this difference decreases.

7.3.4 Magnetic Properties

The magnetic properties of the polycrystalline samples were investigated by means of SQUID magnetometry. The field dependent magnetic moments at low temperature (5 K) are displayed in Figure 7.24. Obviously, all compounds exhibit soft-magnetic hysteresis loops. The saturation magnetic moments of the compounds and several other experimentally determined or calculated magnetic parameters are summarized in Table 7.14. According to the generalized Slater-Pauling rule [31, 108] for half-metallic Heusler compounds, the magnetic moment for CoRhMnGa should amount to 4 μ_B, for CoRhMnSn to 5 μ_B, and for CoRhMnSb and $Co_{0.5}Rh_{1.5}MnSb$ to 6 μ_B. The cal-

culated magnetic moments for the assumed ordered Y-structures are in good agreement with these values. The experimentally determined magnetic moments aside from CoRhMnSn deviate from the Slater-Pauling values, and the corresponding compounds are thus probably not 100% half-metallic. This is evident due to the structural disorder as explained in Section 7.3.3. The value of 4.83 μ_B for CoRhMnSn on the other hand confirms the derived ordered Y structure and the proposed half-metallicity. The small deviation of 0.17 μ_B can be attributed to sample inhomogeneities, partial surface oxidation, the weighting and measurement errors, and to the measurement temperature of 5 K.
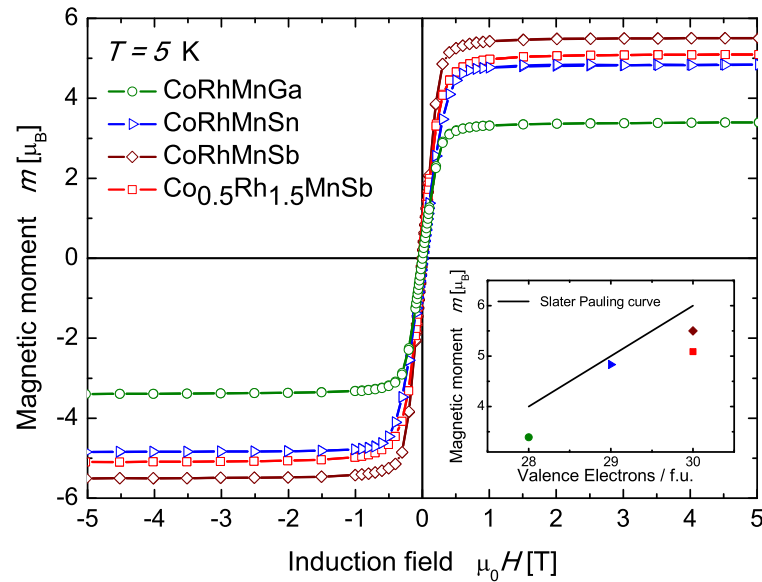
Figure 7.24: Field dependent magnetic moments of $Co_{2-x}Rh_xMnZ$ (Z= Ga, Sn, Sb). The hysteresis loops were measured at $T = 5$ K, the values exhibit uncertainties of $\pm 0.5\%$. The inset shows the saturation magnetic moments compared to the generalized Slater-Pauling curve.

Figure 7.25 displays the temperature dependent magnetic moments of the investigated samples. The high temperature magnetic moments exhibit larger uncertainties due to the lower amounts of material used in the measurements. This leads to deviations of approximately ± 0.05 μ_B in the overlapping temperature range. The high temperature magnetic moments were therefore rescaled to fit to the low temperature data. From the measured magnetization curves $M_{exp}(T)$, T_C and the total angular momentum quantum number J can be obtained by fitting the corresponding curves $M_{mf}(T)$ from the mean field theory. In the mean field approximation, the magnetization must fulfill the equation:

$$M_{mf}(T) = M_0 B_J \left(J\frac{T_C}{T} \left(c_B + \frac{3}{J+1} \frac{M}{M_0} \right) \right), \qquad (7.4)$$

where M_0 is the saturation magnetization, $B_J(\cdot)$ is the Brillouin function and c_B is a constant that depends on the external, applied field. c_B is defined by

$$c_B \equiv \frac{g\mu_B B}{k_B T_C}, \qquad (7.5)$$

where g is the gyromagnetic factor, μ_B is the Bohr magneton, $B = \mu_0 H$ is the external induction field, and k_B is the Boltzmann constant. The function $M_{mf}(T)$ can be fitted to the experimental data by minimizing the mean square deviation

$$\chi^2 \equiv \sum_k \left(M_{mf}(T_k) - M_{exp}(T_k) \right)^2, \qquad (7.6)$$

summed over all data points $M_{exp}(T_k)$. The fitting procedure provides the T_C of the considered materials as shown in Table 7.14. The high T_C of CoRhMnSn supports its attractiveness for spintronics applications. The shape of the temperature dependent magnetization of CoRhMnSn indicates the presence of an impurity since the expected drop of magnetization is not pronounced. An impurity concentration below the detection limit of XRD cannot be excluded.

Table 7.14: Measured and calculated magnetic moments of the compounds $Co_{2-x}Rh_x MnZ$ ($Z=$ Ga, Sn, Sb). The measured values exhibit uncertainties of $\pm 0.5\%$. All values are given in μ_B. The Curie temperatures T_C were derived from mean field fits.

Compound	m_{exp}(5 K)	m_{exp}(300 K)	T_C [K]	m_{calc}	m_{Rh}	m_{Co}	m_{Mn}
CoRhMnGa	3.39	2.27	408	4.11	0.23	0.89	3.12
CoRhMnSn	4.83	4.61	620	5.02	0.36	1.20	3.56
CoRhMnSb	5.50	4.87	534	5.98	0.62	1.50	3.78
$Co_{0.5}Rh_{1.5}MnSb$	5.09	4.02	424	5.06	0.41	1.50	3.67

7.4 Summary

In summary, the quaternary Heusler compounds $Co_{2-x}Rh_x MnZ$ ($Z =$ Ga, Sn, Sb) were predicted by *ab initio* electronic structure calculations to be HMF. The compounds were synthesized by arc melting and subsequent annealing and characterized by powder XRD and SQUID. The ab-initio calculations hint on stable cubic structures for the Mn containing compounds. The structural investigation revealed that
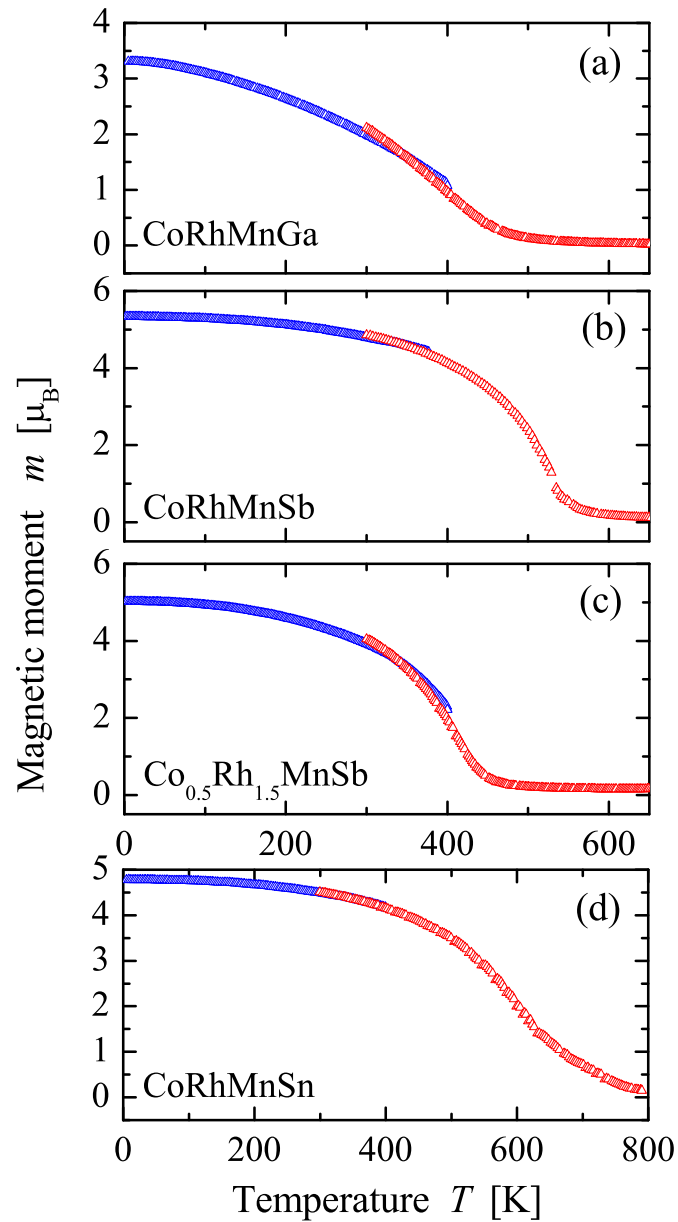
Figure 7.25: Temperature dependent magnetic moments of (a) CoRhMnGa, (b) CoRhMnSb, (c) $Co_{0.5}Rh_{1.5}MnSb$, and (d) CoRhMnSn. The blue parts of the curves correspond to the low temperature SQUID measurements(5-400 K), and the red parts to the high temperature measurements (400-790 K). All measurements were performed in an induction field of $\mu_0 H = 1$ T.

the crystal structures of all compounds aside from CoRhMnSn exhibit different types of anti-site disorder. The quaternary Heusler compounds seem to be more susceptible for anti-site disorder compared to their ternary relatives. It is therefore necessary to improve the synthesis to increase the order of the compounds. The magnetic moments of the disordered compounds deviate to different amounts from the Slater-Pauling rule indicating that 100% spin polarization are not realized in CoRhMnGa, CoRhMnSb, and in the alloy $Co_{0.5}Rh_{1.5}MnSb$. The low temperature magnetic moments vary with the composition and are in the range of 3.4 to 5.5 μ_B. The Curie temperatures were found from measurements in induction fields of up to 1 T by applying molecular field fits respecting the applied field and are in the range of 400 to 620 K depending on the composition.

Exchange of one Co in Co_2MnSn by Rh results in the stable, well-ordered compound CoRhMnSn. This exchange of one of the *"magnetic"* Co atoms by a *"non-magnetic"* Rh atom keeps the magnetic properties and half-metallicity intact. Those properties are completely determined by the Mn atoms together with valence electron count and do not depend much on the remaining type of atoms. This behavior allows to increase the spin-orbit interaction at one of the sites while keeping all other properties as a precondition for applications and physical effects relying on a large spin-orbit interaction. The ordered compound CoRhMnSn is a HMF with a saturation magnetization of 5 μ_B. It furthermore exhibits a high T_C of 620 K allowing utilization at room temperature and above.

8 Mn$_2$-based Heusler Alloys

Tetragonally distorted Heusler compounds are currently attracting a lot of interest as materials for spin-transfer torque (STT) applications [73, 74]. Several Heusler compounds were predicted to exhibit tetragonal distortions [122, 123] but up to the present only few tetragonal Heusler materials have been discovered. Mn$_{3-x}$Ga are the most prominent alloys among them [40, 50, 51]. These exhibit the required high spin polarization and Curie temperatures T_C as well as low saturation magnetizations M_S and Gilbert damping constants [124, 125, 126, 127, 128]. They are particularly interesting due to their perpendicular magnetic anisotropy (PMA), which was realized in thin films opening the door for application in STT magnetic random access memories (STT-MRAMs) [55].

8.1 Tuning the Magnetism of the Heusler Alloys Mn$_{3-x}$Co$_x$Ga from Soft and Half-Metallic to Hard-Magnetic for Spin-Transfer Torque Applications

The ferrimagnetic cubic Heusler compound Mn$_2$CoGa has been studied in theory and from the experimental point of view by several groups [129, 130, 131, 132]. It exhibits a total magnetic moment of 2 μ_B following the generalized Slater-Pauling rule for half-metallic Heusler compounds [6] and it was predicted to have a T_C of above 800 K [129, 132]. The alloys Mn$_{3-x}$Co$_x$Ga have been studied using X-ray absorption spectroscopy (XAS) and X-ray magnetic circular dichroism (XMCD) [133], where an antiparallel alignment of the Mn atoms on different lattice sites corresponding to a ferrimagnetic order has been shown. Here the corresponding structural and detailed magnetic properties of these materials are presented. They offer particular advantages for STT applications, which require minimum switching currents while maintaining thermal stability. The tetragonal Mn-rich alloys ($x = 0.1 - 0.4$) exhibit hard-magnetic properties similar to Mn$_3$Ga, and the cubic Co-rich alloys ($x = 0.6 - 1$) are soft-magnetic half-metallic ferrimagnets. This allows an easy tunability of perpendicular magnetic anisotropy by variation of the Co content. Employing a soft-magnetic, half-metallic material with in-plane magnetization as the switching layer of a magnetic tunnel junction and a hard-magnetic composition with large perpendicular magnetic anisotropy

as the reference layer, the efficiency and the speed of switching can be increased [134]. Furthermore, all alloys were found to exhibit high T_C of 700 K and above. Besides the prominent Co$_2$-based Heusler compounds the Mn$_2$-based cubic compounds are the second large family of half-metals, in this case ferrimagnets, following the generalized Slater-Pauling curve.

8.1.1 Crystal Structure

The regular Heusler compounds X_2YZ crystallize in the cubic $L2_1$ structure ($Fm\bar{3}m$, space group no. 225) with Cu$_2$MnAl as prototype [27]. If the atomic number $Z(Y) > Z(X)$, then the inverse Heusler structure $XYXZ$ (prototype AgLi$_2$Sb, $F\bar{4}3m$, space group no. 216) is formed. A well-studied example is the compound Mn$_2$CoSn or, more exactly, (MnCo)MnSn [44, 45, 116]. The Mn atoms on the octahedrally coordinated lattice sites possess an oxidation state of +3 (Mn^{3+}, d^4) [29]. This electron configuration is energetically unfavorable, and energy can be gained by a distortion of the octahedron. Both, an elongation and a compression are possible. This phenomenon is referred to as the Jahn-Teller-effect. In case of Mn$_{3-x}$Co$_x$Ga, the cubic unit cell undergoes an elongation along the c-axis [40] leading to an inverse tetragonal cell ($I\bar{4}m2$, space group no. 119) The lattice parameters determined by the Rietveld refinements (see Table 8.1) were analyzed as shown in Figure 8.1(c). The cell volumes of the cubic compounds decrease linearly as expected because of the smaller atomic radius of Co compared to the Mn atom. Those of the purely tetragonal alloys do not evidently depend on x. As seen from Table 8.1 this is due to the fact that the lattice parameter c decreases with increasing x in the tetragonal alloys while a at the same time increases, resulting in constant cell volumes. However, the c/a ratio and thus the tetragonal distortion decreases with x. The alloy Mn$_{2.5}$Co$_{0.5}$Ga is a mixture of both cubic and tetragonal phases with different cell volumes.

8.1.2 Magnetic Properties

The magnetic properties of Mn$_{3-x}$Co$_x$Ga determined by SQUID magnetometry are summarized in Table 8.1. The hysteresis loops of three selected compositions ($x=0.3$, 0.5, and 1) in comparison to Mn$_3$Ga [51] and the Slater-Pauling curve are displayed in Figure 8.2(a). It was found that all tetragonal alloys, $x = 0.1 - 0.4$, are hard-magnetic similar to Mn$_3$Ga and exhibit low saturation magnetic moments that decrease with x. The moments follow a linear dependency according to $m_{tetra} = 1 - 1.34\,x$. The magnitude of the magnetic moments indicates a ferrimagnetic type of order as expected from antiferromagnetic coupling Mn atoms on the different lattice sites. The cubic alloys, $x = 0.6 - 1$, exhibit soft-magnetic behavior and follow a linear dependency with $m_{cubic} = N_v - 24$. This is a typical Slater-Pauling-type behavior similar to the
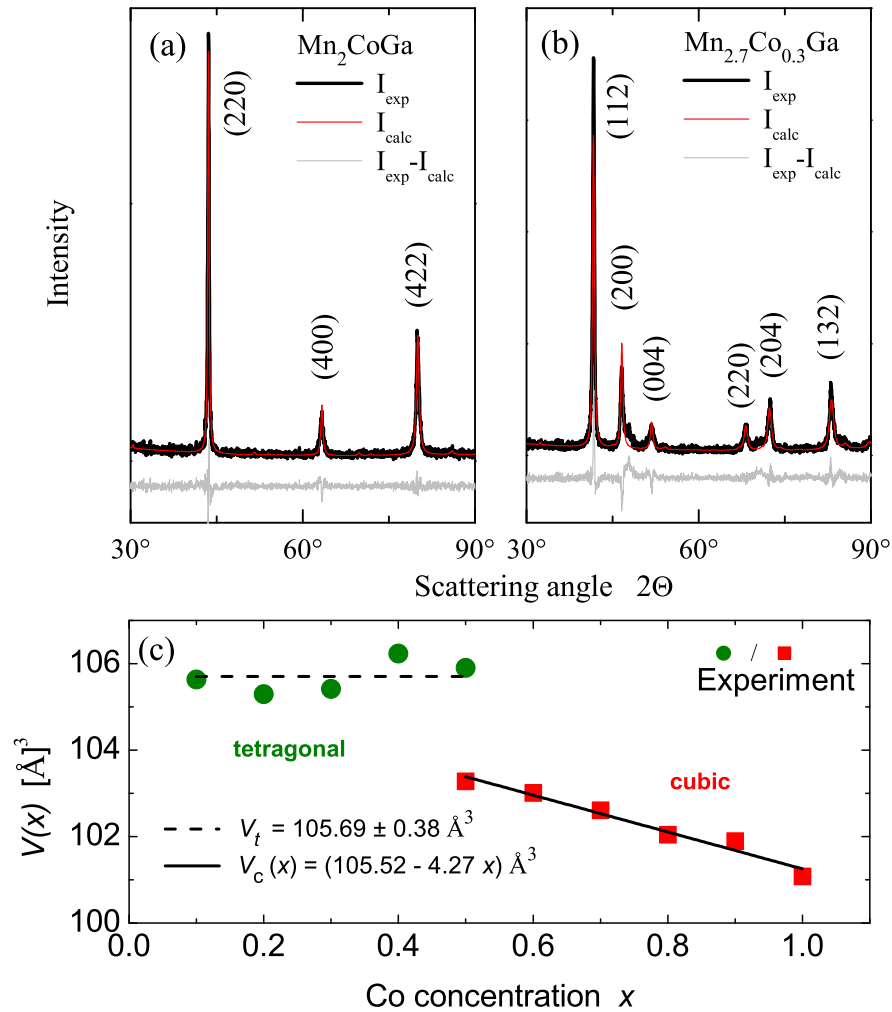
Figure 8.1: Structural characterization of $Mn_{3-x}Co_xGa$. The XRD patterns and Rietveld refinements are shown for a cubic (Mn_2CoGa) and a tetragonal composition ($Mn_{2.7}Co_{0.3}Ga$). The cell volumes of tetragonal and cubic alloys in dependency on x are shown together with the corresponding linear fits in (c).

Table 8.1: Structural and magnetic properties of the Mn$_{3-x}$Co$_x$Ga alloys. The lattice parameters were determined at room temperature. V is the volume of the unit cell, m is the magnetic moment measured at 5 K in a magnetic induction field of 5 T, $i.\,e.$ in or close to magnetic saturation. H_c is the coercive field, B_r the magnetic remanence, both determined at 5 K.

x	a [$\mathring{A}$]	c [$\mathring{A}$]	c/a	V [$\mathring{A}^3$]	m [μ_B]	T_C [K]	H_c [Am^{-1}]	B_r [T]
0.1	3.871	7.049	1.82	105.63	0.90	787	116	83.1
0.2	3.869	7.034	1.82	105.30	0.78	767	111	78.1
0.3	3.874	7.024	1.81	105.42	0.58	750	89	67.1
0.4	3.892	7.013	1.80	106.23	0.49	736	55	38.2
0.5	3.878	7.042	1.82	105.90	0.95	727	26	7.3
	5.911	-	-	103.28				
0.6	5.907	-	-	103.01	1.18	717	-	-
0.7	5.898	-	-	102.61	1.37	714	-	-
0.8	5.888	-	-	102.04	1.57	713	-	-
0.9	5.885	-	-	101.89	1.62	713	-	-
1	5.869	-	-	101.08	2.02	718	-	-

related half-metallic ferromagnetic Co$_2$-based Heusler compounds [94]. The phase mixture Mn$_{2.5}$Co$_{0.5}$Ga evidently has a weakly hard-magnetic hysteresis loop indicating the tetragonal structure but on the other hand exhibits a perfect Slater-Pauling saturation magnetic moment in line with the other cubic alloys. The slope of the magnetic moments of the tetragonal alloys is not in quantitative consistence with the XMCD results [133]. This has been explained by the insufficient external magnetic field of 2 T used in the XMCD study impeding magnetic saturation. High-temperature SQUID measurements were performed to determine T_C, which are summarized in Table 8.1 and plotted in Figure 8.2(b). All alloys investigated exhibit T_C above 700 K. T_C of the cubic alloys are more or less constant while in the tetragonal alloys T_C decrease with x. This decrease is correlated with the c/a ratios of the tetragonal alloys, which are strongly connected to their magnetic anisotropies. The relation between T_C and the magnetic anisotropy in these alloys can be clarified by an investigation of thin films, which is the next step on the way to operating devices.

From Table 8.1, which summarizes the structural and magnetic data, it is apparent that Mn$_{3-x}$Co$_x$Ga becomes magnetically softer with decreasing Mn content (increasing Co content). The coercivities H_c and magnetic remanences B_r consequently decrease with x. Besides their useful properties for STT applications, the tetragonal alloys Mn$_{3-x}$Co$_x$Ga offer potential as permanent magnets, a branch of research, where new rare-earth-free materials are nowadays strongly desired.
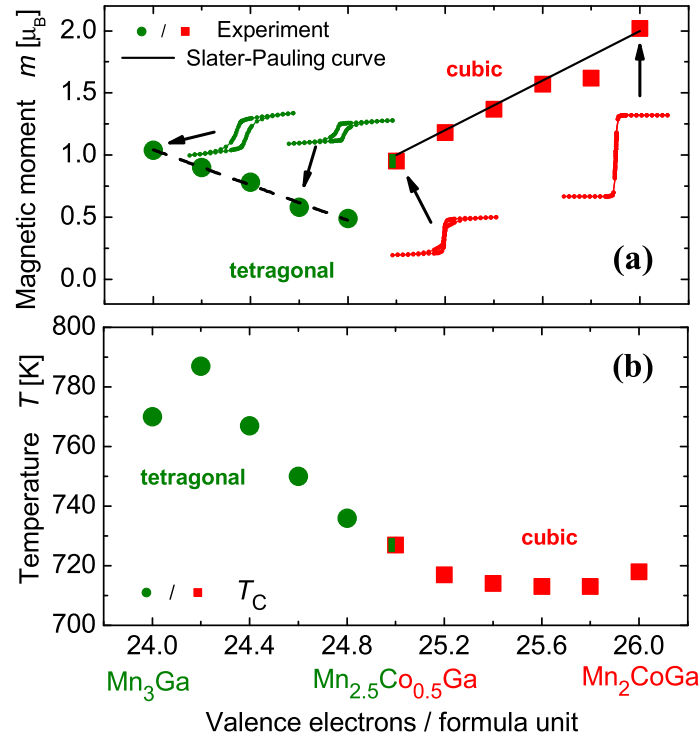
Figure 8.2: Magnetic properties of Mn$_{3-x}$Co$_x$Ga. The experimentally determined saturation magnetic moments at $T = 5$ K are compared to different types of linear dependencies shown as full lines for cubic (Slater-Pauling-curve) and dashed lines for tetragonal alloys in (a). Tetragonal and cubic compounds are represented by circles and squares, respectively. Heights and widths of the inserted hysteresis loops correspond to the factual ratios. The T_C values of all alloys are plotted in (b).

8.1.3 Summary

In conclusion the multifaceted Heusler alloys Mn$_{3-x}$Co$_x$Ga have been synthesized and investigated. Depending on the Co concentration x the compounds exhibit cubic or tetragonal Heusler structures. The tetragonal alloys are hard-magnetic, have low saturation magnetic moments, and high T_C. They are thus highly attractive for STT applications and represent new rare earth free permanent magnets. The cubic alloys are soft-magnetic and also exhibit high T_C. Besides the Co$_2$-based half-metallic ferromagnets, the cubic Mn$_2$-based compounds and alloys represent the second class of

materials exhibiting the typical 100% spin polarized Heusler half-metallic electronic structure and obeying the Slater-Pauling rule. A continuous tunability of magnetic and structural properties simply depending on the Co concentration can easily be realized in these materials. With respect to STT it is expected that due to the strong relation to Mn$_3$Ga a perpendicular magnetic anisotropy can be realized in thin films of tetragonal Mn$_{3-x}$Co$_x$Ga alloys. In that case, very similar compositions could be used as reference and as switching layers allowing for a strong increase of efficiency in the STT devices.

8.2 Structural, and magnetic properties of Mn$_{2-x}$Rh$_{1+x}$Sn Heusler materials

The ferromagnetic cubic Heusler compound Rh$_2$MnSn has been studied in theory and from the experimental point of view by several groups [49, 135, 136, 137, 138, 139]. It exhibits a total magnetic moment of 4.14 μ_B [139] and it was predicted to have a T_C between 410 K to 420 K in different literatures [49, 135, 136, 137, 138, 139]. The present work reports on the structural characteristic of Mn$_{2-x}$Rh$_{1+x}$Sn with x varying from 0 to 1 in steps of $x = 0.2$ and their magnetic properties. The structure was investigated using powder X-ray diffraction (XRD). The magnetic properties were studied using induction field dependent magnetometry by a super conducting quantum interference device (SQUID).

8.2.1 X-ray diffraction

The crystalline structure of the Mn$_{2-x}$Rh$_{1+x}$Sn series was examined using XRD with excitation by Cu K$_\alpha$ radiation. The measurements were performed at room temperature. As examples, Figure 8.3 shows the XRD results for Mn$_2$RhSn and Mn$_{1.5}$Rh$_{1.5}$Sn. Rietveld refinements of the data were performed using the TOPAS ACADEMIC software package [91]. The XRD data verify that Mn$_2$RhSn crystallizes in the inverse tetragonal structure type ($I\bar{4}m2$, space group no. 119). Splitting of the cubic (220) reflex into the (112) and (200) reflexes in the related diffraction pattern is an evidence for existance of tetragonal structure. With increasing amount of Rh, both tetragonal and cubic structure for Mn$_{1.8}$Rh$_{1.2}$Sn and inverse cubic structure for Mn$_{2-x}$Rh$_{1+x}$Sn (x= 0.5, 0.6, 0.8) are observed. Rh$_2$MnSn crystallizes in the regular cubic Heusler structure [49, 135, 136].

The lattice parameters found from a Rietveld refinement of the powder XRD data are summarised in Table 8.2.
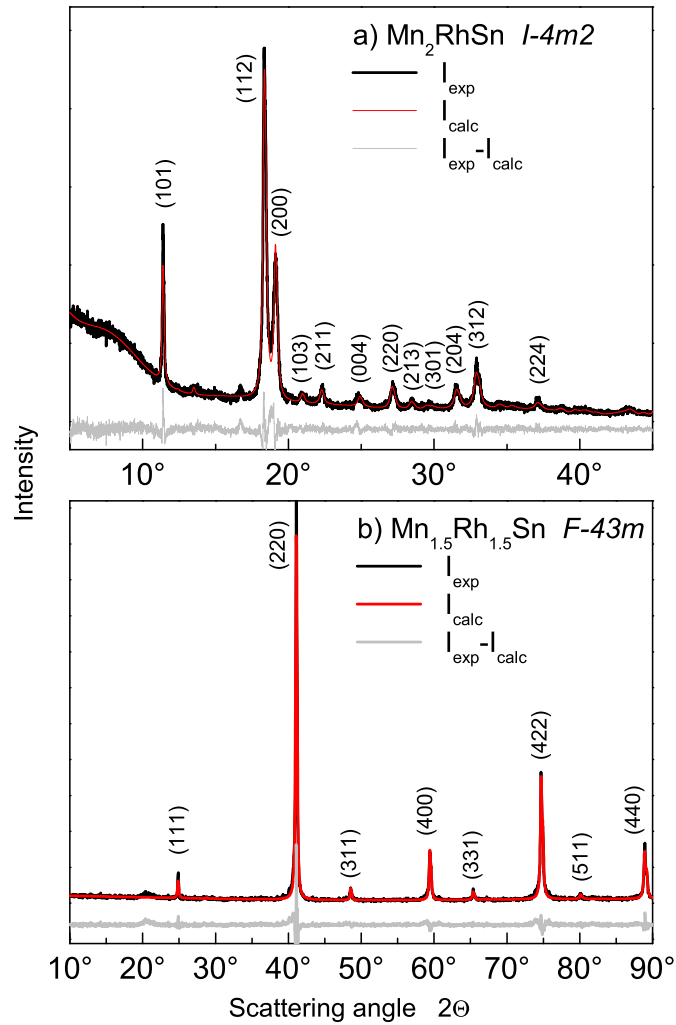
Figure 8.3: Powder diffraction patterns of Mn$_{2-x}$Rh$_{1+x}$Sn. The measured diffrac-
tograms for Mn$_2$RhSn and Mn$_{1.5}$Rh$_{1.5}$Sn are compared to the fits from
a Rietveld refinement. The spectra were excited using Cu K$_\alpha$ radiation for
Mn$_{1.5}$Rh$_{1.5}$Sn and Mo K$_\alpha$ radiation for Mn$_2$RhSn recorded at $T = 300$ K.

Table 8.2: Lattice parameters, magnetic moments and Curie temperatures T_C of the Mn$_{2-x}$Rh$_{1+x}$Sn compounds. As found from a Rietveld refinement of the XRD data, the lattice parameters a and c are tabulated for increasing Rh content. The ratios c/a are calculated from the measured values of a and c. Magnetic moments of the compounds are available at 5 K and 300 K. Also the amounts of magnetic moment from the Slater-Pauling rule are given in the table.

alloy	a [Å]	c [Å]	c/a	Hys	m_{exp}(5 K) [μ_B]	m_{SP} [μ_B]	m_{exp}(300 K) [μ_B]	T_C [K]
Mn$_2$RhSn	4.2945	6.6055	1.54	hard	1.87	3	0.57	305
Mn$_{1.8}$Rh$_{1.2}$Sn	4.29 6.2035	6.61 -	1.54 -	hard	2.84	3.40	0.75	320
Mn$_{1.5}$Rh$_{1.5}$sn	6.2207	-	-	soft	4.01	4.00	2.21	387
Mn$_{1.4}$Rh$_{1.6}$Sn	6.2202	-	-	soft	4.04	4.20	2.63	391
Mn$_{1.2}$Rh$_{1.8}$Sn	6.2243	-	-	soft	4.51	4.60	3.43	398
Rh$_2$MnSn	6.2320	-	-	soft	4.14	5.00	-	410

8.2.2 Magnetic properties

The magnetic properties of the polycrystalline samples were investigated by means of SQUID magnetometry. The field dependent magnetic moments at $T = 5$ K and $T = 300$ K are displayed in Figure 8.4 (a) and (b), respectively. The inset shows the zoom of the hysteresis at $T = 5$ K for Mn$_2$RhSn and Mn$_{1.8}$Rh$_{1.2}$Sn. According to Figure 8.4 all cubic compounds exhibit soft magnetic behavior while tetragonal compounds (Mn$_2$RhSn and Mn$_{1.8}$Rh$_{1.2}$Sn) are hard magnets. The saturation magnetic moment at 5 K and 300 K, the Slater-Pauling magnetic moments, and the Curie temperature of the compounds are summarized in Table 8.2. Unfortunately for all the compounds, T$_c$ is too low (less than 410 K) to make them relevant for technological applications. The saturation magnetic moments of cubic samples are in good agreement with the Slater-Pauling magnetic moments and exhibit the typical 100% spin polarized Heusler half-metallic electronic structure obeying the Slater-Pauling rule. The tetragonal Mn$_2$CoSn alloy which is a hard magnet has low saturation magnetic moment which makes it attractive as a candidate for STT applications.

8.2.3 Summary

In summary, Mn$_2$RhSn crystallizes in the inverse tetragonal structure ($I\bar{4}m2$, space group no. 119) and shows hard magnetic hysteresis behavior. As Mn$_2$RhSn has a tetragonal structure, it does not follow the Slater-Pauling rule and low saturation magnetic moment of it beside its hard magnetic properties can make it suitable for STT applications. With substituting Mn by Rh, the inverse cubic structure for Mn$_{2-x}$Rh$_{1+x}$Sn
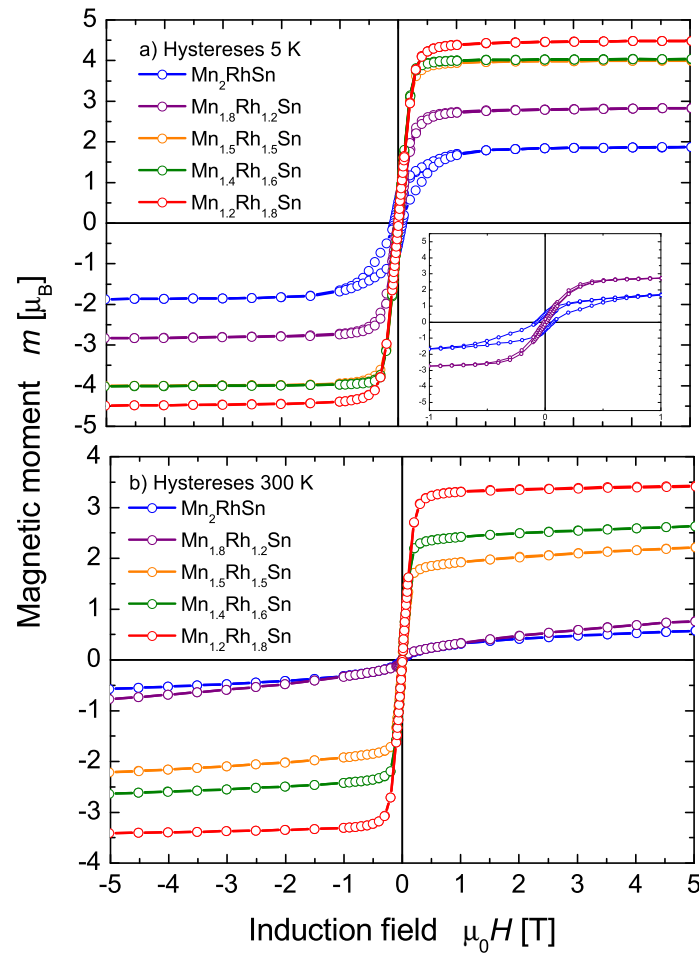
Figure 8.4: Magnetic properties of Mn$_{2-x}$Rh$_{1+x}$Sn. The MH-curves were measured at $T = 5$ K (a) and $T = 300$ K (b). The inset shows a zoom of the hysteresis at $T = 5$ K which makes the hard magnetic behavior of Mn$_2$RhSn and Mn$_{1.8}$Rh$_{1.2}$Sn more clear.

(x = 0.5, 0.6, 0.8) and regular cubic structure for Rh$_2$MnSn is observed. All cubic samples show perfect Slater-Pauling behavior and soft hysteresis loops and exhibit the typical 100% spin polarized Heusler half-metallic electronic structure. Both cubic and tetragonal phases exist for Mn$_{1.8}$Rh$_{1.2}$Sn and it shows similar magnetic properties with Mn$_2$RhSn.

9 Summary and Outlook

This work emphasizes on the prediction of half-metallicity in the quaternary Heusler compounds and their potential for spintronic applications and also on the structural properties of Mn_2-based Heusler alloys and tuning the magnetism of them for spin-transfer torque applications.

In Section 5.1, $XX'MnGa$ (X = Cu, Ni and X' = Fe, Co) quaternary Heusler compounds have been identified using a theoretical approach for preselection. As predicted by these calculations NiFeMnGa and NiCoMnGa are half-metallic ferromagnets. These are the first reported Ni-based half-metallic ferromagnets within the huge family of Heusler compounds. CuCoMnGa turned out to be a regular metallic ferromagnet due to the closed shell character of the Cu d electrons. NiFeMnGa has a Curie temperature that is too low to make it relevant for technological applications but NiCoMnGa with a high spin polarization, high magnetic moment, and Curie temperature is an interesting new material for spintronics applications. A large resource of quaternary Heusler materials is open and to be investigated in future to find prospective materials for several applications.

In Section 5.2, the quaternary intermetallic Heusler compounds CoFeMnZ (Z = Al, Ga, Si, Ge) were identified as potential half-metallic ferromagnets with high T_C by *ab-initio* electronic structure calculations. Electronic, structural, and magnetic properties of these compounds were analyzed. All compounds exhibit cubic Heusler structures. A certain amount of disorder was found in the XRD patterns of CoFeMnAl and CoFeMnSi and cannot be excluded for CoFeMnGa and CoFeMnGe due to similar scattering amplitudes of the corresponding elements. A detailed study of order/disorder is required to clarify the complex crystallographic situation with four equivalent fcc sublattices. Anomalous XRD and extended X-ray absorption fine structure (EXAFS) will provide help. It was, however, shown for related and recently reported quaternary half-metallic ferromagnetic Heusler compounds that disorder does not influence the electronic structures to an amount that destroys half-metallicity of the compounds [93]. The magnetic moments of the compounds are in fair agreement with the Slater-Pauling rule indicating the half-metallicity and high spin polarization required for spintronics applications. The Curie temperatures of all compounds are higher than 550 K allowing for utilization at room temperature and above.

In Section 5.3, the quaternary Heusler compounds $Co_{2-x}Rh_xMnZ$ (Z = Ga, Sn,

Sb) were predicted by *ab initio* electronic structure calculations to be half-metallic ferromagnet. The ab-initio calculations hint on stable cubic structures for the Mn containing compounds. The structural investigation revealed that the crystal structures of all compounds aside from CoRhMnSn exhibit different types of anti-site disorder. The quaternary Heusler compounds seem to be more susceptible for anti-site disorder compared to their ternary relatives. It is therefore necessary to improve the synthesis to increase the order of the compounds. The magnetic moments of the disordered compounds deviate to different amounts from the Slater-Pauling rule indicating that 100% spin polarization are not realized in CoRhMnGa, CoRhMnSb, and in the alloy $Co_{0.5}Rh_{1.5}MnSb$. The low temperature magnetic moments vary with the composition and are in the range of 3.4 to 5.5 μ_B. The Curie temperatures were found from measurements in induction fields of up to 1 T by applying molecular field fits respecting the applied field and are in the range of 400 to 620 K depending on the composition. Exchange of one Co in Co_2MnSn by Rh results in the stable, well-ordered compound CoRhMnSn. This exchange of one of the "*magnetic*" Co atoms by a "*non-magnetic*" Rh atom keeps the magnetic properties and half-metallicity intact. Those properties are completely determined by the Mn atoms together with valence electron count and do not depend much on the remaining type of atoms. This behavior allows to increase the spin-orbit interaction at one of the sites while keeping all other properties as a precondition for applications and physical effects relying on a large spin-orbit interaction. The ordered compound CoRhMnSn is a HMF with a saturation magnetization of 5 μ_B. It furthermore exhibits a high T_C of 620 K allowing utilization at room temperature and above.

In Section 6.1, the multifaceted Heusler alloys $Mn_{3-x}Co_xGa$ were investigated . Depending on the Co concentration x the compounds exhibit cubic or tetragonal Heusler structures. The tetragonal alloys are hard-magnetic, have low saturation magnetic moments, and high T_C. They are thus highly attractive for spin-transfer torque applications and represent new rare earth free permanent magnets. The cubic alloys are soft-magnetic and also exhibit high T_C. Besides the Co_2-based half-metallic ferromagnets, the cubic Mn_2-based compounds and alloys represent the second class of materials exhibiting the typical 100% spin polarized Heusler half-metallic electronic structure and obeying the Slater-Pauling rule. A continuous tunability of magnetic and structural properties simply depending on the Co concentration can easily be realized in these materials. With respect to spin-transfer torque it is expected that due to the strong relation to Mn_3Ga perpendicular magnetic anisotropy can be realized in thin films of tetragonal $Mn_{3-x}Co_xGa$ alloys. In that case, very similar compositions could be used as reference and as switching layers allowing for a strong increase of efficiency in the spin-transfer torque devices.

In Section 6.2, the detailed investigation of $Mn_{2-x}Rh_{1+x}Sn$ series was reproted.

Mn_2RhSn crystallize in the inverse tetragonal structure ($I\bar{4}m2$, space group no. 119) and shows hard magnetic hysteresis loop. As Mn_2RhSn has a tetragonal structure, it does not follow the Slater-Pauling rule and its low saturation magnetic moment of it beside its hard magnetic properties can make it suitable for spin-transfer torque applications. With substituting Mn by Rh, the inverse cubic structure for $Mn_{2-x}Rh_{1+x}Sn$ (x = 0.5, 0.6, 0.8) and regular cubic structure for Rh_2MnSn is observed. All cubic samples show perfect Slater-Pauling behavior and soft hysteresis loop and exhibit the typical 100% spin polarized Heusler half-metallic electronic structure. Both cubic and tetragonal phases exist for $Mn_{1.8}Rh_{1.2}Sn$ and it shows similar magnetic properties as observed for Mn_2RhSn.

Acknowledgement

List of Abbreviations

Å	Angstrom
A/Cm^2	Ampere per square centimeter
AMR	anisotropic magnetoresistance
bcc	body-centered cubic
CPP	current-perpendicular-to-plane
CIP	current-in-plane
CMR	colossal magnetoresistance
CPA	coherent potential approximation
DOS	density of states
eV	electron volt
EXAFS	extended x-ray absorption fine structure
fcc	face-centered cubic
FM	ferromagnetic metal
FLAPW	full potential linearized augmented plane wave
GMR	giant magnetoresistance
GGA	generalized gradient approximation
hcp	hexagonal close-packed
HMF	half-metallic ferromagnet
HAXPES	hard X-ray photoemission spectroscopy
K	Kelvin
m	magnetic moment
MTJs	magnetic tunnel junctions
MR	magnetoresistance
MRAM	magnetic random access memory
n_V	number of valence electrons per atom
N_V	valence electron number per formula unit
NM	nonmagnetic layer
PMA	perpendicular magnetic anisotropy
STT	spin-transfer torque
STT-MRAM	spin-transfer torque switched magnetic random access memory
SPRKKR	spin polarized Korringa - Kohn - Rostocker method
SQUID	super conducting quantum interference device

TMR	tunneling magnetoresistance
T_c	Curie temperature
XRD	X-ray powder diffraction
XAS	x-ray absorption spectroscopy
XMCD	x-ray magnetic circular dichroism
ϵ_F	Fermi energy
μ_B	Bohr magneton

List of Figures

List of Tables

Bibliography

[1] I. Zutic, J. Fabian, and S. Das Sarma. *Rev. Mod. Phys.*, 76:323, 2004.

[2] J. de Boeck, W. van Roy, J. Das, V. Motsnyi, Z. Liu, L. Lagae, H. Boeve, K. Dessein, and G. Borghs. *Semicond. Sci. Technol.*, 17:342, 2002.

[3] I. Galanakis. *Phys. Rev. B.*, 71:012413, 2005.

[4] I. Galanakis and P. H. Dederichs. *arXiv:cond-mat/0408068 v1*, 2004.

[5] I. Galanakis, N. Papanikolaou, and P. H. Dederichs. *Phys. Rev. B*, 66:134428, 2002.

[6] I. Galanakis, P. H. Dederichs, and N. Papanikolaou. *Phys. Rev. B*, 66:174429, 2002.

[7] I. Galanakis. *J. Phys.: Condens. Matter*, 16:3089, 2004.

[8] M. Zhang, X. Dai, H. Hu, G. Liu, Y. Cui, Z. Liu, J. Chen, J. Wang, and G. Wu. *J. Phys: Condens. Matter*, 15:7891, 2003.

[9] R. J. Soulen Jr., J. M. Byers, M. S. Osofsky, B. Nadgorny, T. Ambrose, S. F. Cheng, P. R. Broussard, C. T. Tanaka, J. Nowak, J. S. Moodera, A. Barry, and J. M. D. Coey. *Science*, 282:85, 1998.

[10] H. Kato, T. Okuda, Y. Okimoto, Y. Tomioka, K. Oikawa, T. Kamiyama, and Y. Tokura. *Phys. Rev. B.*, 69:184412, 2004.

[11] T. Shishidou, A.J. Freeman, and R. Asahi. *Phys. Rev. B.*, 64:180401, 2001.

[12] I. Galanakis. *Phys. Rev. B*, 66:012406, 2002.

[13] S. Sanvito and N.A. Hill. *Phys. Rev. B.*, 62:15553, 2000.

[14] H. Akinaga, T. Manago, and M. Shirai. *Jpn. J. Appl. Phys.*, 39:L1118, 2000.

[15] J.H. Zhao, F. Matsukura, K. Takamura, E. Abe, D. Chiba, and H. Ohno. *Appl. Phys. Lett.*, 79:2776, 2001.

[16] M. Horne, P. Strange, W.M. Temmerman, Z. Szotek, A. Svane, and H.Winter. *J. Phys.: Condens. Matter*, 16:5061, 2004.

[17] A. Stroppa, S. Picozzi, A. Continenza, and A. J. Freeman. *Phys. Rev. B.*, 68:155203, 2003.

[18] H. Akai. *Phys. Rev. Lett.*, 81:3002, 1998.

[19] J.-H. Park, E. Vescovo, H.-J. Kim, C. Kwon, R. Ramesh, and T. Venkatesan. *Nature*, 392:749, 1998.

[20] S. Datta and B. Das. *Appl. Phys. Lett.*, 56:665, 1990.

[21] K.A. Kilian and R.H. Victora. *J. Appl. Phys.*, 87:7064, 2000.

[22] C.T. Tanaka, J. Nowak, and J.S. Moodera. *J. Appl. Phys.*, 86:6239, 1999.

[23] J.A. Caballero, Y.D. Park, J.R. Childress, J. Bass, W.-C. Chiang, A.C. Reilly, W.P. Pratt Jr., and F. Petroff. *J. Vac. Sci. Technol. A*, 16:1801, 1998.

[24] C. Hordequin, J.P. Nozieres, and J. Pierre. *J. Magn. Magn. Mater.*, 183:225, 1998.

[25] P. J. Webster and K. R. A. Ziebeck. Springer, Berlin, 1988, pp. 75 184.

[26] F. Heusler, W. Starck, and E. Haupt. *Verh. der Deutsch. Phys. Ges.*, 5:220, 1903.

[27] F. Heusler. *Verh. der Deutsch. Phys. Ges.*, 5:219, 1903.

[28] R. A. de Groot, F. M. Mueller, P. G. van Engen, and K. H. J.Buschow. *Phys. Rev. Lett.*, 50:2024, 1983.

[29] J. Kübler, A. R. William, and C. B. Sommers. *Phys. Rev. B*, 28:1745, 1983.

[30] G. H. Fecher, H. C. Kandpal, S. Wurmehl, C. Felser, and G. Schönhense. *J. Appl. Phys*, 99:08J106, 2006.

[31] J. Kübler. *Theory of Itinerant Electron Magnetism.* Clarendon Press, Oxford, 2000.

[32] J. C. Slater. *Phys. Rev.*, 49:931, 1936.

[33] L. Pauling. *Phys. Rev.*, 54:899, 1938.

[34] A. P. Malozemoff, A. R. Williams, and V. L. Moruzzi. *Phys. Rev. B.*, 29:1620, 1984.

[35] H. C. Kandpal, G. H. Fecher, and C. Felser. *J. Phys. D: Appl. Phys.*, 40:1507, 2007.

[36] S. Wurmehl, H. C. Kandpal, G. H. Fecher, and C.Felser. *J. Phys.: Condens. Matter*, 18:6171, 2006.

[37] W. E. Pickett. *Phys. Rev. B*, 57:10619, 1998.

[38] O. Heusler. *Ann. Phys.*, 155:411, 1934.

[39] A. J. Bradley and J. W. Rodgers. *Proc. Royal Soc. A,*, 144:340, 1934.

[40] T. Graf, S. Parkin, and C. Felser. *IEEE Trans. Mag.*, 47:367, 2011.

[41] M. Puselj and Z. Ban. *Croat. Chem. Acta*, 41:79, 1969.

[42] H. Pauly, A. Weiss, and H. Witte. *Z. Metallk*, 59:47, 1968.

[43] X. Dai, G. Liu, L. Chen, J. Chen, and G. wu. *Solid State Commun.*, 140:533, 2006.

[44] V. V. Surikov, V. N. Zhordochkin, and T. Y. Astakhova. *Hyperfine Interact.*, 59:469, 1990.

[45] N. Lakshmi, A. Pandey, and K. Venugopalan. *Bull. Mater. Sci.*, 25:309, 2002.

[46] U. Eberz, W. Seelentag, and H. U. Schuster. *Z. Naturforsch. B*, 35:1341, 1980.

[47] J. Drews, U. Eberz, and H.-U. Schuster. *Journal of the Less Common Metals*, 116:271, 1986.

[48] G. E. Bacon and J. S. Plant. *J. Phys. F: Met. Phys.*, 1:524, 1971.

[49] J.C. Suits. *Solid State Commun.*, 18:423, 1976.

[50] Benjamin Balke, Gerhard H. Fecher, Jürgen Winterlik, and Claudia Felser. *Appl. Phys. Lett.*, 90:152504, 2007.

[51] J. Winterlik, B. Balke, G. H. Fecher, C. Felser, M. C. M. Alves, F. Bernardi, and J. Morais. *Phys. Rev. B*, 77:054406, 2008.

[52] J. B. Goodenough. Interscience, NY, 1963.

[53] J. Labbe and J. Friedel. *J. phys.*, 27:153, 1966.

[54] H. IHRIG, D. T. Vigren, J. Kübler, and S. Methfessel. *Phys. Rev. B*, 8:4525, 1973.

[55] F. Wu, S. Mizukami, D. Watanabe, H. Naganuma, M. Oogane, Y. Ando, and T. Miyazaki. *Phys. Rev. Lett.*, 94:122503, 2009.

[56] Y. Miura, K. Nagao, and M. Shirai. *Phys. Rev. B.*, 69:144413, 2004.

[57] H. C. Kandpal, V. Ksenofontov, M. Wojcik, R. Seshadri, and C. Felser. *J. Phys. D: Appl. Phys.*, 40:1587, 2007.

[58] S. Picozzi, A. Continenza, and A. J. Freeman. *Phys. Rev. B.*, 69:094423, 2004.

[59] J. Pierre, R. V. Skolozdra, J. Tobola, S. Kaprzyk, C. Hordequin, M. A. Kouacou, I. Karla, R. Currat, and E. Lelievre-Berna. *J. All. Comp.*, 101:262, 1997.

[60] P. J. Webster. *Contemp. Phys.*, 10:559, 1969.

[61] K. R. A. Ziebeck and K.-U. Neumann. Springer, Berlin, 2001, pp. 64 314.

[62] T. Graf, F. Casper, J. Winterlik, B. Balke, G. H. Fecher, and C. Felser. *Z. Anorg. Allg. Chem.*, 635:976, 2009.

[63] C. Felser, G. H. Fecher, and B. Balke. *Angew. Chem. Int. Ed.*, 46:668, 2007.

[64] M. Johnson and R. H. Silsbee. *Phys. Rev. Lett.*, 55:1790, 1985.

[65] M. N. Baibich, J. M. Brote, A. Fert, N. Nyugen Van Dau, F. Petroff, P. Eitenne, G. Creuzet, A. Friederich, and J. Chazelas. *Phys. Rev. Lett.*, 61:2472, 1988.

[66] P. Grünberg, R. Schreiber, Y. Pang, M. B. Brodsky, and H. Sowers. *Phys. Rev. Lett.*, 57:2442, 1986.

[67] W. Thomson. *Proc. R. Soc. London*, A8:546, 1857.

[68] I. Genish, Y. Kats, L. Klein, J. W. Reiner, and M. R. Beasley. *J. Appl. Phys*, 95:6681, 2004.

[69] R. von Helmolt, J. Wecker, B. Holzapfel, L. Schultz, and K. Samwer. *Phys. Rev. Lett.*, 71:2331, 1993.

[70] S. Jin, T. H. Tiefel, M. McCormack, R. A. Fastnacht, R. Ramesh, and L. H. Chen. *Science*, 264:413, 1994.

[71] J. S. Moodera, J. Nassar, and G. Mathon. *Annu. Rev. Mater. Sci.*, 29:381, 1999.

[72] M. Jullire. *Phys. Lett*, 54A:225, 1975.

[73] J. C. Slonczewski. *J. Magn. Magn. Mater.*, 159:L1, 1996.

[74] L. Berger. *Phys. Rev. B*, 54:9353, 1996.

[75] S. Krause, L. Berbil-Bautista, G. Herzog, and R. Wiesendanger. *Science*, 317:1537, 2007.

[76] P. Blaha, K. Schwarz, P. Sorantin, and S. B. Tricky. *Comput. Phys. Commun.*, 59:399, 1990.

[77] P. Blaha, K. Schwarz, G. K. H. Madsen, D. Kvasnicka, and J. Luitz. *WIEN2k, An Augmented Plane Wave + Local Orbitals Program for Calculating Crystal Properties*. Karlheinz Schwarz, Techn. Universitaet Wien, Wien, Austria, 2001.

[78] K. Schwarz, P. Blaha, and G. K. H. Madsen. *Comput. Phys. Commun.*, 147:71, 2002.

[79] J. P. Perdew, K. Burke, and M. Ernzerhof. *Phys. Rev. Lett.*, 77:3865, 1996.

[80] H. Ebert. Fully relativistic band structure calculations for magnetic solids for-malism and application. In H. Dreysee, editor, *Electronic Structure and Physical Properties of Solids. The Use of the LMTO Method*, volume 535 of *Lecture Notes in Physics*, page 191. Springer-Verlag, Berlin, Heidelberg, 1999.

[81] H. Ebert. *The Munich SPR-KKR package, Version 3.6*. http://olymp.cup.uni-muenchen.de/ak/ebert/SPRKKR. 2005.

[82] H. Ebert, J. Minar, and V. Popescu. Magnetic dichroism in electron spectroscopy. In K. Baberschke, M. Donath, and W. Nolting, editors, *Band-Ferromagnetism*, volume 580 of *Lecture Notes in Physics*, page 371. Springer-Verlag, Berlin, Hei-delberg, 2001.

[83] J. F. Nye. *Physical Properties of Crystals*. Clarendon Press, Oxford, 1957.

[84] S. Ueda, Y. Katsuya, M. Tanaka, H. Yoshikawa, Y. Yamashita, S. Ishimaru, Y. Matsushita, and K. Kobayashi. *AIP Conf. Proc.*, 1234:403, 2010.

[85] R. Hesse, T. Chasse, and R. Szargan. *Fresen J. Anal. Chem.*, 365:48, 1999.

[86] V. Y. Markiv, E. I. Hladyshevskii, and Y. B. Kuzma. *Dopovidi Akademii Nauk Ukrainskoi RSR*, page 1329, 1962.

[87] P. J. Webster. *J. Phys. Chem. Solids*, 32:1221, 1971.

[88] N. Shutoh and S. Sakurada. *J. Alloys Compd.*, 289:204, 2005.

[89] C. S. Lue and Y.-K. Kuo. *Phys. Rev. B*, 66:085121, 2002.

[90] J. Winterlik, G. H. Fecher, and C. Felser. *Solid State Commun.*, 145:475, 2008.

[91] A. Coelho. *TOPAS ACADEMIC, version 4.1*, 2007.

[92] A. Dannenberg, M. Siewert, M. E. Gruner, M. Wuttig, and P. Entel. *Phys. Rev. B.*, 82:214421, 2010.

[93] V. Alijani, J. Winterlik, G. H. Fecher, S. S. Naghavi, and C. Felser. *Phys. Rev. B*, 83:184428, 2011.

[94] H. C. Kandpal, G. H. Fecher, C. Felser, and G. Schönhense. *Phys. Rev. B*, 73:094422, 2006.

[95] X. Dai, G. Liu, G. H. Fecher, C. Felser, Y. Li, and H. Liu. *J. Appl. Phys.*, 105:07E901, 2009.

[96] B. Balke, G. H. Fecher, H. C. Kandpal, C. Felser, K. Kobayashi, E. Ikenaga, J.-J. Kim, and S. Ueda. *Phys. Rev. B*, 74:104405, 2006.

[97] J. Winterlik, S. Chadov, V. Alijani, T. Gasi, K. Filsinger, B. Balke, G. H. Fecher, C. A. Jenkins, J. Kübler, G. D. Liu, L. Gao, S. S. P. Parkin, and C. Felser. *arXiv:1105.0337v1 [cond-mat.mtrl-sci]*, 2011.

[98] B. Balke, S. Wurmehl, G. H. Fecher, C. Felser, and J. Kübler. *Sci. Technol. Adv. Mater.*, 9:014102, 2008.

[99] D. M. Teter, G. V. Gibbs, M. B. Boisen Jr., D. C. Allan, and M. P. Teter. *Phys. Rev. B*, 52:8064, 1995.

[100] G. E. Bacon and J. S. Plant. *J. Phys. F: Met. Phys.*, 1:524, 1971.

[101] S. Ouardi, G. H. Fecher, B. Balke, A. Beleanu, X. Kozina, G. Stryganyuk, C. Felser, W. Klö, H. Schrader, F. Bernardi, J. Morais, E. Ikenaga, Y. Yamashita, S. Ueda, and K. Kobayashi. *Phys. Rev. B*, in print:000000, 2011.

[102] P. Klaer, B. Balke, V. Alijani, J. Winterlik, G. H. Fecher, C. Felser, and H. J. Elmers. *Phys. Rev. B*, 84:144413, 2011.

[103] F. de Groot and A. Kotani. *Core Level Spectroscopy of Solids*. CRC, London, 2008.

[104] M. B. Trzhaskovskaya, V. I. Nefedov, and V. G. Yarzhemsky. *Atomic Data and Nuclear Data Tables*, page 97, 2001.

[105] M. Kallmayer, H. Schneider, G. Jakob, H. J. Elmers, B. Balke, and S. Cramm. *J. Phys. D: Appl. Phys.*, 40:1552, 2007.

[106] C. S. Fadley, D. A. Shirley, A. J. Freeman, P. S. Bagus, and J. V. Mallow. *Phys. Rev. Lett.*, 23:1397, 1969.

[107] S. Ouardi, B. Balke, A. Gloskovskii, G. H. Fecher, C. Felser, G. Schönhense, T. Ishikawa, T. Uemura, M. Yamamoto, H. Sukegawa, W. Wang, K. Inomata, Y. Yamashita, H. Yoshikawa, S. Ueda, and K. Kobayashi. *J. Phys. D: Appl. Phys.*, 42:084010, 2009.

[108] S. Wurmehl, G. H. Fecher, H. C. Kandpal, V. Ksenofontov, C. Felser, and H.-J. Lin. *Appl. Phys.Lett.*, 88:032503, 2006.

[109] K. Uchida, S. Takahashi, K. Harii, J. Ieda, W. Koshibae, K. Ando, S. Maekawa, and E. Saitoh. *Nature*, 455:778, 2008.

[110] S. Takahashi and S. Maekawa. *Phys. Rev. Lett.*, 88:116601, 2002.

[111] Y. K. Kato, R. C. Myers, A. C. Gossard, and D. D. Awschalom. *Science*, 306:1910, 2004.

[112] V. Alijani, S. Ouardi, G. H. Fecher, J. Winterlik, S. S. Naghavi, X. Kozina, G. Stryganyuk, C. Felser, E. Ikenaga, Y. Yamashita, S. Ueda, and K. Kobayashi. *Phys. Rev. B.*, in print:000000, 2011.

[113] S. Fuji, S. Sugimura, S. Idhida, and S. Asano. *J. Phys.: Condens. Matter*, 2:8583, 1990.

[114] Y. Sakuraba, M. Hattori, M. Oogane, Y. Ando, H. Kato, A. Sakuma, T. Miyazaki, and H. Kubota. *Appl. Phys. Lett.*, 88:192508, 2006.

[115] R. G. Pillay, A. K. Grover, P. N. Tandon, L. D. Khoi, and P. Veillet. *J. Magn. Magn. Mater.*, 647:15, 1980.

[116] J. Winterlik, G. H. Fecher, B. Balke, T. Graf, V. Alijani, V. Ksenofontov, C. Jenkins, O. Meshcheriakova, C. Felser, G. Liu, S. Ueda, K. Kobayashi, T. Nakamura, and M. Wojcik. *Phys. Rev. B.*, 83:174448, 2011.

[117] R. B. Helmholdt and K. H. J. Buschow. *J. Less-Common Metals*, 128:167, 1987.

[118] P. J. Brown, T. Kanomata, K. Neumann, K. U. Neumann, B. Ouladdiaf, A. Sheikh, and K. R. A. Ziebeck. *J. Phys.: Condens. Matter*, 22:506001, 2010.

[119] M. Meinert, J.-M. Schmalhorst, and G. Reiss. *J. Phys.: Condens. Matter*, 23:116005, 2010.

[120] S. K. Dhar, A. K. Grover, S. K. Malik, and R. Vijayaraghavan. *Solid State Commun.*, 33:545, 1980.

[121] K. H. J. Buschow, P. G. Van Engen, and R. Jongebreur. *J. Magn. Magn. Mater.*, 38:1, 1983.

[122] M. Gillessen and R. Dronskowski. *J. Comput. Chem.*, 30:1290, 2009.

[123] M. Gillessen and R. Dronskowski. *J. Comput. Chem.*, 31:612, 2010.

[124] F. Wu, S. Mizukami, D. Watanabe, E. P. Sajitha, H. Naganuma, M. Oogane, Y. Ando, and T. Miyazaki. *IEEE Trans Magn. 46, 1863 (2010).*, 46:1863, 2010.

[125] S. Ikeda, K. Miura, H. Yamamoto, K. Mizunuma, H. D. Gan, M. Endo, S. Kanai, J. Hayakawa, F. Matsukura, and H. Ohno. *Nature Mater*, 9:721, 2010.

[126] T. Kubota, Y. Miura, D. Watanabe, S. Mizukami, F. Wu, H. Naganuma, X. Zhang, M. Oogane, M. Shirai, Y. Ando, and T. Miyazaki. *Appl. Phys. Express*, 4:043002, 2011.

[127] S. Mizukami, F. Wu, A. Sakuma, J. Walowski, T. Kubota, X. Zhang, H. Naganuma, M. Oogane, Y. Ando, and T. Miyazaki. *Phys. Rev. Lett.*, 106:117201, 2011.

[128] H. Kurt, K. Rode, M. Venkatesan, P. Stamenov, and J. M. D. Coey. *Phys. Rev. B*, 83:020405, 2011.

[129] G. D. Liu, X. F. Dai, H. Y. Liu, J. l. Chen, Y. X. Li, G. Xiao, and G. H. Wu. *Phys. Rev. B*, 77:014424, 2008.

[130] N. Xing, H. Li, J. Dong, and C. Zhang. *Comput. Mater. Sci.*, 42:600, 2008.

[131] M. Meinert, J.-M. Schmalhorst, and G. Reiss. *J. Phys.: Condens. Matter*, 23:116005, 2011.

[132] M. Meinert, J.-M. Schmalhorst, C. Klewe, G. Reiss, E. Arenholz, T. Böhmert, and K. Nielsch. *Phys. Rev. B*, 84:132405, 2011.

[133] P. Klaer, C. A. Jenkins, V. Alijani, J. Winterlik, B. Balke, C. Felser, and H. J. Elmers. *Appl. Phys. Lett.*, 98:212510, 2011.

[134] K. J. Lee, O. Redon, and B. Dieny. *Appl. Phys. Lett.*, 86:022505, 2005.

[135] J. Itoh, K. Shimizu, H. Mizutani, A. K. Grover, L. C. Gupta, and R. Vijayaraghavan. *J. Phys. Soc. Jpn.*, 42:1777, 1977.

[136] R.G. Piliay and P.N. Tandon. *phys. stat. sol. (a)*, 45:K109, 1978.

[137] P.G. van Engen K.H.J. Buschow and R. Jongebreur. *J. Magn. Magn. Mater.*, 38:1, 1983.

[138] G. M. Julian R. A. Dunlap, S. Jha. *Can. J . Phys.*, 62:396, 1984.

[139] E. Uhl. *J. Magn. Magn. Mater.*, 49:101, 1985.